Chapter 1

Introduction

1.1. Objectives

The present work deals with the introduction and characterization of nanocomposites of poly(2-hydroxytheyl acrylate) and vitreous silica. Besides, it is described a process to produce a well-ordered 3D structure of cylindrical pores made by the reinforced composite previously presented in this study.

Poly(2-hydroxyethyl acrylate) swollen in water forms a hydrogel with good biological acceptance but poor mechanical properties, especially when the material may be somehow porous. Reinforcement by a nanometric silica phase obtained by acid catalyzed sol-gel reaction of tetraethoxysilane (also called tetraethyl orthosilicate) occurring simultaneously with the polymerization of the organic polymer leads to a hybrid material. Assuming that sol-gel reactions were completed, composites with different filler percentages were polymerized and their properties studied, inferring the inorganic phase threshold where silica percolation takes place. The prime aim at this first part of the study is thus to enhance the poly(2-hydroxyethyl acrylate) mechanical properties both in the rubbery and swollen state by the inclusion of small silica amounts, keeping the intrinsic hydrogel character of

polymer. Afterwards, the role of the hydrophilic/hydrophobic balance of the organic solution (precursor of the organic phase) on the silica topology is assessed. To do so, systematically controlled feeding ratios of hydroxyethyl acrylate and ethyl acrylate were used in order to synthesize hybrid materials with variable hydrophilicity of the organic phase. These materials were also characterized and compared with those properties previously introduced regarding poly(2-hydroxyethyl acrylate) sol-gel composites.

The second part of the work will focus on the description of a procedure to prepare scaffolds with a well-ordered array of cylindrical pores made by the hybrids introduced at the former part. The process include the use of a porogenic template made by stacked layers of commercial polyamide 6 fabrics, which in turn were compressed and sintered before use. After the polymerization of the monomers which filled the available spaces left inside the template, polyamide 6 was removed. The final porous structure is thus formed by the complementary part of the template fabric mesh, with new pores arising because of the sintering of the fabrics, which make this kind of scaffold tridimensionally interconnected.

1.2. Poly(2-hydroxyethyl acrylate)

Polymeric hydrogels are macromolecular networks able to absorb large water amounts without being dissolved. Their hydrophilicity is the consequence of the existence of polar chemical groups (–OH, -COOH, -$CONH_2$) included on its chemical skeleton which are able to establish hydrogen bonds with water molecules.

The success or rejection of a hydrogel as a biomaterial mainly relies on surface interactions between material and surrounding tissues, such as protein adsorption upon its surface. Hydrogels decrease their surface tension when swollen in aqueous or biological media, minimizing thus the surface tension differences between living tissue and material. Furthermore, it is reported that hydrophilic surfaces adsorb less protein quantities on their surfaces in comparison

with hydrophobic ones [1], making them suitable for medical purposes where cell adhesion must not be permitted (for instance, biomaterials in close contact with blood so as to avoid thrombus formations [2]). However, protein conformation as well as the strength of the protein mediated cell-material interactions will obviously rely on the nature of both protein and material. Besides, another key point concerning hydrogels as biomaterials also comes together with their high water uptake capability: it allows the supply of oxygen and nutrients and the removal of metabolic wastes due to high diffusion coefficients and permeability. However, high water absorption also brings poor mechanical properties when swollen, which is the most important handicap of polymeric hydrogels. There are several strategies to overcome that inconvenient and therefore to supply mechanical stability: copolymerization with a less hydrophilic monomer, increase the crosslinker density [3], formation of interpenetrated polymer networks [4], *etc*.

Crosslinked poly(2-hydroxyethyl acrylate) (henceforth PHEA) is a hydrogel with the intrinsic good biological properties characteristic of polyacrylates, making it potentially useful for medical applications. This polymer behaves as a rubber at room temperature, with a glass transition temperature (T_g) of 15.2 ºC [5,6]. As generally pointed above, its large capacity of water uptake leads to decreased mechanical resistance [3]. The need to find ways so as to reinforce hydrogels on its swollen state arises, especially when beside they must be porous. Several trials were made to obtain PHEA scaffolds with few micrometers of average pore diameter following a procedure which involves polymerization in the presence of a solvent (water or methanol) [7,8,9]. Another strategy only tries to cover the surface of a hydrophobic poly(methyl methacrylate) macroporous scaffold with a thin layer of PHEA obtained by plasma polymerization [10]. Regardless the method used to manufacture porous PHEA samples, there is still the need to improve its mechanical properties. The procedure chosen in this work to reinforce PHEA is the inclusion of inorganic filler (silica) throughout the polymer matrix.

Let's examine first the dissipation phenomena that pure PHEA undergoes. Completely dried PHEA exhibits three mechanical

relaxations which were shown by dynamic-mechanical spectroscopy [11]: the highest energetic α-transition is related with the cooperative relaxation of the macromolecular backbone and takes place at 9ºC; the others two take place at lower temperatures and are ascribed to local relaxations of different parts of the acrylic side chain: β-dispersion is connected with the onset of mobility of the side chain ester groups (COO) and takes place around -90ºC; besides, γ-dispersion is assigned to the hindered rotation of the hydroxyethyl groups (CH_2CH_2OH) and takes place at lower temperatures. Everything said until now in this paragraph refers pure PHEA behaviour as a rubber at the temperature of a human body (~37ºC). Furthermore, water molecules act as plasticizers lowering the α-transition [12].

Water is a good solvent of hydrogels and therefore if constituent macromolecules are not physical and/or chemically crosslinked they will be dissolved when immersed in water. For the homopolymer PHEA there is no need to add small molecules acting as crosslinkers, like ethyleneglycol dimethacrylate, because it spontaneously establishes covalent bonds between chains due to etherification and transesterification reactions involving hydroxyls and oxo-hydroxyethyls of the pending acrylic groups [13].

1.3. Introduction to the sol-gel process

Silica is one of the most common mineral in the world. Silicon dioxide presents several polymorphs, either crystalline (for instance quartz, cristobalite and tridymite) or amorphous. The reason why these broad types of structures exist lies on the flexibility of the Si-O-Si siloxane bond, whose bond angle can rotate from 120º to almost 180º (completely aligned silicons). On the contrary, the distribution of O-Si-O angles is narrower and approaches to that of a tetrahedron [14]. Indeed, the intuitive idea of silica structures one can image is an arrangement of rigid tetrahedra connected by Si-O-Si hinges which give enough flexibility so as to build the different silica polymorphs.

Silica hydrophilicity depends on the existence of structural defects able to react with water (mostly on its surface) yielding hydroxyls joint to silicon atoms (these bonds are named silanols and they will be along this work). In fact, a completely perfect silica surface will yield a hydrophobous material. Acidity of silanols (and therefore silica reactivity) depends on the substitution degree of the silicon where silanols are bound: if only one Si-O-Si siloxane bond is changed by Si-OH, this silanol is named terminal; besides, two hydroxyls bonded to the same silicon atom are called geminal. Lately *ab initio* studies carried out by Tielens et al regarding amorphous silica point out that geminal silanols are slightly more acidic than terminal ones [14], result which was previously reported by Zerda et al [15].

At the end of the previous century a process called sol-gel was exhaustively studied and developed in order to obtain ceramics almost at room temperature [16-20], avoiding conventional methods which imply heating up to hundreds of degrees. Based on those studies, a new path for obtaining polymer-ceramic composites was proposed, taking advantage of the simultaneous polymerization of both materials. The sol-gel reaction is a polymerization process in which a precursor hydrolyzes and condenses to form a network. The characteristics of the resulting network depend on some critical parameters of the reaction such as the relative rate of the hydrolysis and the condensation reactions [15,16], the molar ratio between water and alkoxide [19], the acidic or basic character of the environment [16], the nature [21] and quantity [20] of the solvent in which the sol-gel reaction takes place, and also on whether the hydrolysis takes place in a single or in multiple steps [22]. All these parameters will be explained below.

1.3.1. Sol-gel reactions

The sol-gel process involves two chemical reactions by which alkoxides undergo hydrolysis and condensation. These two reactions can be summarized by Eq. 1.1, Eq. 1.2 and Eq. 1.3 for tetravalent alkoxides.

$$M(OR)_4 + yH_2O \rightarrow M(OR)_x(OH)_y + yROH \quad \text{(Eq. 1.1)}$$

$$M(OR')_x(OH)_y + M(OR'')_{x'}(OH)_{y'} \rightarrow (OH)_{y-1}(OR')_x M - O - M(OR'')_{x'}(OH)_{y'-1} + H_2O \quad \text{(Eq. 1.2)}$$

$$M(OR')_x(OH)_y + M(OR'')_{x'}(OH)_{y'} \rightarrow (OH)_{y-1}(OR')_x M - O - M(OR'')_{x'-1}(OH)_{y'} + R''OH \quad \text{(Eq. 1.3)}$$

in which *M* can be Si, Ti, Zr, Al, Sn, Ce, Mo, W, *etc*, and *R* the alkyl group of the alkoxide (R=C_nH_{2n+1}). Focused on tetraethoxysilane (henceforth TEOS), the silicon alkoxide used in this work (M=Si and R=CH_2CH_3), it is first hydrolyzed (Eq. 1.1) in the presence of water to produce silanols (a reactive hydroxyl group) and ethanol (the corresponding alcohol of the alkyl group of the alkoxide). Afterwards, these silanols react in two different ways to produce the final siloxane groups (Si-O-Si): two silanols can react and condense themselves (Eq. 1.2), or a silanol can react with a not hydrolyzed *OR* group to produce ethanol (Eq. 1.3). Thus, based on Eq. 1.1, it is necessary 4 molecules of water to stoichiometrically hydrolyze a molecule of TEOS. This value will be used later on to define the conditions where sol-gel reactions are carried out.

It is obvious that these three equations do not describe the underlying intermediate products created during the process as hydrolysis and condensation advance (mainly oxooligomers, inorganic polymers or more branched polymeric molecules) [22]. In fact the final inorganic polymeric structure will be dependent on how these intermediate species grow (either linear or branched, with a high or low condensation degree) [19], which indeed depend on the initial polymerizing conditions.

1.3.2. Factors affecting the hydrolysis rate of tetraethoxysilane

The polymerization conditions in which silica is obtained determine the wide spectrum of polymeric structures available with the sol-gel process: from full condensed colloidal silica to linear chain or weakly branched polymeric species.

A key factor to success synthesizing sol-gel nanocomposites is the choice of the metal alkoxide. The nature of the metal alkoxide which undergoes the sol-gel process is crucial because of its intrinsic sensitivity to hydrolysis. A high chemical reactivity is due to a low electronegativity of the central atom of the alkoxide precursor as well as to the ability of this central atom to exhibit several coordination states, which change spontaneously during the hydrolysis and condensation reactions [23]. In fact, there are situations where it is not possible to use certain alkoxides to produce nanocomposites without chemical modifications due to its large hydrolysis sensitivity [24,25]. Generally, the higher the ionic radii of the central atom (the ability to increase its coordination number and degree of unsaturation) the higher the reactivity [24,26]. Turning to TEOS, silicon has a low electrophilicity and its coordination number remains the same in both alkoxide and silica. As a consequence, silicon alkoxides are thus not too much reactive [25].

Hydrolysis of alkoxides takes place by a nucleophilic attack of the water oxygen to the silicon atom (Eq. 1.1). This attack is generally delayed by the length of the alkyl group of the alkoxide which is being hydrolyzed and by its branching degree. Besides, the inmiscibility gap which exists between TEOS and water at room temperature make the hydrolysis rate decrease [27,28]. There are different ways to surpass that inmiscibility and promote the dissolution of water and TEOS (and therefore the hydrolysis rate): the addition of solvents [28-31] or mechanical stimulation [27,32,33].

Donatti et al studied the hydrolysis rate of a solventless solution of TEOS and water by calorimetry [32]. In order to homogenize the solution without loosing the exothermic peaks of hydrolysis taking place at low exposure times, the solution was stimulated by ultrasounds

while measuring. They concluded that the overall hydrolysis process is thermally activated, following the Arrhenius equation

$$t_p \sim \exp\left(\frac{\Delta h}{\Re}\frac{1}{T}\right) \qquad \text{(Eq.1.4)}$$

where t_p is the time required for the maximum of the exothermic hydrolysis peak to arise, Δh the activation energy of the hydrolysis and T the temperature at which the assay takes place. Moreover, they also studied the hydrolysis peak evolution with systematic small additions of ethanol [32,33]: the time needed for hydrolysis diminishes when increasing the solvent amount as a consequence of the homogenizing effect of ethanol.

In latter works, Donatti et al also studied the influence of the initial water quantity [27] and the pH effect (the nature of the catalyst) [34] on the TEOS hydrolysis rate. For higher water amounts than the stoichiometric (>4), t_p increases and thus the hydrolysis rate falls. They also ascertained that the final quantity of hydrolyzed species did not depend on the initial water amount of the dissolution; however, what they do not establish is a relationship between the relative rates of hydrolysis and condensation reactions. Nonetheless, whether the final hydrolyzed species are the same regardless the initial water amount, it is only possible if the condensation reaction is enhanced for low water initial amounts so as to produce water molecules (Eq. 1.2) which continue the hydrolysis [27]. On the other hand, Donatti et al also found a logarithm relationship between the hydrolysis rate and the hydrogen ion concentration $[H^+]$: the lower the pH the faster the hydrolysis [34]. Anyway, to conclude it must be highlighted that above all these parameters affecting hydrolysis, it is claimed that the most important one is the initial water amount [24].

Considering these factors altogether, it can be inferred that hydrolysis of TEOS during the sol-gel process is autocatalytic [35]: the ethanol generated during hydrolysis and condensation reactions (Eq. 1.1 and Eq. 1.3) helps to the homogenization of water and TEOS and

therefore enhances latter hydrolysis; furthermore, the released latent water (Eq. 1.2) further hydrolyzes TEOS molecules, especially in low water conditions.

1.3.3. pH influence on the condensation mechanism

Aside the above commented influences on the hydrolysis rate, the condensation mechanism undergone by silica during its gelification through the sol-gel process is strongly dependent on the pH conditions. Zerda et al, based on previous works by Okkerse [36], established the chemical condensation reactions which lead to a silica structure analyzing by ^{29}Si NMR the evolution of the early species generated during gelification of tetramethoxysilane (TMOS) with stoichometric excess of water (ratio between TMOS and water equal to 10) at room temperature [15]. They claimed there are mainly two situations regarding the influence of pH on the condensation mechanism of TMOS to consider: pH below and above that corresponding to the isoelectric point (pH~2.2) [15].

$$\equiv Si - O^{-} + HO - Si \equiv \leftrightarrow \equiv Si - O - Si \equiv + OH^{-} \qquad \text{(Eq.1.5)}$$

When the pH surpasses the isoelectric point, the polymerization reaction is catalyzed by OH^{-} anions following Eq.1.5. Depending on pH, ionization equilibrium is established so as to produce deprotonated silicon anions, which in turn by a nucleophilic attack react with silanols to yield siloxane bonds. The ionization silanol degree depends on pH, and the condensation rate is thus proportional to the OH^{-} concentration (the higher the pH the lower the gelification time [15]). The deprotonated silicon species ($\equiv Si - O^{-}$) tend to react with those silanols with higher acidic character (i.e. silanols of intermediate species with larger condensation degrees), which finally promotes the formation of isolated highly condensed clusters.

On the other hand, at pH values below the isoelectric point, the condensation mechanism is completely different. This time the condensation reaction is acid catalyzed by H^+ protons following Eq.1.6. The equilibrium reached by H^+ and silanols to form temporally positive charged species yields to an electrostatic attraction between those charged molecules and silanols (electrophilic attack). The proton excess is eventually erased by either a water molecule or another silanol.

$$\equiv Si - OH_2^+ + Si(OH)_4 \leftrightarrow \equiv Si - OH^+ - Si(OH)_3 + H_2O \qquad \text{(Eq.1.6)}$$

As pointed out when introducing the condensation mechanism for pH larger than 2.2, the silanol acidity varies with the degree of substitution of the silicon where it is bound (geminal *versus* terminal Si-OH), as well as its position within the premature silica network: the lower the silicon substitution and the more peripheral the silicon is the lower its acid character [14,15]. Therefore, it is more likely that $\equiv Si - OH_2^+$ species react with end group silanols in species which low condensation degrees. Thereby this polymerization mechanism promotes the formation of linear or weakly crosslinked branched inorganic polymers with low condensation degrees.

1.3.4. Silica growth: linear versus branched species

The silica network topology relies on the initial sol-gel conditions, mainly pH (acid or basic conditions) [15] and water [18,20]. Taking into account these two parameters, there are thus four basic combinations between the initial sol-gel conditions which may lead to different silica topologies. In fact, there are three basic different structures: linear or weakly branched inorganic polymers, colloidal silica and an intermediate between them. All of them will be explained below.

At the initial stages of the silica polymerization, isolated species are hydrolyzed and form dimers, trimers and so on, with a condensation degree which relies on the sol-gel process conditions. Through gelation, initially isolated growing species contact themselves and react, forming the main silica skeleton of a gel. The main properties of that gel (density, free volume, free energy and condensation degree) are the outcome of those initial species and following steps (mainly desiccation). The final different properties (for instance porosity, surface tension,…etc) of silica gels synthesized at different conditions are thus dependent of their condensation degree (i.e. how they grew: either linearly or in a more branched fashion). A sketch of the silica gelation process under different polymerizing conditions is presented in Figure 1.1.

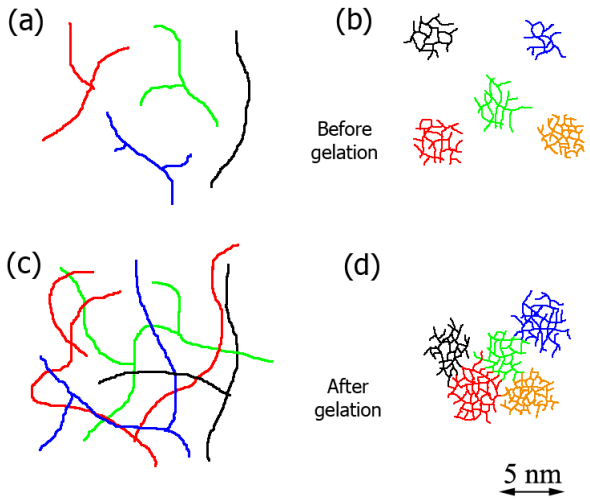

Figure 1.1. Polymer growth ((a) and (b)) and gel formation ((c) and (d)): (a), (c) acid catalyzed conditions with water amounts lower than stoichiometry (<4); (b), (d) basic conditions

The underlying reason of different intermediate species is dependent on the relative rates of hydrolysis and condensation which take place at the initial conditions: if the condensation reaction is not favored, the generated intermediate molecules show higher

condensation degrees. Precisely due to that dense network, they could not entangle through gelation and the silica gel generated behaves as a cluster aggregation ((d) in Figure 1.1). On the contrary, when condensation rate is similar to that of hydrolysis, linear and/or weakly branched oligomers (fuzzy networks) are formed, diffusing their low crosslinked networks along other similar species when gelifying ((c) in Figure 1.1) [18,25].

Through silica gel desiccation (if necessary), the volatile components are removed and the sol-gel products' structure is modified: the silica skeleton is shrunk. Remaining groups which did not react previously due to steric hindrances and lower reactivities now polymerize to achieve a higher degree of condensation and thus silica structure parameters (specific surface area, pore diameter, porosity) change. Nevertheless, the number of non-bridging oxygens (not Si-O-Si oxygens) is larger in sol-gel products than in the corresponding glass obtained from melt (i.e. lower condensation degrees) [18].

It may be concluded that not always is possible to achieve full condensed silica by a sol-gel process. Indeed, very special and restrictive conditions are required to obtain colloidal SiO_2: the reaction must be basic catalyzed, with water amounts much higher than stoichiometry (»4) and low silica precursor concentrations [37]. The underlying reasons for these conditions are that all silica precursor must be hydrolyzed before the onset of condensation (it means a hydrolysis rate really higher than condensation), forming a solution of monosilicic acid ($Si(OH)_4$) which undergoes condensation to form full condensed silica. If condensation starts before hydrolysis finishes, intermediate species are form with different degrees of condensation. Under acid catalyzed conditions and stoichiometrically lower water amounts (<4), the growth of the silica is mainly linear or branched polymers (species with lower condensation degrees) [18,19]. The other conditions lead to isolated species with higher condensation degrees (but not fully condensed) which form dispersed clusters [16].

1.4. Introduction to composites

Composites are systems formed by two or more different phases, whose combination produces unique properties which are different to those exhibited by the components alone. Composites are thus technologically interesting because of those exclusive properties which can not be afforded by a simple materials family (neither metals, nor ceramics, nor polymers). Generally, the phases (materials) that composites are made of are usually identified as matrices and fillers (or reinforcers). The matrix is the phase which adheres to fillers and it is responsible for the general composite shape; furthermore, matrices protect filler surfaces from damage and keep them separated so as to avoid crack propagation. On the contrary, fillers give mechanical strength thanks to the tension transmission from the matrix.

Organic-inorganic composites unite some of the best properties of both phases and improve some of the worst. However, final properties of composites are generally more complex than a simple sum of their single component properties because of synergistic effects, especially when heterogeneity only takes place at a nano-scale levels (the so-called nanocomposites), where the interactions between phases are maximized due to a large specific surface area. Due to the intrinsic thermodynamic incompatibility of the organic-inorganic composites' phases, there could appear voids (potential cracks' nuclei) at the interfaces because of the interfacial energy (wettability between phases), which finally yields undesirable poor properties.

Focusing on ceramic-polymer hybrids, there are several strategies to synthesize composites depending on the initial states of the raw materials: the organic phase can be introduced as a monomer, oligomer, polymer precursor or a lineal polymer from a solution, emulsion or melt [38]; on the other hand, the inorganic phase may be inserted as a metal alkoxide, a porous structure, or layered silicate hosts where molecules of polymer guests are intercalated [39].

The heterogeneous properties of materials are determined by several common factors: the components' characteristics, composition, structure and interfacial interactions, which are described as follows.

1.4.1. Composite composition

The choice of composite's composition relies on the purpose for which the material is designed. This work is focused on biphasic materials made by a polymer matrix (PHEA) reinforced by an amorphous silica phase. The elastic properties of the hybrid composite will be dependent on the filler percentages: for low silica contents, it is expected that the behavior of the hybrid material is governed by the properties of the polymer; on the contrary, for high silica percentages, when both phases are co-continuous, the nanocomposite performance will approach that of a ceramic, increasing its brittleness. Thus silica was systematically varied from low (5 and 10 wt%) to high contents (30wt%) to explore the challenges this hybrid system can face (generally between those of glasses and those of polymers). In order to compute TEOS amounts to produce composites with well defined inorganic contents, it was assumed that sol-gel reactions were completed and full condensed silica is obtained through a chemical reaction that can be summarized by Eq.1.5 [29].

$$Si(O-C_2H_5)_4 + 2H_2O \rightarrow \equiv Si-O-Si \equiv + C_2H_5OH \qquad \text{(Eq. 1.7)}$$

Eq. 1.8 is the outcome of a mass balance on the nanocomposite. Assuming 100% efficiency for the PHEA polymerization, the mass of 2-hydroxyethyl acrylate (hereinafter HEA, m_2) equals that of PHEA. Besides, the silica mass (m_{SiO2}) is related with TEOS mass (m_1) by the molar relationship shown by Eq. 1.7; M_{SiO2} and M_{TEOS} are the molar weights of silica and TEOS, (~60 and ~208 g/mol, respectively).

$$m_t = m_2 + m_{SiO2} = m_2 + \frac{M_{SiO2}}{M_{TEOS}} m_1 \qquad \text{(Eq. 1.8)}$$

Just defining the silica percentage (σ) of the hybrid material as the ratio between silica and total masses, it can be established a relationship between the monomer initial masses which will be used to estimate the feeding amounts of HEA and TEOS (Eq. 1.9) [29].

$$\sigma = \frac{m_{SiO2}}{m_t} = \frac{\frac{M_{SiO2}}{M_{TEOS}} m_1}{m_2 + \frac{M_{SiO2}}{M_{TEOS}} m_1} \Rightarrow \frac{m_2}{m_1} = \left(\frac{1}{\sigma} - 1\right) \times \frac{M_{SiO2}}{M_{TEOS}} \qquad \text{(Eq. 1.9)}$$

1.4.2. Filler structure

There are several geometric issues regarding fillers which modify the final performance of composites. In fact, the expected mechanical properties can be tuned by changing the components' structures [25]. Some of them involved the aspect ratio of fillers, size, their orientation and dispersion (clustering) throughout the matrix.

Termonia modeled the influence of the filler shape on the mechanical tensile modulus of nanocomposites [40]. The aspect ratio (*l/d*) of fillers is defined by the relationship between geometric values which define their shape (mainly length or thickness and diameter). The critical aspect ratio (l/d_{cr}) equals the one needed to reach those properties given by infinite large fillers. He found when comparing two different shapes that platelets-like fillers ("disks") have l/d_{cr} higher than fibers-like fillers ("rods") because of the intrinsic higher platelet inertia [40].

Besides, the filler orientation degree determines the isotropic (or anisotropic) properties of the composite regardless the shape of the reinforcement. The general behavior of composites with the filler orientation is similar to that shown with crystalline fibers [41]: the higher the orientation the larger the mechanical tensile modulus along the orientation direction [40,42].

Another parameter which affects the composite properties is the filler dispersion throughout the matrix. The trend to cluster of nanofillers is a well-known problem [25,43-45]. The exceptional properties of nanocomposites are based on the high contact area between matrix and filler. Through clustering, both the aspect ratio and the specific surface area decrease with the obvious abatement of the mechanical properties at fixed filler percentages [29,40]. To reduce the trend of phase segregation often caused by the thermodynamic incompatibility of the components, it is essential either to enhance the intermolecular interactions between phases or promote the existence of strong chemical bonds [25].

Related to the aforementioned aggregation trend in particle-filled nanocomposites, it is obvious that the filler size influences the composite properties as well. For instance, optical applications are generally out of the scope of classic micro-composites owing to their lack of transparency; however, nanocomposites may be transparent as long as their materials are also transparent and the filler average size does not surpass few hundreds of nanometres (<400 nm) [29,46].

1.4.3. Interfaces and interphases

Generally, an interphase with different properties than the original materials constituting the composite is formed when composites are. There are different origins for interphases: the adsorption of one material onto a surface (e.g. monomers upon a filler surface to form polymer composites); network interpenetration (e.g. the interdiffusion in polymer blends); and chemical reactions between materials (e.g. fiberglass). The quantity and characteristics of the

generated interphases depend on their origin and component properties, which in turn are able to influence on some properties of the composite [40,47,48]. On the contrary, there are other macroscopic properties which are not significantly affected by the interphase characteristics [49].

Nanocomposites, in comparison with traditional composites, increase the contact area between their phases (the so-called interface). Additionally to that huge contact area, an intermediate genuine phase may be formed there, the interphase. Its properties differ from those of the pure components, normally due to interactions (either physical or chemical) between them. Sometimes, there is a gradient of properties from the interface to the unperturbed phase [50]; there are others where the interphase has its own properties different from those of neat counterparts (like fiberglass). Nanocomposite properties do not only depend on the interface size, but also on their interactions. For instance the change in the glass transition temperature of polymer filled nanocomposites (referred to the pure polymer) relies on the interfacial energy of the involved materials [48,51,52]: if the polymer matrix wets the filler then its glass transition temperature increases and *vice versa*.

Termonia also evaluated the effect of the interphase properties on the mechanical modulus [40]. His works pointed out that the enhancement of the properties at interfaces and the increase of their average thickness improve the composite modulus, in agreement with other studies [43,53-55]. However, the improvement of mechanical properties at interphases is somehow limited (physical *versus* chemical bonds between filler and matrix, wettability of fillers by the matrix material); on the other hand, it is easier to tailor the thickness of interphases mainly by surface treatments or modifications.

1.5. Sol-gel derived nanocomposites

A classification of materials product of the synthesis of nanocomposites by the sol-gel process must take into account the

nature of the inorganic precursor, the real network structures which are formed during the process because of the initial polymerizing conditions, and the interactions between organic and inorganic composite components [24].

The existence of (reactive or not) organic groups in alkoxides either modifies the final inorganic structure which is able to form, or they react and join the organic polymer network [24]. In this latter situation, the inorganic phase would act as an *n*-functionality crosslinker [29]. The occurrence of either strong (mainly covalent bonds) or weak interactions (van der Waals forces, hydrogen bonds and/or electrostatic forces) between phases depends on the stability of those hybrid bonds and the chance to functionalize either alkoxides (previous to the inorganic phase formation) or previously synthesized filler surfaces.

1.5.1. Silica reinforced poly(2-hydroxyethyl acrylate)

The procedure used in this work to enhance the PHEA mechanical properties is to produce hybrid organic-inorganic nanocomposites with an included silica phase obtained simultaneously with the polymer by a sol-gel process. The simultaneous polymerization of both organic and inorganic phases generally yields to either well distributed filler dispersion throughout the matrix or, on the contrary, high interpenetrated networks. Polymer-silica nanocomposites have received much attention in recent years both from a fundamental and an applied perspective [56]. The preparation and characterization of hybrid materials by means of inorganic precursors, such as tetramethyloxysilane (TMOS) or TEOS, have been carried out with several organic polymers: in [46] a poly(methyl methacrylate)-silica composite was prepared and its structure investigated by Nuclear Magnetic Resonance; the surface of acrylic-silica hybrids was studied by scanning force microscopy in [57] and several nanodomains were identified. X-ray analysis was extensively used with poly(dimethyl sulfone) using TEOS as a precursor [57,58]. Closer to the system studied in this work, the structure and morphology of

poly(hydroxymethyl methacrylate)-silica hybrids using TEOS as a precursor were investigated [29,44] by different techniques including Atomic Force Microscopy in the contact mode for characterizing the surface morphology of the samples. PHEA-silica hybrids using TEOS as a precursor were investigated by Small Angle X-ray Scattering and Transmission Electron Microscopy [59] and the uniform dispersion of the inorganic phase throughout the sample was seen to be dependent on the synthesis conditions.

By the simultaneous polymerization of the polymeric matrix and the silica phase a new kind of hybrid material was obtained, in which the silica phase is dispersed in the form of domains with typical sizes of tens of nanometers [59]. The complete process by which the final silica phase develops takes place in three steps: the hydrolysis of the alkoxide groups of TEOS to form silanols, the condensation of the previously formed silanols to polymerize into silica polymers, and the aggregation of partially condensed silica macromolecules to build up the network [16]. Under acid catalyzed reaction conditions and with a stoichiometrically deficient amount of water (>4) it is known that the condensation rate is much greater than the production of silanols by the hydrolysis reaction, and the silica forms as an extremely fine (nanometer sized) network [16]. It has been reported that the addition of a co-solvent like ethanol makes the hydrolysis reaction faster for TEOS [32]. Despite of the immiscibility gap which exists between TEOS and HEA at room temperature, no additional solvent was added in this work since silanols are rapidly formed in the presence of water after a short induction time, making the solution of TEOS miscible with the solution of HEA and initiator [32].

The different relative rates of polymerization of the organic and inorganic phases may induce a macro-phase separation, but when the silica network forms faster than PHEA, the size of the typical phase aggregate is so small that transparent hybrid materials are obtained and phase separation only takes place at a nanoscale level [59]. This applies to the present work, where the polymerizing conditions were chosen so that the obtained PHEA-based sol-gel nanocomposites retain the transparency characteristic of neat PHEA.

1.6. Scaffolds made by hybrid materials

The applications of porous materials are nowadays widespread. As biomaterials, there are uses which require those porous structures to act as cellular scaffolds. Interconnection and geometry of pores, physicochemical properties and mechanical resistance of the material play in these applications a major role. The layout of the pore geometry of the scaffold should try to mimic the arrangement of key components and structures in the tissue whose regeneration is to be assisted, an arrangement which is often very special. Thus, it is well known that the arch-wise disposition of the collagen fibers near the articular surface of hyaline cartilage is critical for the functional performance of this tissue. Trabecular bone is another example of a tissue possessing a distinct geometrical arrangement of its component structures. In general these layouts are dictated by the mechanical and functional requirements of the different specialised tissues.

There are several methods to produce scaffolds, which include gas foaming [60], sintering fiber meshes [61] solvent casting [62], and others [63,64]. Different kinds of porogenic agents and ways to induce porous architectures have been reported [61,65,66]; each has some advantages and some disadvantages with respect to matters such as the control of the pore size, pore distribution, interconnectivity and construction of channels within the scaffold to guide cell growth. Some scaffolds are intended to degrade in their biological environment [67,68], while others must be designed to keep their properties and integrity for a long lifetime [69,70]. Mechanical resistance depends both on the material properties and on the pore structure of the scaffold, and the high porosity requirements of scaffold structures invariably run counter the mechanical and creep requirements on them. This problem is more serious in the case of hydrogels which exhibit very poor mechanical properties in their swollen state, the more so if they are porous.

PHEA porous structures have been successfully obtained mainly by polymerization in the presence of solvents (water, ethanol or methanol) [7-9], taking advantage of a phase segregation process called microsyneresis [71]. However, sometimes either their pore size or porosity may not be suitable for particular biomedical applications, where higher average pore sizes are requested.

Concerning the potential biological response of the inorganic phase of the nanocomposite, silica is a biocompatible material and has been reported to possess bioactive properties [72]. In this second part of the thesis, the simultaneous polymerization of the organic and inorganic phases was carried inside a specially tailored porogenic template. The ensuing scaffolds thus resulted in organic-inorganic hybrid nanocomposite materials [29,59,73] with a well-ordered array of large interconnected orthogonal cylindrical pores.

As an example of a possible application, this material may be of use in the design of non-biodegradable scaffolds to replace partially the fibrous ring of human intervertebral discs, an application in which a high degree of guidance of ingrowing tissue is needed, as well as a high water uptake and improved mechanical properties of the material. Intervertebral disks are constituted by the inner pulpous nucleus (composed mainly by chondrocytes and water) and a surrounding fibrous ring (collagen and proteoglycans) [74]. Their degeneration is a common disease basically due to aging which is manifested by increased stiffness, mechanical overstress and/or dehydratation of nucleus [74]. Polymer hydrogels are materials with good biocompatibility which are able to absorb large quantities of water, and thus seem candidates for replacement materials [75].

1.7. Nanoindentation assays by Atomic Force Microscopy

Nanoindentation is a technique that will be used to assess the mechanical properties of the hybrids at a nanoscale level. Despite of several works which deal with the AFM use as an indenter [76-79], it is worth mentioning the fundamentals of this useful method.

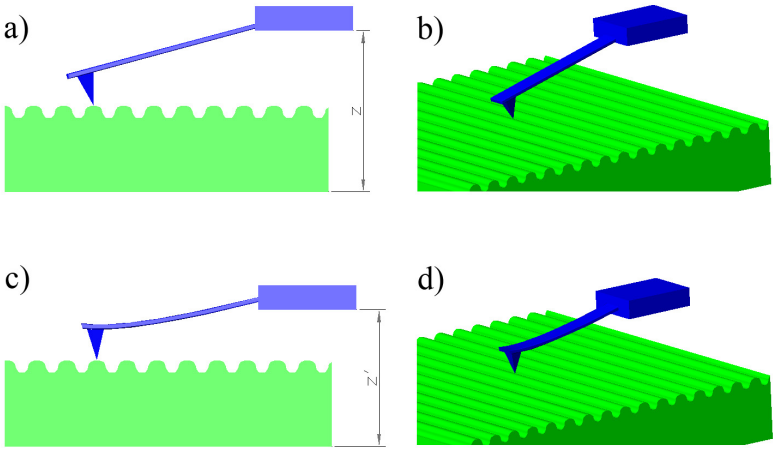

Figure 1.2. Sketch for the deflexion calibration on a surface with no deformation due to the tip indentation: a) tip approach to the surface; c) deflexion of the tip. b) and d) show the corresponding tridimensional images.

Indentation is a common way to evaluate local properties of materials which are finally extrapolated to bulk. Atomic Force Microscope (AFM) can be used as a nanoindenter to perform force-volume probes (also called nanoindentation) without further specialized depth-sensing instruments [76]. In force-volume assessments, a rigid sharp tip interacts with a surface while applied force and penetration depth are recorded (Figure 1.2). An array of indentations is normally done along the target surface, and for each indentation measurement a force-displacement curve is obtained (Figure 1.3). Those plots normally collect the loading and unloading cycles, which must coincide if material's behavior is purely elastic. On the contrary, hysteresis loop appears when viscoelastic materials are studied [76].

Figure 1.2 shows how the cantilever deflexion is calculated: several indentation assays are performed over a surface which is practically not deformed by the AFM tip. The difference between height distance immediately before (z on Figure 1.2a) and after (z' on Figure

1.2c) tip deflexion ($d = z - z'|_{F\max}$) yields an average tip deformation per force unit.

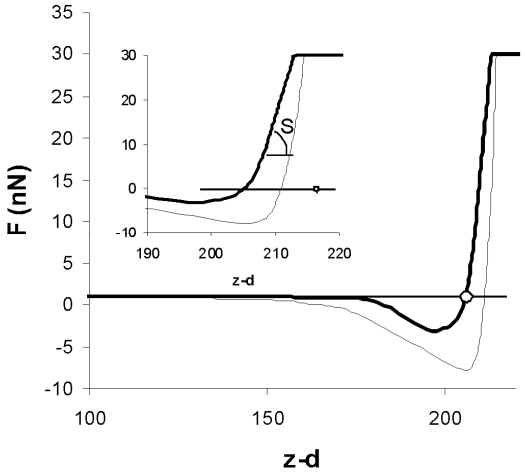

Figure 1.3. Measured force in an indentation AFM experiment against the difference between the *z* displacement of the sample and the cantilever deflection *d*. The thick line represents the indentation scan and the thin one the retraction. Insert indicates the uploading curve chosen for stiffness (*S*) calculations.

Figure 1.3 shows a typical loading-unloading curve. The thick line is obtained during indentation while the thin one corresponds to the retracting scan. The negative values of the force (attraction force between the tip and the surface due to van der Waals long-range interactions) are produced close to the contact point [80], which can be determined using the extrapolation shown in Figure 1.3 (i.e. it is the intersection point between the experimental curve and the horizontal reference assumed for absence of contact) [81]. At low values of *z-d* (penetration, *h*) there is no contact between the tip and the surface (both the deflection of the cantilever and the measured force are close to zero). For greater values of relative displacement *z-d*, short-range repulsive interactions surpass the attractive ones while material indentation goes on, making the force *F* increase. Ascribing the value of penetration zero to this point, the plot in Figure 1.3 can be

transformed into a force-penetration graph. The stiffness *S* is then defined as the slope of this graph.

Considering the indenter's shape, there are generally two different kinds of tips: sharp and blunt. Sharp tips normally have three-face pyramidal form which let a better definition of the contact area between tip and sample. On the contrary, blunt tips are generally rounded, with circular cross-sections, and they are used to obtain full stress-strain curves [25]. In this work it was used a sharp four-face pyramidal tip for nanoindentations assays.

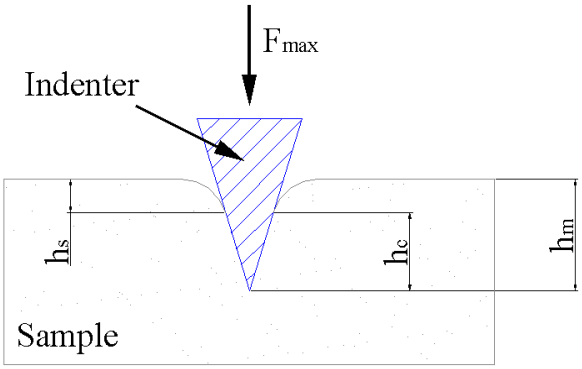

Figure 1.4. Sketch of indentation assessments.

There are some general limitations regarding the models used to obtain the elastic properties of the materials (Young modulus and Poisson ratio) just analyzing the load-unload curves (Figure 1.3). Some of them include the hypothesis of elastic recovery during the unloading process, which obviously does not apply when viscoelastic materials are assessed. Besides, it is assumed an elastic behavior along the assessments, but plastic deformation may take place during loading as well as other time dependent contributions to deformation (penetration). Additionally, the contact area between sample and tip is difficult to define because of local deformations which make the material sink-in or pile-up [25].

The unload curve can be fitted to a power law equation by a least square routine when a sharp indenter is used:

$$F = k(h - h_r)^m, \quad 1 < m < 2 \qquad \text{(Eq. 1.10)}$$

F is the applied load, *h* the penetration of the indenter, h_r the residual depth remaining after unloading and *m* a constant which defines the power law exponent which is related to the indenter's geometry. It is worthy of note that *m* describes how much curvature the unloading curve presents: for a flat punch *m* is equal to 1 (linear unloading); however, the larger the departure from linear behavior the higher *m* values. *k* takes into account geometric constants and the elastic properties (Young modulus and Poisson ratio) of sample and indenter. In order to avoid the blur of the unloading curve with time dependent deformations, some authors keep applied the maximum load during a few seconds and afterwards they analyzed the unloading curve [79]. The fitting routine of unloading curves must account for *m*, *k* and h_r. Once fitted, the stiffness (*S*) is analytically defined as the penetration derivative of the applied force at the maximum load:

$$S = \left.\frac{dF}{dh}\right|_{F\max} = km(h_{\max} - h_r)^{m-1} \qquad \text{(Eq. 1.11)}$$

where h_{max} is the penetration at maximum load (Figure 1.4).

The elastic properties of the composite can be obtained by defining a reduced modulus (E_r) which takes into account the deformation that the indenter bears. Thus, the elastic modulus (E_i) as well as the Poisson ratio (ν_i) of the tip's material is included on the definition of the reduced modulus by:

$$\frac{1}{E_r} = \frac{1-\nu_i^2}{E_i} + \frac{1-\nu^2}{E} \qquad \text{(Eq. 1.12)}$$

where E and ν are the Young modulus and Poisson ratio of the assessed material, respectively. In the case of soft samples and sufficiently rigid tips, Eq. 1.12 reduces to:

$$E_r = \frac{E}{1-\nu^2} \qquad \text{(Eq. 1.13)}$$

The relationship which finally correlates the measured stiffness (S) and the reduced modulus is

$$S = 2\lambda E_r \sqrt{\frac{A_c}{\pi}} \qquad \text{(Eq. 1.14)}$$

where A_c is the projected elastic contact area between sample and tip, and λ a correcting factor which depends on the tip geometry (λ=1.034 for a Berkovich tip) [25]. The contact area can be measured directly by microscopy of the indented surfaces (either scanning or transmission electron microscopy). However, the examined impression area does not consider the elastic and plastic recovery which occurs during the unloading. Other procedure tries to overcome this inconvenient by searching analytical functions which relate the cross-sectional area of the indenter with the distance from its tip (h). To do so, experimental procedures are reported in literature [77] which assumes that the elastic modulus does not depend on the indentation depth. This method implies indentation assays over aluminium surfaces at different indentation depths [77]. As a first estimate, it can be used the contact area due to a perfect Berkovich tip:

$$A_c = 24.5 h_c^{\,2} \qquad \text{(Eq. 1.15)}$$

which relates the contact area (A_c) as a function of the contact indentation depth (h_c). Further improvements of A_c can be made by series expansion around the value presented by Eq. 1.15 due to deviations of the Berkovich geometry [77].

Finally, the definition of h_c will determine the elastic properties of the indented sample. h_c can be defined as the difference between the penetration at the maximum load (h_{max}) and the residual depth remaining after unloading (h_r):

$$h_c = h_{\max} - h_r = h_{\max} - \frac{\varepsilon F_{\max}}{S} \qquad \text{(Eq. 1.16)}$$

ε is a function of the power law exponent m (Eq. 1.17). For instance, ε is equal to 1 for flat punch, and 0.75 for a tip whose cross-sectional area is described by a paraboloid of revolution.

$$\varepsilon = m\left[1 - \frac{1}{\sqrt{\pi}} \frac{\Gamma\left(\frac{1}{2(m-1)} + \frac{1}{2}\right)}{\Gamma\left(\frac{1}{2(m-1)} + 1\right)}\right] \qquad \text{(Eq. 1.17)}$$

1.8. Kinetics of the structural relaxation process in nanocomposites by Differential Scanning Calorimetry

Nanocomposites are systems that give unique opportunities to study the confinement effects on polymers, since polymeric macromolecules become trapped in small open spaces within filler porous structure. Polymer layered silicate nanocomposites exhibit a hybrid structure of alternating polymer-filler layers whose gallery (space left between neighbour silicate layers) can be tailored to obtain average sizes ranging from the radius of gyration of the polymer to the statistical polymeric length of the chains [39]. The large available conformation possibilities just changing that interlayer distance give rise to situations where the intercalated polymer chains form monolayers (i.e. single and extended polymer chains), or more bulky-like structures. Aside confinement effects, there is additionally an enhancement of the interactions between organic and inorganic phases which also hinder the bulk polymeric kinetics, the higher the lower the gallery distance (for polymer layered silicate nanocomposites).

Another attempt to use nanocomposites as model systems to study polymer confinement founds on an analogy between the behavior of immobilized chains around crystallites in semicrystalline polymers with polymer entrapment taking place on hybrid nanocomposites [82]. The issue whether the immobilized amorphous polymer chains around crystallites must relax before the onset of the crystalline phase melting or, on the contrary, the thermal structural instability of crystallites through their fusion allows the relaxation of the confined polymer chains, is difficult to clarify since both phenomena take place at the same temperature range [83]. Furthermore, through crystalline fusion the interaction between amorphous and crystalline phases changes. Dynamics of confined polymer chains can also be assessed with organic-inorganic nanocomposites, taking advantage of their large surface to volume ratio between counterparts. The sum of the hindered chains either around or laying on the surfaces of the inorganic phase becomes significant due to that huge interface, which in turn make the confinement phenomenon feasible to study in nanocomposites.

As previously mentioned, the polymer chains immobilization does not extend throughout the whole polymer matrix in hybrid systems; instead, the hindrance influence only ranges a few nanometers from the filler surface [82]. This interlayer with special properties differing from the bulk polymer (which plays a key role in the performance of the hybrid system [40]) is identified as the interphase. It can be distinguished two main sorts of interphases: those composed by completely immobilized polymeric chains (they do not devitrify at any temperature) and interphases formed by partly hindered polymer chains, which relaxes at higher temperatures giving rise to a second glass transition temperature or, at least, a shoulder at the high energy side of the relaxation main transition [73,82].

The glass transition temperature measured by Differential scanning calorimetry (DSC) is often used to evaluate changes in molecular dynamics in polymers. As a result of polymer-ceramic nanocomposite synthesis, the structural relaxation of the organic phase varies in such a way that the glass transition temperature may increase, decrease, remain the same, or even disappear, depending on the system [82]. However, the glass transition temperature alone is not conclusive regarding the nature of the confinement on polymers. Glass transition requires cooperative motions, which finally are detected by DSC as a step-like increase of heat capacity, whose intensity depends on the quantity which is relaxing. On the other hand, physical ageing assay utilizing the DSC technique is a useful procedure to study the enthalpy relaxation phenomenon since the experimental thermograms can be exploited not only by means of the calculation of the enthalpy relaxation at different annealing temperatures and times, but also by using phenomenological models with fitting parameters [84-90]. The later approach yields meaningful physical magnitudes by which the study of polymeric molecular dynamics is available.

The usual procedure to study isothermal enthalpy relaxation is to subject the sample to different thermal histories that start at a temperature T_0 higher than the glass transition temperature T_g (sample in thermodynamic equilibrium), then the sample is cooled at a constant rate to the annealing temperature T_a below or in the region of the glass transition and kept at this temperature for a time t_a. Next, the sample

is cooled to the temperature T_1 far below T_g and subsequently heated to T_0 at a constant rate. The structural relaxation process is usually measured as the recovery of the lost enthalpy associated with the glass transition event during the last heating scan. When an aged glass is heated through T_g to the rubbery state, the lost enthalpy is regained and this event can be observed as an endothermic peak (in the glass transition region) in the DSC profile that has a strong dependence on the previous thermal history, i.e. on T_a and on t_a. It can be shown that the enthalpy loss in the sample during the isothermal stage at T_a is equal to the area (from T_1 to T_0) between the heating thermogram measured immediately after the annealing process c_p, and the thermogram measured between the same temperatures in a scan without annealing, c_{pref}, the reference scan [91-93]:

$$\Delta H(T_a, t_a) = \int_{T_1}^{T_0} \left[c_p(\theta) - c_{pref}(\theta) \right] d\theta \qquad \text{(Eq. 1.18)}$$

Chapter 2

Materials and methods

2.1. Materials

The hybrid systems which were synthesized are focused on the reinforcement of the polymeric hydrogel PHEA by the inclusion of vitreous silica obtained by an acid catalyzed sol-gel process. The silica amount was systematically increased until an upper limit where the composite becomes brittle. Besides, the hydrophilic character of the organic phase was changed to assess its influence on the silica structure. To do so, increasing ethyl acrylate weights were added to the organic feeding solution of hydroxyethyl acrylate. The final organic phase forms a copolymer of both monomers, whose balance will determine the hydrophilicity of the nanocomposite. Besides, a procedure to obtain porous materials (scaffolds) made of these hybrid materials is described.

2.1.1. PHEA-silica nanocomposites

The nanocomposite samples were obtained by the simultaneous polymerization of HEA and TEOS (Figure 2.1) as described in [29] for the case of the similar polymer poly(2-hydroxyethyl methacrylate) but without the presence of ethanol as solvent. The matrix undergoes a

free radical polymerization and the silica phase polymerizes following a sol-gel process. TEOS reaction was acid catalyzed in a water/hydrochloric acid solution by keeping the molar ratios HCl/TEOS equal to 1.85×10^{-2} and the H_2O/TEOS ratio equal to 2. The silica content was changed from 5 to 10, 15, 20, 25 and 30wt% by controlling the HEA/TEOS ratio and assuming that the sol-gel reactions were complete (Eq. 1.9). Benzoyl peroxide, BPO (97%, Fluka) in a proportion 2 wt% of HEA mass, was used as thermal initiator of the organic polymerization. All the chemicals were used as supplied.

Chemicals were used without further purification. HEA (96%, Aldrich) was mixed with BPO and mechanically stirred for 30 minutes. In parallel, TEOS (98%, Aldrich) was added to a hydrochloric acid solution (HCl, 37%, Aldrich) and distilled water, and stirred for 30 minutes[i]. Then both solutions were mixed together and stirred for another 30 minutes.

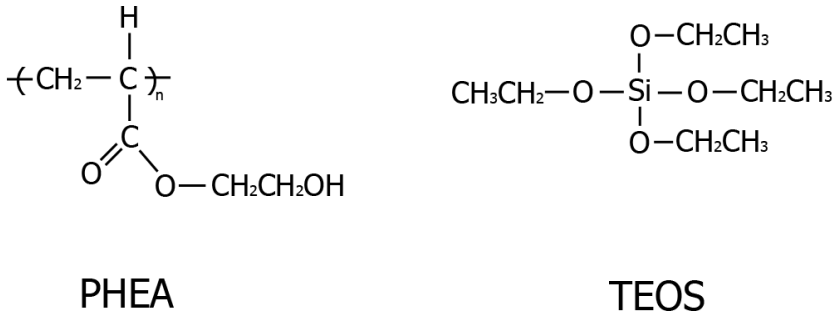

Figure 2.1. Chemical structures of PHEA monomeric unit and the silica precursor tetraethoxysilane (TEOS).

The polymerisation process was carried out at 60ºC for 21 hours, and then completed with a post-polymerization stage at 90ºC for 18 hours. Finally, the samples were rinsed in boiling distilled water

[i] Due to the thermodynamic inmiscibility at room temperature between water and TEOS [27,28], sol-gel reactions must begin in order to produce silanols before the solution becomes homogeneous.

for 24 hours to remove residuals and unreacted monomers, and dried *in vacuo* at 60ºC until constant weight.

Pure silica and homopolymer PHEA samples were also synthesized following the same procedures as described above, but in the absence of HEA in the case of silica, and without HCl/TEOS/water solution for neat PHEA.

2.1.2. Copolymer nanocomposites

The same methodology to synthesize PHEA-silica polymer nanocomposites was used to produce hybrids with controlled hydrophilic character: instead of a HEA solution (HEA+BPO), the feeding monomers which finally polymerize to yield the organic phase are a mixture of HEA and ethyl acrylate (hereafter EA, 99% pure, Aldrich). The HEA/EA ratio was systematically varied to obtain materials with different organic matrices, avoiding the appearance of macro-phase separation (materials must remain transparent regardless their silica content). *-OH_x* will account for the HEA amount relative to the organic phase (for instance *-OH_{30}* identifies the nanocomposite whose HEA/EA percentages equal 30/70). The synthesized hybrids as regards the organic phase are *OH_{10}*, *OH_{30}*, *OH_{50}*, *OH_{70}*, *OH_{90}*, where the former composition concerns to the highest hydrophobic system.

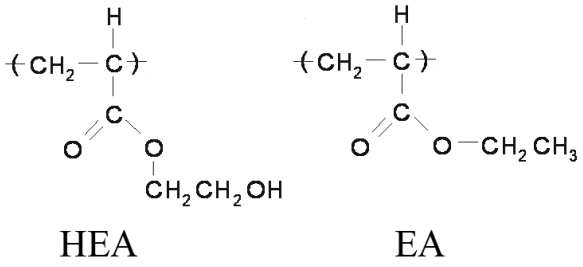

Figure 2.2. Schematic chemical structure of monomers 2-hydroxethyl acrylate (HEA) and ethyl acrylate (EA).

2.1.3. Nanocomposite scaffolds

Different numbers of polyamide 6 sheets of commercial textile fabrics (SAATI S.A., Barcelona, Spain) were used to build well-ordered structures to serve as porogenic templates. The employed fabric has a nominal thread diameter equal to 80 micrometers with a mesh opening of 160 micrometers. The thickness of the fabric is 144 micrometers (Figure 2.3).

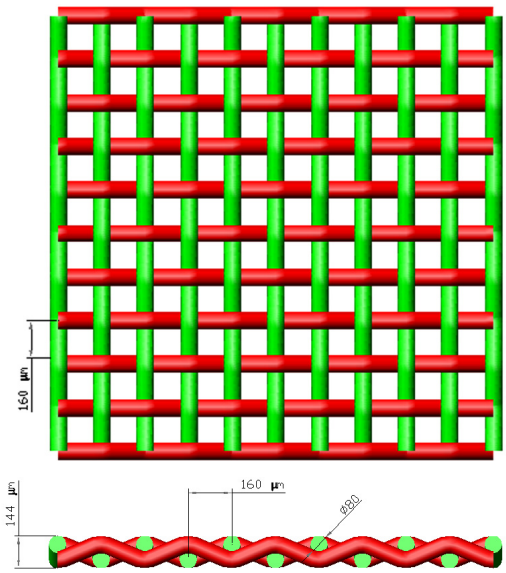

Figure 2.3. Dimensions detail of a commercial fabric with woven threads.

For obtaining the templates [94] a two-step process was performed which included compression and sintering. Previous to compression, squares of 100×100mm dimensions of the commercial fabrics were cut and stacked. Simultaneous heating and compression were applied during 15 minutes in a hydraulic plate press on these stacks, made up of 8 and 16 sheets. The temperature during compression was approximately 25ºC lower than the measured onset temperature of the melting peak for polyamide 6 (T_{onset} = 245ºC

measured by DSC heating at 10ºC/min). This temperature was kept constant during the process. The compression weight was varied and ranged between $4x10^3$ and 16 $x10^3$ kg. Afterwards, a sintering process was carried out in an oven at a well-controlled temperature slightly higher than T_{onset} for 45 minutes, keeping a low compression stress while sintering.

The filling of the available spaces within the templates was carried out by immersion of the produced templates into the reactant solutions described above. After polymerization took place, a composite material was formed in which the polyamide template was embedded inside the hybrid organic-inorganic matrix. The polyamide 6 template was then dissolved by immersion at room temperature in nitric acid (Aldrich, 30% extra pure) for 4 days with several changes of the acid. A previous grinding of the front exterior surface was done to enhance the speed of penetration of the acid. Since the compression and sintering process has ensured the continuity of the polyamide template, access to it by the solvent and the ensuing removal of the polyamide threads by dissolution is complete. After this step, the resulting porous materials were rinsed in boiling distilled water to remove any remaining chemicals. Finally, the scaffolds were dried *in vacuo* at 70ºC to constant weight.

2.2. Experimental techniques

Following sections will describe the experimental techniques used in order to characterize both bulk materials and scaffolds. Some of them are used for the characterization of both systems, hybrids and porous materials (such as several microscopy techniques, dynamic-mechanical spectroscopy, and so on), while there are others which are specific for only one of them (for instance mercury porosimetry for scaffolds).

2.2.1. Density and solvent uptake measurements

Hybrids density was determined through Archimedes' Principle by weighing dried samples in air (*P*) and immersed in n-octane (*P'*) (99%, Aldrich, 0.708 g/cm^3) using a 10^{-5} g sensitivity Mettler Toledo AX205 balance with a density accessory kit. Each determination was repeated three times for each sample. The equation used to compute the materials density is given by:

$$\rho_{mat} = \rho_{oct}\left(\frac{P}{P - P'}\right) \qquad \text{(Eq. 2.1)}$$

where ρ_{mat} and ρ_{oct} are the densities of the material and n-octane, respectively.

For the solvent uptake measurements, dried samples were weighed before and after being immersed in two different solvents, distilled water (reagent grade, Scharlau) and acetone (synthesis grade, Scharlau), at room temperature for 3 days. Measurements were repeated three times for each material. The equation used to compute the equilibrium solvent uptakes (*ESC*) is given by:

$$ESC = \frac{m_{sol}}{m_{dry}} \times 100 = \frac{m_{sw} - m_{dry}}{m_{dry}} \times 100 \qquad \text{(Eq. 2.2)}$$

where m_{sol} is the mass of the liquid which swells the material, and m_{dry} and m_{sw} the bulk material masses before and after the immersion, respectively. For nanocomposites, it is considered that the solvent amount absorbed by the silica phase is much lesser than that of the organic phase, and thus the *ESC* results will be referred to the polymer rather than to the sample mass.

2.2.2. Fourier transform infrared spectroscopy (FTIR)

Fourier transform infrared spectra were obtained at room temperature in the Attenuated Total Reflectance (ATR) mode between 600 and 4000 cm^{-1} with a Nexus spectrometer (Nicolet Instruments LTD, Warwick, UK), operating with a 4 cm^{-1} resolution. All the spectra shown are the average of 32 scans for each dried specimen.

2.2.3. Dynamic mechanical analysis (DMA)

Dynamic mechanical measurements were performed in a DMS210 Seiko analyzer in the stretching mode. Samples with rectangular geometry and dimensions of $20\times4\times0.7$ mm were used. Two kinds of measurements were performed: on completely dry samples scans were conducted at a constant heating rate of 2ºC/min at a frequency of 1 Hz over a temperature interval ranging from -120 to 180ºC; and isothermal measurements previously performed at 25ºC and 1 Hz over swollen samples equilibrated for three days in distilled water at room temperature.

Similar conditions apply to the characterization of the mechanical properties of the scaffolds. However, due to their pore structure anisotropy, samples were cut along one of the two possible main axis defined by the cylindrical pores so as to be stretched on this direction (i.e. the largest probe dimension for DMA assays coincides with the pore direction shown in Figure 3.37).

2.2.4. Thermogravimetric analysis (TGA)

Thermal stability and final silica content of hybrids were investigated with a SDT Q600 analyzer (TA Instruments, United States) under a nitrogen flow of 50 ml/min at a heating rate of 20ºC/min, starting from 50ºC up to 700ºC. The TGA temperature was calibrated

with zinc and indium and the heat flow with sapphire. Dried sample weights varied from 5 to 10 mg.

2.2.5. Scanning electron microscopy (SEM)

Scanning electron micrographs were taken in a JEOL JSM6300 microscope. Samples were coated with gold (for secondary electron images) or carbon (for x-ray microanalysis and back-scattered electron images) by sputtering. Micrographs were taken at an accelerating voltage of either 20 kV to reveal topography features (secondary images) or 10 kV (for microanalysis and back-scattered electron micrographs).

X-ray microanalysis mapping was performed with an Energy Dispersive x-ray Spectrometer (EDS) from Oxford Instruments attached to the SEM. Three different areas were examined of cryo-fractured surfaces. Only the intensity of the energy region of the x-ray emission spectra corresponding to silicon was collected. Silicon signal was corrected subtracting the background signal collected immediately above the silicon intensity peak (between 1.2 and 1.5 eV). The EDS images were the result of 50 frames of collection (same exposition times).

2.2.6. Transmission electron microscopy (TEM)

Transmission electron microscopy was performed in a Fei Tecnai Spirit at an accelerating voltage of 60 kV. Samples were cryo-cut with an approximate thickness of 80 nm. No additional dye was added to distinguish the inorganic from the organic phase.

2.2.7. Optical properties

Refractive index was measured in air with a Shibuya Abbe-type refractometer at wavelengths corresponding to visible light. Refractive index was measured on samples previously dried (n_{dry}) and on samples swollen to equilibrium in distilled water (n_{sw}). Measurements were done on 5 different specimens. The refractive index average and the corresponding standard deviation were computed.

2.2.8. Differential scanning calorimetry (DSC)

Differential scanning calorimetry (DSC) was performed in a Pyris 1 apparatus (PerkinElmer). Nitrogen gas was let through the DSC cell with a flow rate of 20ml/min. The temperature of the equipment was calibrated by using Indium and Zinc. The melting heat of Indium was used for calibrating the heat flow.

The characteristic transition temperatures have been calculated from the DSC curves. For the glass transition of all samples, the temperature of the intersection between the extrapolation of the enthalpic liquid and glass lines has been taken. Computing Eq. 2.3 gives the solution for T_g, where T_1 and T_0 are temperatures below and above T_g, respectively, and $c_p\big|_g$ and $c_p\big|_l$ the specific heat capacities of the glass and liquid states.

$$\int_{T_1}^{Tg}\left(c_p - c_p\big|_g\right)d\theta = \int_{Tg}^{T_0}\left(c_p\big|_l - c_p\right)d\theta \qquad \text{(Eq. 2.3)}$$

$c_p\big|_g$ and $c_p\big|_l$ may be defined by linear regression fits to experimental data well below and above T_g, respectively. It gives rise to errors in the slopes and intercepts which define the heat capacities lines of the glass and liquid states. An estimate of the glass transition temperature error may be computed just assuming the slope and

intercept values which give the lowest and the highest T_g value. Their difference is then assumed to be a good estimation of the error for glass transition temperature measurement.

The width of the glass transition (ΔT_g) was characterized by the temperature interval determined by the intersection of the tangent to the thermogram at the inflection point with the glass and liquid lines. Its measurement error can be analytically computed once $c_p\big|_g$ and $c_p\big|_l$ lines were defined by linear regression fits, assuming an error propagation law.

The normalized heat flow, which has heat capacity units, is obtained by dividing the heat flow as obtained from the apparatus by the mass of the sample and the heating rate, and was employed instead of the absolute value of the specific heat capacity. The specific heat capacity increment at the glass transition ($\Delta c_p\big|_{Tg}$) was determined as the difference between the intersections of the extrapolated glass and liquid lines at T_g. The reported measurement error for $\Delta c_p\big|_{Tg}$ is the difference between the two extreme situations which lead to the highest and lowest heat capacity increment values once $c_p\big|_g$ and $c_p\big|_l$ lines were defined by linear regression fits.

Before measures, samples were dried under vacuum until constant weight and hermetically sealed in aluminium pans, with masses ranging between 5 and 10 mg.

2.2.8.a. Standard heating scans

After erasing the effects of any previous thermal history by heating above the glass-transition temperature (T_g), the samples were subjected to a cooling scan down to -40ºC at 40ºC/min, followed by a heating scan from that temperature up to 140ºC at a rate of 10ºC/min.

2.2.8.b. Physical ageing assays

The thermal history started at 125°C (T_0) for all the samples. Then the sample was cooled to different temperatures T_a at a cooling rate of 40ºC/min and kept isothermally for a time t_a during 200 min. Next, the sample was cooled to -30°C (T_1) at a cooling rate of 40ºC/min, and finally heated to T_0 at a heating rate of 10ºC/min. Immediately after each of these experiments a heating reference scan at 10ºC/min was performed after cooling the sample from the highest to the lowest temperature (from T_0 to T_1) at 40ºC/min. A sketch of the process is shown in Figure 2.4. In this way the baseline of the DSC corresponding to the annealing and the reference scans are nearly identical and the position of the sample in the sample holder of the DSC is the same as well. The difference between both scans is zero with great accuracy at the start and the end of the thermogram.

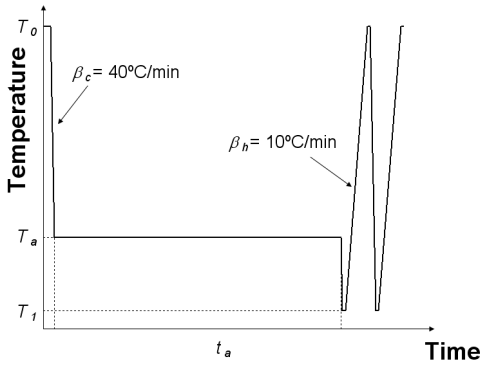

Figure 2.4. Sketch of the thermal history applied in the annealing process, including the annealed and reference scans.

Samples were also subjected, without annealing, to a set of scans at different cooling rates from T_0 to T_1 (0.5, 1, 2, 5, 10, 20 and 40ºC/min) before a heating scan from T_1 to T_0 at a heating rate of 10ºC/min.

2.2.9. Atomic Force Microscopy (AFM)

2.2.9.a. Tapping mode

AFM was performed in a NanoScope III from Digital Instruments (Santa Barbara, CA, USA) operating in tapping mode in air. Silicon-cantilevers from Nanoworld were used with force constant of 2.8 N/m and nominal resonance frequency of 75 kHz. The phase signal was set to zero at 5-10% lower than the resonance frequency of the tip, as suggested by manufacturer. Drive amplitude was 360 mV and the amplitude setpoint 1.4 V. Samples were cryo-fractured and the resulting surfaces exposed to the AFM so as to collect tapping mode images.

In the tapping mode AFM, a cantilever oscillates with the probing tip close to its free resonance frequency with given amplitude. The interaction between the sample and the probe gives rise to a shift in the probe vibration respective to that measured in a free oscillation, i.e., with the probe far away from the sample. The vertical displacement (height) needed to keep the set amplitude provides information about the topography of the system. On another hand, the measured phase shift may be caused by differences in the viscoelastic properties (in fact with different capabilities of energy damping) in different parts (or phases) of the sample, and therefore it can provide some information about the morphology of the system. However, differences in phase lag may be caused not only by the occurrence of different phases, but also by geometric features (such as edges, steps-like features, etc), induced by the system topography. There are several strategies for programming the apparatus parameters so as to obtain either accurate surface topographies (height) or morphologies (phase). Recent studies have shown that only when the amplitude of the vibrating cantilever is programmed to be equal to that of the free cantilever (or really close to it) the height of the topography represents a true surface topography since if not surface is deformed by tip's touch [95], and that a much harder tapping is necessary to observe maximum phase shift contrast between stiff and soft regions of the material. Thus, the AFM was set to perform a *soft* tapping when topography (height signal) was the parameter to study: it means a

ratio between the free oscillation of the cantilever (A_0) and the set point amplitude (A_{sp}), $r_{sp}=A_{sp}/A_0$, around 0.9. On the contrary, to observe good phase contrast between regions with different viscoelastic properties, a *hard* tapping mode has been suggested, keeping r_{sp} around 0.5 [96]. Several AFM scans were performed on PHEA-based nanocomposites with different values of the r_{sp} parameter and the highest contrast for phase signal was obtained at moderate high pressures r_{sp} ~0.6, which was the value used for obtaining tapping mode images.

Probe tip shape influences the obtained AFM images, which are finally a convolution of the geometry of both sample topography and probe. It is known that despite the high vertical resolution of the AFM, the contact between material surface and tip does not always take place at the probe's apex and, as a result, surface features circa those corresponding to the tip are widened and thus overestimated [97]. However, our work does not focus on the quantification of silica sizes, where the aforementioned overestimation can yield incorrect results. Instead, we try to compare results after different treatments or synthesis procedures, and so AFM image deconvolution was not performed.

2.2.9.b. Nanoindentation assays

Indentation experiments were also conducted with the AFM but for nanoindentation it was used a Veeco square pyramidal tip OTR8 with a spring constant 0.57 N/m (datum supplied by the manufacturer) and tip half angle 35º. Calibration of the tip sensibility was performed in the same conditions than the experiments with a flat surface sample made of the same material than the tip, and was calculated to be 5.721 nm/V after at least 10 repetitions. Sensitivity of the tip was used for correcting the deflection of the tip due to the vertical movement of the sample without penetration. The plateau around 30 N/m in Figure 1.3 is a consequence of the deflection limit imposed in the experiment (20 V). Samples for indentation experiments were sheets of the nanocomposites, around one micrometer thick, cut with a microtome

and glued on a stiff surface. All experiments were performed with the instrument mounted on a vibration isolation system.

Indentation experiments were performed in a series of 50 points located on a straight line and separated 10 nm from each other, covering a distance of 490 nm. The experiments were repeated on five parallel lines separated 20 nm from each other. Thus, the stiffness is measured over a square of 80 x 490 nm.

2.2.10. Scaffold porosity

Scaffold porosity was evaluated by two different experimental methods: the apparent density method and mercury intrusion porosimetry. The former allows the measurement of porosity on dried and swollen scaffolds, running statistical analysis for porosity in a non-destructive way; the latter additionally gives other important parameters, such as the pore size distribution, tortuosity,… but only with dried samples; however, samples are useless after measuring.

2.2.10.a. The apparent density method

Porosity (π) is defined as the ratio between the volume of pores (V_{pores}) and total volume (V_T):

$$\pi = \frac{V_{pores}}{V_T} = \frac{V_T - V_{polymer}}{V_T} = 1 - \frac{v_{polymer}}{v_T} \qquad \text{(Eq. 2.4)}$$

where the specific volume of the polymer ($v_{polymer}$) is equal to the inverse of its density, and the specific total volume (v_T) is the quotient between the total volume and the scaffold mass. With the aim to evaluate porosity, dried scaffolds were cut in the form of squares as regular as possible, measuring their apparent volumes geometrically.

The same porous samples were weighed in a Mettler AX205 balance with a sensitivity of 0.01 mg. Taking advantage of the previously measured densities of the bulk materials, porosity calculations were done for at least three times of each different scaffold. Porosity values determined in this way were reproducible up to 7%.

2.2.10.b. Mercury porosimetry

Mercury porosimetry was performed in a PoreMaster PM-33-11 porosimetry analyzer (Quantachrome Instruments, Florida, USA). Porous samples were kept dried before measurements, with masses ranging from 3 to 5 mg. The mercury intrusion and extrusion volumes were recorded while increasing (or decreasing) the pressure from 6.9 to 344.7 kPa. The surface tension and contact angle of mercury was set to 480 mJ/m^2 and 140º, respectively.

Washburn equation was used to correlate applied pressure (p) with pore radius (r) (Eq. 2.3). It is outcome of relating, on one side, the work needed to force mercury to enter into a cylindrical pore at a defined pressure and, on the other hand, the work necessary to create new mercury area because of the cylinder filling.

$$pr = -2\gamma\cos(\vartheta) \qquad \text{(Eq. 2.5)}$$

where γ is the mercury surface tension and ϑ the contact angle. Besides, pore size distributions (per volume, surface and length) were computed assuming cylindrical pore shapes, since it suits well with the scaffold structure. They are defined by Eq 2.4, Eq. 2.5 and Eq. 2.6.

$$dV = D_V(r)dr \Rightarrow D_V(r) = -\frac{p}{V}\frac{dV}{dp} \qquad \text{(Eq. 2.6)}$$

$$dS = D_S(r)dr \Rightarrow D_S(r) = \frac{D_V(r)}{r} \quad \text{(Eq. 2.7)}$$

$$dL = D_L(r)dr \Rightarrow D_L(r) = \frac{D_V(r)}{r^2\pi} \quad \text{(Eq. 2.8)}$$

Finally, pore tortuosity (τ_{pore}, Eq. 2.7) is a dimensionless parameter which lumps together all deviations from straight diffusion paths [98]. It is useful when calculating the scaffold apparent diffusion coefficient which is related in turn to material's bulk diffusion.

$$\tau_{pore} = 2.23 - 1.13 V_{Hg} \rho_{mat} \quad \text{(Eq. 2.9)}$$

V_{Hg} is the mercury volume intruded at the maximum applied pressure and ρ_{mat} the bulk density of the material.

2.2.11. Pyrolysis

Pyrolysis was performed in a tubular electric oven with a temperature-time regulator (Gallur, Valencia, Spain). The process consisted in two stages, first raising the temperature up to 650ºC at a very slow heating rate to avoid cracking, and second an isothermal step at 650ºC for 3 hours to erase any remaining organic trace.

2.2.12. Computer simulation of the scaffolds pore structure

The geometry of the employed fabric was simulated using AutoCad®. A model sheet was copied and pasted in order to mimic the actual stack of fabrics. The distance between neighbouring sheets was

varied so that the compression process could be simulated. Finally, the pore structure was obtained by subtraction of the stacked fabrics from a solid cube. An estimate of the theoretical porosity was also calculated making use of these computer simulations.

2.2.13. Silica dissolution

Pure silica synthesized from TEOS as well as the SiO_2 phase in nanocomposites were dissolved by a concentrated solution of sodium hydroxide (hereinafter NaOH, Panreac) at room temperature after 3 hours of immersion at pH equal to 11.6.

Chapter 3

Results and discussion

3.1. Silica structure on PHEA-derived nanocomposites

3.1.1. The silica size

The synthesized nanocomposite materials retain the transparency of pure PHEA. This indicates that the characteristic size of the silica phase is small enough (less than a few hundred nanometers) not to disperse light [29,46,59,99], otherwise the samples would be translucent. This fine-grained structure of the silica phase is typical of acid catalyzed polymerization of the silica precursor in presence of less water than the stoichiometrical amount [16,20], in agreement with the results of Jackson et al obtained with the same organic matrix but in different polymerization conditions [59].

A direct observation of the silica phase on nanocomposite slices is shown in Figure 3.1 by TEM images. Micrographs of neat PHEA did not reveal meaningful features (data not included). However, silica phase can be distinguished from the polymer as darker areas throughout the sample even though no dye was added to highlight one phase [29,59,100,101]. The contrast between inorganic and organic phases is especially marked for low silica amounts (Figure 3.1a and b). As the inorganic fraction increases, the silica features become harder to

identify until they finally are so smeared that are no longer distinguishable (Figure 3.1c and d). During the hybrids polymerization there is always a phase separation due to the formation of the biphasic composite. Indeed, it is reported that silica polymerization must be faster than that of PHEA in order to avoid a macro-phase separation (i.e. micro- instead of nano-aggregates of SiO_2) [59].

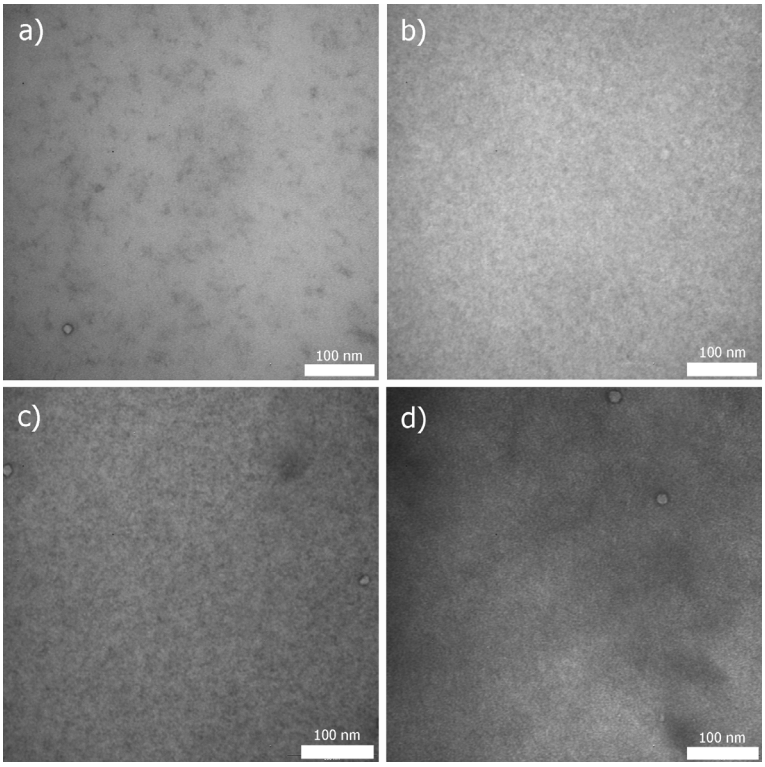

Figure 3.1. Representative TEM images for PHEA-based nanocomposites at 120000x with different silica contents: a) 5wt%; b) 10wt%; c) 15wt%; d) 30wt% silica.

Hajji et al studied similar hybrid systems but using PHEMA instead of PHEA [29]. They concluded that the silica amount influences the final silica morphology: small angle x-ray scattering (SAXS) assays showed that the lower the silica content (below the silica percolation) the larger the SiO_2 size. It is in agreement with the ease to identify

silica rich-domains by TEM (Figure 3.1) as well as by higher bright areas ascribed to silica (Figure 3.8) in samples with low silica amounts.

At low silica percentages (5 and 10wt%), dispersed silica nuclei begin to grow, forming SiO_2 single porous nanoaggregates or nanoparticles with the corresponding condensation degree determined by the polymerization conditions (in the present situation, linear rather than branched polymer species [16,18,20,102]) and the HEA molecules acting as a non-surfactant templating liquid [99,103,104]. When close single particles coalesce, they form not completely stacked aggregates with holes within (Figure 3.2); this may have a reflection in the contrast of TEM images, due to an easier passage of the electron beams when the phase is porous. The same process takes place at higher silica percentages, but this time there are more numerous particle aggregates which finally contact each other, until a silica threshold from which biphasic co-continuity is established.

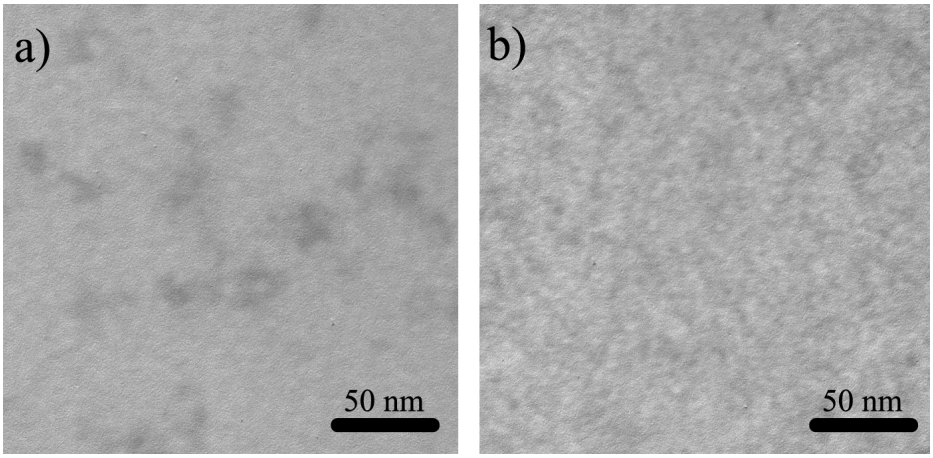

Figure 3.2. Detail of TEM micrographs for hybrids with: a) 5wt% and b) 10wt%.

Figure 3.3 shows both the refractive index for dry (n_{dry}) and swollen (n_{sw}) samples. The refractive index is larger for the dry than for the swollen samples, these having values close to that of water. It first slightly increases in the case of the dry samples until a silica percentage of 10%, and from this content on, it smoothly. By contrast,

for the swollen samples there is a sharp fall of the refractive index at the smallest silica percentages, which then remains almost constant for the rest of silica contents, except for 10wt% which is even higher than for pure PHEA.

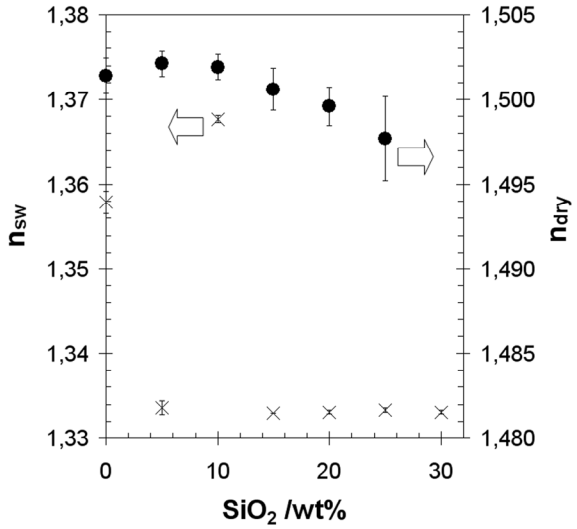

Figure 3.3. Silica content dependence of the refractive index for dry (●) and swollen (×) samples at wavelengths corresponding to visible light. Average is presented with its standard deviation as error bars.

Figure 3.4 shows the topography of the hybrid materials as seen by AFM. Different areas of 2x2 μm were scanned so that reproducible images were obtained. Nanoscale common features can be observed in both images with different silica contents, like an aggregation of small particles of around 40 nm. Nevertheless, those aggregates should be an intimate mixture of silica and polymer phases since they do not appear in TEM images as larger as it does in AFM topography images (Figure 3.1).

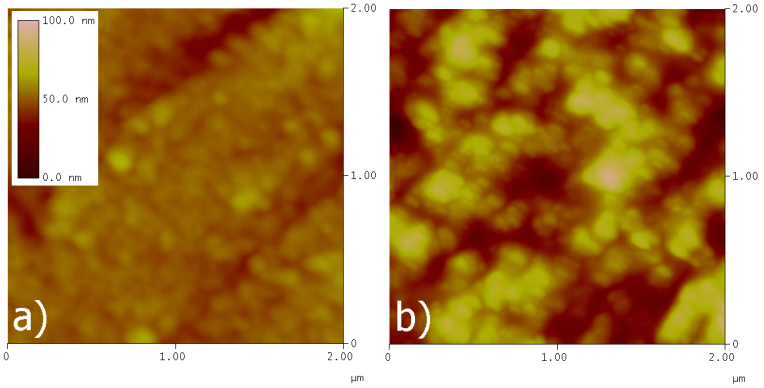

Figure 3.4. AFM surface topography of hybrid materials: (a) PHEA+15wt% silica and (b) PHEA+30wt% silica. Both images share the scale.

Another attempt to assess the silica size consisted on the remove of the organic nanocomposite phase by pyrolysis. Figure 3.5 shows the AFM topography of the silica residue after a TGA assay of nanocomposite with 15wt% silica. Residues after pyrolysis retain the shapes of the original samples but somehow shrunk, and are continuous even for small percentages of silica [59]. However, the dimensional changes undergone by the samples after the thermal degradation of the organic phase are more significant for those hybrids with lower silica contents. The continuity of residues points out that nanocomposites must consist in two phases, both of them in the form of networks, finely interdispersed or interpenetrated. However, pyrolysis changes the silica network structure by sintering it to a glass [18]; nonetheless, high magnification of the residues (Figure 3.5) clearly shows a structure of aggregated silica nano-particles with dimensions in the order of tens of nanometers, which give an estimate of the size of the silica-rich phase in nanocomposites (Appendix 1 for more images).

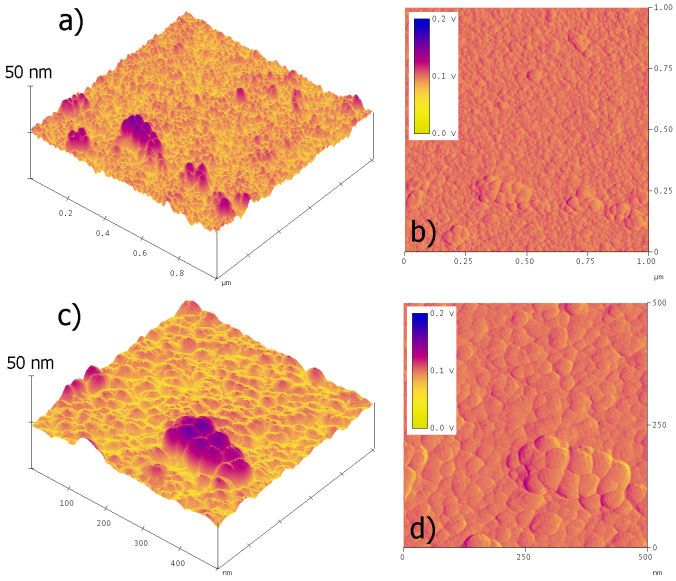

Figure 3.5. Tapping Mode AFM height (a-c) and amplitude (b-d) signals of the TGA residues of PHEA-15wt% nanocomposite at 1x1 μm and 500x500 nm.

In order to avoid the sintering effect which may be induced by pyrolysis, amorphous silica was also obtained by a direct polymerization of TEOS at the same polymerizing conditions as those used for nanocomposites (i.e. same ratio of [TEOS]/[H_2O], in acidic conditions and thermal procedure), but without HEA addition; such silica will be used in future comparisons with nanocomposites as well. Figure 3.6 shows the AFM topography of pure silica obtained by this way. There are not significant differences of topography or average particle size in comparison with silica residues (Figure 3.5).

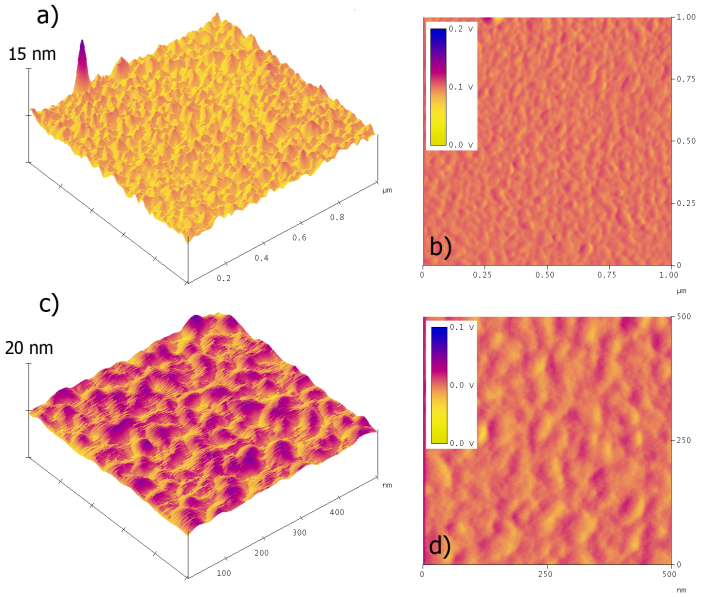

Figure 3.6. Tapping Mode AFM height (a-c) and amplitude (b-d) signals of silica obtained by a direct TEOS polymerization with the same polymerizing conditions as those used for nanocomposites.

To synthesize mesoporous silicas, some molecules are needed to act as templates so as to obtain well ordered porous structures at nano-scale, sometimes even with periodic porous orders [105-108]. However, when amorphous silica is obtained by sol-gel reactions at low temperature conditions (Figure 3.6), there are not molecules (or oligomers) of HEA acting as templates when silica undergoes the transition from sol to gel [18] as happens in nanocomposites, and perhaps different inorganic structures may be synthesized if compared with the synthesis method of mesoporous silicas. To evaluate whether HEA molecules have an influence on the final silica structure or not, different silicas were gelified at room temperature in the presence of the monomer 2-hydroxyethyl acrylate, avoiding its polymerization (no thermal initiator was added). Figure 3.7 shows the AFM topography of silicas polymerized in the presence of 70 and 85wt% HEA (it means a 30 and 15wt% silica, respectively). Again, no significant change in the nano-particle size and structure was ascertained when comparing with

either silica observed after pyrolysis (Figure 3.5) or silica polymerized following the same thermal procedure as hybrids (Figure 3.6).

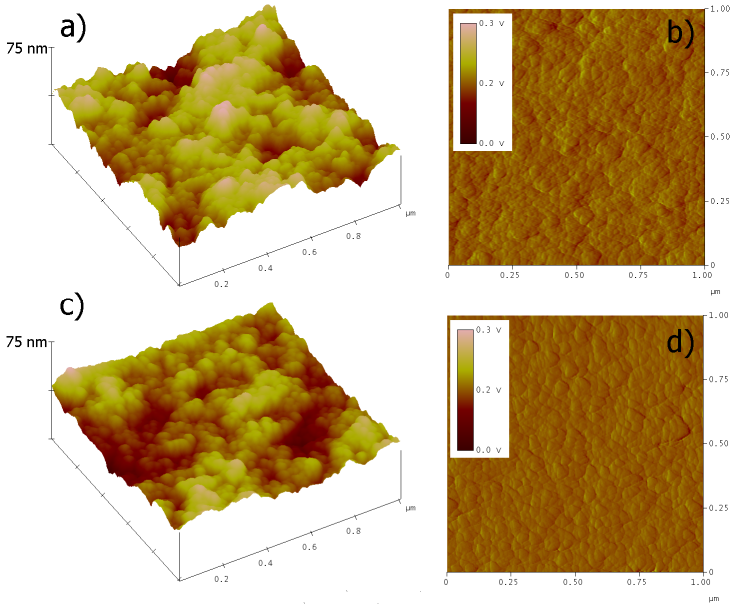

Figure 3.7. AFM images of the topography (a and c) and amplitude (b and d) signals of silicas gelified in the presence of a variable HEA amount: 85wt% HEA (a and b); 70wt% HEA (c and d).

3.1.2. Silica dispersion on PHEA-based sol-gel hybrid systems

TEM images (Figure 3.1) reveal that silica is widely spread regardless silica content. Another related issue is the content dependency of the silica structure, as previously commented when TEM images were introduced: nanocomposites with low silica percentages show more defined silica boundaries compared with higher inorganic contents. Nevertheless, whatever the silica content, heterogeneity only takes place at nanoscale, with no segregation phenomena at higher levels.

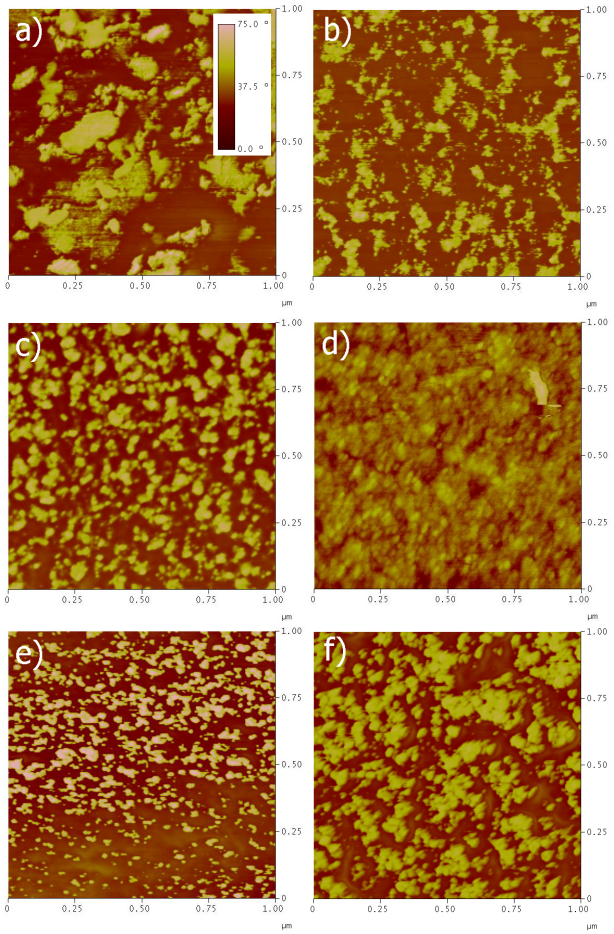

Figure 3.8. AFM phase image (tapping mode) of the PHEA/silica hybrid nanocomposites scanning 1x1 µm area. Different mass fraction of silica: (a) 5 wt%, (b) 10 wt%, (c) 15 wt%, (d) 20 wt%, (e) 25 wt%, (f) 30 wt%.

Another microscopy technique, AFM, was also used to obtain further information about silica distribution, but this time exploiting the phase lag signal. Figure 3.8 shows the AFM phase images of the hybrid systems after scanning a 1x1 µm area. Different areas of each sample were scanned, and the images shown in Figure 3.8 are representative of the material and reproducible at different magnifications. It is known that the phase lag which the tip undergoes when contacting with a surface is a magnitude sensitive to composition variations in the

material, what makes it appropriate for showing the underlying structure of the system [96,104,109-113]. Indeed, the AFM tapping mode phase pictures show the heterogeneity of the energy dissipation capability of the material surface. Even at high values of the parameter r_{sp}, the response of the material is due to a very thin layer close to the surface. Two qualitatively different main areas can be identified in each one of the images. The bright zones are ascribed to regions of higher stiffness in the material that would correspond to silica-rich zones, while the dark areas would correspond to softer domains [95,105]. Up to silica contents of 15 wt%, isolated bright regions without interconnections are present in the samples. For the nanocomposite with silica content 20 wt%, these particles seem to start interconnecting, but still a co-continuous structure cannot be inferred from the AFM images.

To provide morphological evidences of the dispersion of silica within these hybrid systems but at lower magnifications (micro-scale), an elemental microanalysis study was performed. Figure 3.9 shows the cryo-fractures and x-ray microanalysis of hybrid materials with 10, 20 and 30wt% of silica content. The silicon distribution (white spots) attached to the SEM micrographs seem to be uniform throughout the sample, with lower density in samples with less silica. The silica phase seems to be uniformly distributed at the micro-scale. In interpreting Figure 3.9 it must be taken into account that it shows not only the silica aggregates at the surface, but also some from a finite in-depth volume layer, since the high energy electron beam impinging on top of a surface penetrates a few micrometers; the ensuing x-rays emitted thus stem from a volume (around 1 μm^3), and not from a surface [106]. It is also noteworthy that x-ray microanalysis resolution is not as high as that for secondary electron micrographs [106]. Thus the silica distribution shown in Figure 3.9 represents a coarsened image of the true silica distribution at the nanoscale, but is sufficient to infer the uniformity of the silica-rich domains throughout the sample. Back-scattered electron images (here not reported) confirmed this uniformity, but did not add any relevant insight regarding the silica distribution since they did not show any feature besides topography (up to magnifications equal to 10000x). Small angle X-ray scattering (SAXS) is not only used to quantify different morphologies of fillers in

nanocomposites, but also to assess their distribution. Hajji et al performed SAXS in nanocomposite sol-gel hybrid systems similar to those studied in this work, but using PHEMA instead of PHEA as organic phase [29]. Their results regarding silica distribution yielded by SAXS assays agree with those reported here. Jackson et al also carried out SAXS measures but on PHEA-silica sol-gel nanocomposites at different synthesis conditions [59]: hydrofluoric acid instead of hydrochloric acid as catalyst and a stochiometric water amount (H_2O/TEOS=4). However, their conclusion regarding silica distribution is the same which is previously stated in this paragraph.

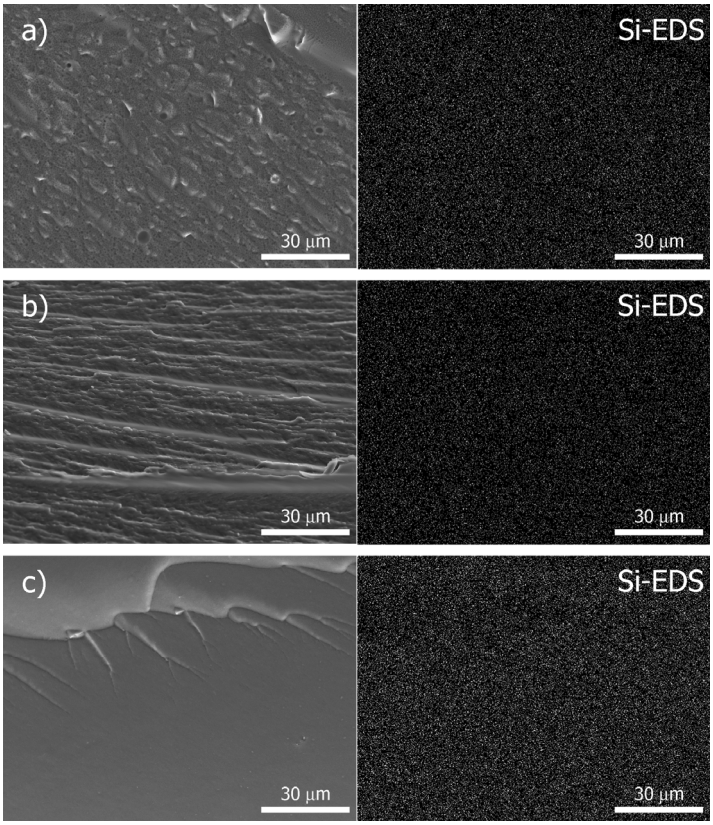

Figure 3.9. Micrographs of cryo-fractures at 1000x and their corresponding silicon microanalysis mapping: a) PHEA-10wt% SiO_2; b) PHEA-20wt% SiO_2; c) PHEA-30wt% SiO_2.

3.1.3. Porous distribution of silica

As seen in Figure 3.10, the density of the nanocomposites varies linearly with their silica content (expressed as mass fraction) [107]. The extrapolated value for pure silica obtained from that trend is 2.196 g/cm^3, which coincides with the value for the pure silica glass obtained after a heat treatment at 900ºC [16].

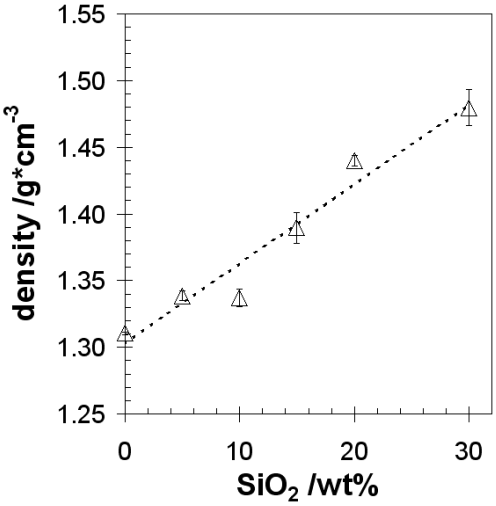

Figure 3.10. Dependence of the density (Δ) of the hybrid materials on the silica content. The dotted line represents a linear regression of the measurements. Error bars represent standard deviations.

The porous structure of silica is bimodal (Figure 3.11): a family of disordered assembly of smaller pores in the few-nanometer range (around 3 nm [103]) within the elementary silica nanoparticles due to the combined effect of, on one hand, synthesis conditions which yield open porous silica structures because of the formation of linear species (low condensation degrees) [16,18,20,102] and, on the other hand, the liquids acting as a template during the sol-gel reaction [108,109], even with non-surfactant templating liquids [99,103,104]. There is another family of pores consisting in the larger spaces (tens of nanometers) left between the aggregates of those smaller elementary particles that develop as the phase separation and coalescence of silica proceed to

form a continuous network [19,29]. Density data point out that all these pores have been occupied by the organic polymer matrix' chains: the apparent specific volumes of both mixed phases coincide with the specific volumes of both pure phases (in the case of the silica network, that of its sintered amorphous glass [16]), thus indicating a most efficient packing of the phases, with no interstitial vacancies. This highly efficient filling of the pores must be related to the fact that silica polymerization is a faster process that the organic polymerization [59].

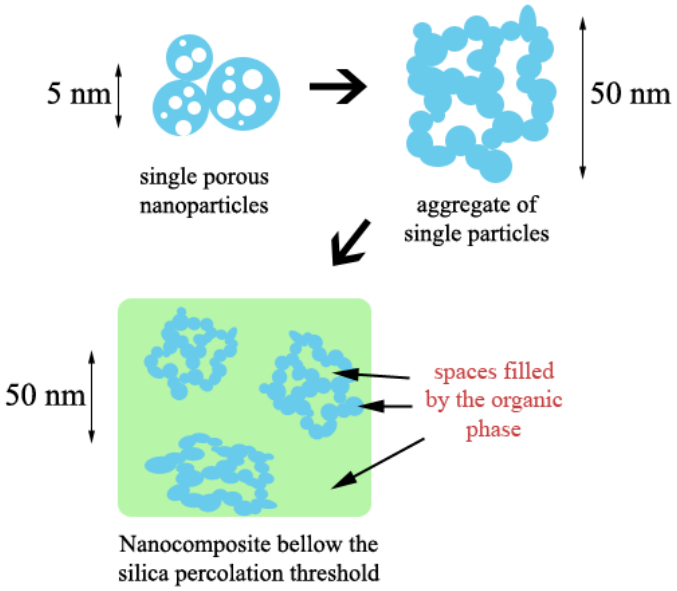

Figure 3.11. Sketch of the silica built-up on nanocomposites. Three different types of spaces are filled by the organic phase: those within single particles (with sizes *circa* few nanometers), in the spaces between single particles aggregates (tens of nanometers, Figure 3.1) and finally the spaces left between aggregates (unperturbed bulk polymer).

3.2. Chemical and/or physical bonds between organic and inorganic phases?

The FTIR spectra for three nanocomposites (10, 20 and 30 wt%) and for pure PHEA are represented in Figure 3.12 [107]. With increasing silica contents of the nanocomposites there is an intensity increase of some characteristic peaks of the silica phase such as the *Si-O-Si* stretching at 1085, 1024 and 800 cm^{-1} [110,111]. At the same time, the *OH* stretching at 3405 cm^{-1}, the CH_x asymmetric and symmetric stretching peaks at 2962 and 2888 cm^{-1}, respectively, and the *C=O* stretching peak at 1724 cm^{-1} tend to disappear with increasing silica content.

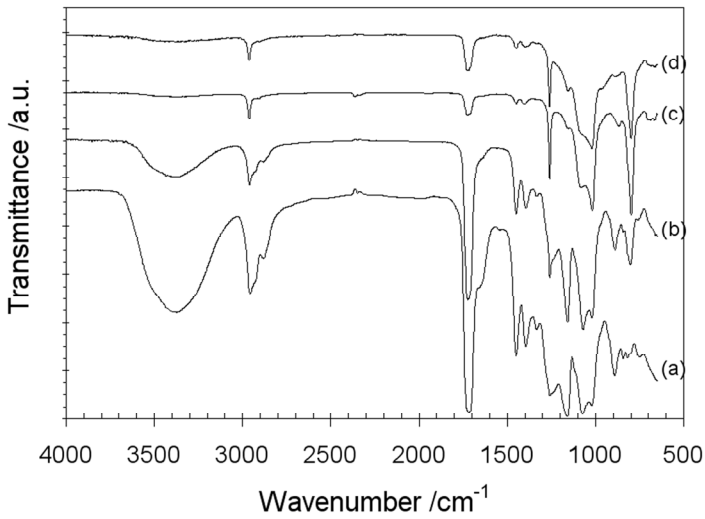

Figure 3.12. FTIR spectra for hybrid materials: (a) pure PHEA; (b) PHEA-10% SiO_2; (c) PHEA-20% SiO_2; (d) PHEA-30% SiO_2. The spectra are shifted in the ordinate axis for sake of clarity.

The stretching vibration of silanols (*Si-OH*) takes place at 3588 and 964 cm^{-1} [44]. The higher energetic peak overlaps with the one corresponding to the stretching vibration of PHEA hydroxyls and therefore it is not conclusive to ascertain the existence of silanols.

However, there is a small peak that arises with the increase of the silica percentage at 970 cm^{-1}, which is assigned to the occurrence of silanols. But more important than the easy to identify silanol peaks in the FTIR spectra is the fact that silica obtained by sol-gel reactions at mild temperatures does not possess the same condensation degree as those obtained from melt [18,19], especially with the acid catalyzed conditions used in this work, which implies the existence of silanol and ethoxy groups. Thus, even though silanol peaks are hidden by other peaks appearing at the same wavenumbers, it is expected they exist and, indeed, it is confirmed by other techniques (like DMA and TGA, as will be shown below).

The FTIR peaks that could reveal heterogeneous condensation reactions between the HEA monomers and the silanols, such as the characteristic peak for the Si-O-C bond, should take place at 1120-1080 and 836 cm^{-1} [110,111]; they overlap the absorption interval of the Si-O-Si bond (at 1085, 1024 and 800 cm^{-1} [110,111]) and are thus not distinguishable in the reported spectra (Figure 3.12). Therefore no definitive conclusions can be obtained from the FTIR data as regards the question whether heterogeneous condensation between the organic and the inorganic monomers occurs or not, and thus whether stable chemical bonds between the PHEA and the silica phases exist. On the one hand, the residue weights of silica at 700ºC (Table 3.1) correspond accurately to the TEOS amounts put into the reacting mixture. On the other hand, the FTIR spectra (Figure 3.12) show a marked disappearance of the broad OH absorption as the silica content is increased, but this might be an effect of the increasing stiffness of the samples, which results in a less efficient contact of the sample with the apparatus in the ATR mode. It is thus not directly interpretable as a loss of the PHEA's hydroxyl groups at the expense of interphase condensations. That these OH groups have not disappeared and are, to a large extent, still present in the organic phase is demonstrated by the water sorption data (Figure 3.18). The fall of the equilibrium water sorption after sample composition 15wt% must be attributed not to a loss of active OH groups but to the constraint on the polymer network expansion imposed by the continuous silica network. This constraint is independently revealed by the acetone sorption data (Figure 3.18). In fact, the equilibrium water sorption of the 30wt% silica sample closely

coincides with the equilibrium water content of PHEA in a pure water vapour atmosphere, a situation which corresponds to the maximum sorption capacity of the polymer before the network starts to swell significantly [112-114]. It is thus a swelling constraint, and not the absence of the OH groups, what explains the fall in the sorption capacity. The safe conclusion is that polymer-silica condensation reactions, if they occur at all, involve a non-significant fraction of the materials (the same conclusion was put forward in [29], although the opposite view has also been defended [30]).

One can conclude that physical interactions between organic and inorganic phases lead to a strong adhesion (wettability) between the hydrophilic silica and PHEA, since otherwise, the glass transition temperature would not increase with the silica addition [48,50,115,116].

3.3. Influence of the silica amount on the nanocomposite properties

3.3.1. Mechanical properties

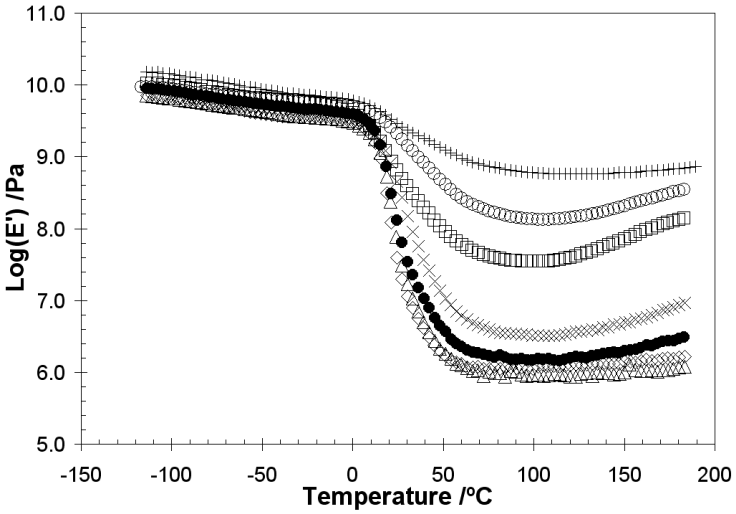

Figure 3.13. Temperature dependence of the storage modulus of dry nanocomposites with different silica contents: (◇) pure PHEA; (△) PHEA-5% SiO_2; (●) PHEA-10% SiO_2; (×) PHEA-15% SiO_2; (□) PHEA-20% SiO_2; (○) PHEA-25% SiO_2; (+) PHEA-30% SiO_2.

Figure 3.13 shows the curves for the temperature dependence of the dynamic-mechanical storage modulus (*E'*) of dry samples [107]. Pure PHEA exhibits a well defined plateau above the glass transition due to transesterification reactions which are unavoidable during its normal free radical polymerization, building a network with chemical bonds between lateral side groups even with the absence of crosslinking agents [13]. *E'* increase takes place both at the glassy and rubbery states, but it is in the latter state where is more dramatic: even though the *E'* increase value is higher at the glassy state (~1 GPa), it is more relevant above the glass transition temperature, up to almost three orders of magnitude for the highest silica amounts (it means almost a suppression of the glass transition as regards the *E'* fall). The

rubbery plateau in the hybrid materials has a higher storage modulus the greater the silica content. The rubbery modulus of some nanocomposite samples (especially the 15%, 20% and 25% samples) showed a marked increasing trend for the highest temperatures. The values of the elastic modulus of the swollen samples measured at 25ºC are shown in Figure 3.14. If the elastic moduli are fitted by linear regressions below and above the silica percolation, their intercept is almost the same regardless swollen or dried modulus data are used (Figure 3.14).

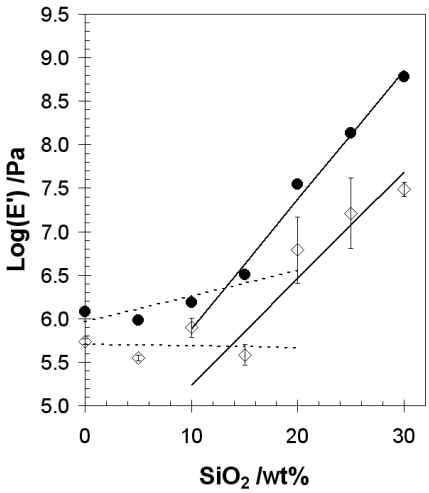

Figure 3.14. Storage modulus corresponding to the rubbery state of dry hybrid materials at 100ºC and 1 Hz (●), and for swollen samples (◇) at 25ºC and 1 Hz. Lines are linear regressions for data below (dotted) and above (solid) the silica percolation. Error bars represent standard deviations.

The reinforcement of a PHEA matrix by a nanosized uniformly disperse phase of silica (Figure 3.8) obtained by simultaneous sol-gel polymerization provides an effective method to improve the mechanical properties of the hydrogel: the storage modulus in the swollen state at 1 Hz increases from a value of around 0.54 MPa for PHEA to a value of around 30.7 MPa for the 30%wt nanocomposite (Figure 3.14), a 57-fold increase for a material which is still a hydrogel! These materials

retain many of the good properties of the matrix polymer: they are hydrogels (the 30%wt nanocomposite still absorbs 38% of its weight of water, Figure 3.18) and they are transparent (average silica sizes in the order of tens of nanometers, Figure 3.2).

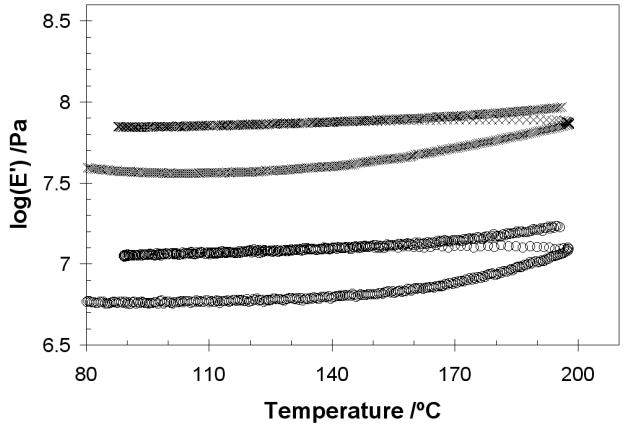

Figure 3.15. Evolution of the storage modulus (E') for dry samples at 1 Hz and a heating rate of 2ºC/min with a cycling temperature program of a first heating until 200ºC, an immediate cooling until 90ºC, and a final reheating for the 15% (○) and 20% (×) silica content hybrid materials.

The temperature increase of the storage modulus taking place after the glass transition was in some nanocomposite samples larger than what rubber elasticity effects could account for, and thus the hypothesis that some additional condensation reactions in the silica phase could be taking place enhanced by the mechanical stimulus at these high temperatures above T_g is advanced. To check this, a thermal cycling experiment was performed: samples were run to a temperature $T^*>T_g$, then cooled and then reheated until a temperature $T>T^*$. The results in Figure 3.15 show that indeed the modulus increment reached at a temperature T^* is permanent, and that the modulus continues increasing if that temperature is surpassed. This seems in accord with the hypothesis that the silica phase contains non-reacted silanol groups which can condense further when the mobility of the silica and PHEA phases becomes high enough [29,117]. It is also in

agreement with the mechanism of silica build-up proposed by Brinker et al [18], by which silica domains obtained by sol-gel process never reach a condensation state equal to that of a full-condensed silica, thus allowing additional condensations to take place if suitable conditions are met (in our case, the un-freezing of the network's state at temperatures well above T_g). A FTIR assay was performed after the thermal treatment, but no significant differences were found. It means that only few silanols are able to undergo further condensation reactions, but enough to increase the material's stiffness.

The polymerising conditions where hybrid samples were produced (i.e. acidic conditions and low stoichiometric water amount) make hydrolysis reaction definitively faster than condensation. Indeed, the procedure of sample preparation involves a first step by which TEOS hydrolysis improves its miscibility with water at room temperature [27,28] before the mixture with the organic dissolution (see *2.1.1. PHEA-silica nanocomposites*). Sol-gel condensation reaction may be thus taking place simultaneously with the organic phase synthesis. Besides, Hajji et al concluded that a lower glass transition temperature yields higher condensed silica species because of the viscosity decrease of the organic phase [29], issue which points out that both silica condensation and PHEMA polymerization takes place at the same time. Although this situation does not strictly apply to our system since synthesis always takes place at temperatures higher than T_g (Table 3.2), the viscosity increase due to PHEA polymerization (liquid to solid) joint to the barrier effect of the organic phase (even with a such phase interpenetration) may make condensation reactions further delayed. Taking into account this matter and that a condensation state similar to that of full-condensed silica is not reached without thermal treatments at high temperatures, these thermal treatments above T_g and below the onset of the thermal degradation (T_{10}, see Table 3.1) let condensation reactions continue (irreversible processes like that shown in Figure 3.15).

3.3.2. Real silica contents and thermal stability

Thermal degradation of polymers is generally a complex multistage process which involves several reactions taking place simultaneously. It is well established the different thermal stability behaviour which polyacrylates and polymethacrylates show, even thought the large similarity on their chemical structures: whereas polymethacrylates decomposes releasing large amounts of monomeric units, polyacrylates undergo main-chain scissions and side-chain reactions [118]. Main-chain scissions products lump monomers, dimmers, trimers, saturated esters and the corresponding acetates and methacrylates, whereas non-radical side-chain reactions yield olefins and alcohols.

Silica /wt%	**T_{10}[ii] /ºC**	**T_{50}[ii] /ºC**	**T_m[iii] /ºC**	**T_{hf}[iv] /ºC**	**Residue at 700ºC /wt%**
0	374.2	447.1	452.3	477.8	0.10
5	369.3	448.2	454.6	464.4	3.21
10	369.7	447.8	458.1	468.6	7.17
15	362.6	448.8	462.3	464.8	11.67
20	355.0	438.0	426.7	437.8	17.84
25	354.9	424.7	422.6	436.0	29.06
30	355.0	433.5	420.0	433.4	30.87

Table 3.1. Thermal characterization of the hybrid materials and final residues.

[ii] T_{10} and T_{50}: temperature corresponding to 10 and 50 wt% loss, respectively.
[iii] T_m: temperature of maximum rate of weight loss.
[iv] T_{hf}: temperature corresponding to the maximum of the endothermic peak for the main degradation mechanism.

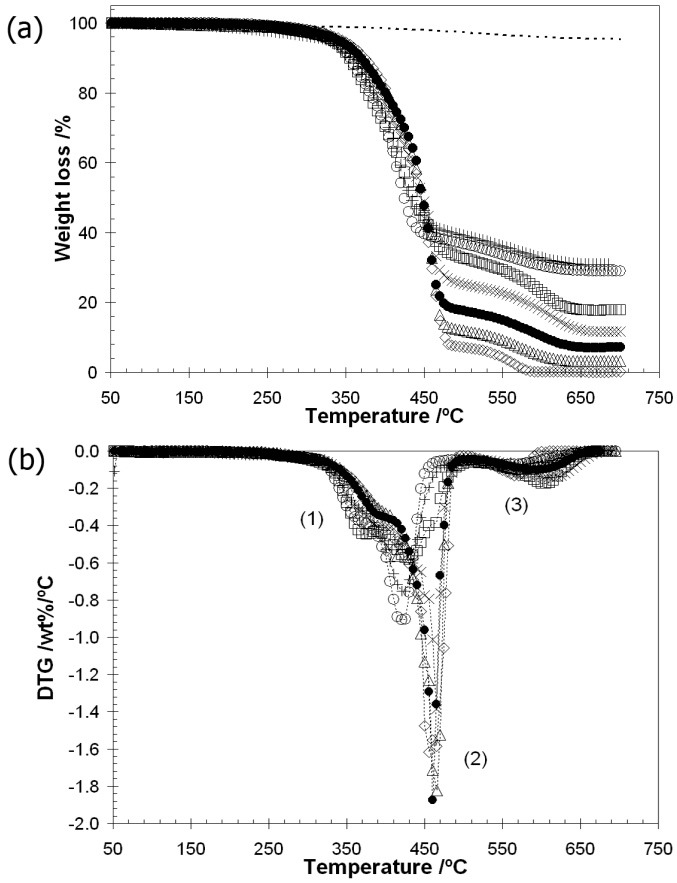

Figure 3.16. Weight loss curves (a) and their temperature derivative (DTG) (b) for the hybrid materials versus temperature: (◇) pure PHEA; (△) PHEA-5% SiO_2; (●) PHEA-10% SiO_2; (×) PHEA-15% SiO_2; (□) PHEA-20% SiO_2; (○) PHEA-25% SiO_2; (+) PHEA-30% SiO_2; (dotted line) pure SiO_2 as obtained from TEOS in the sol-gel process. The degradation steps are indicated in (b).

The residue weights of silica at 700ºC correspond accurately to the TEOS amounts theoretically computed by Eq. 1.9 [107]. The residue of pure silica at 700ºC is a 95.47% of its starting weight. This small weight decay can be the product of two thermal degradation mechanisms [16]: at lower temperatures combustion of non hydrolyzed alkoxide groups takes place; and for higher temperatures, condensation reactions continue releasing water molecules, producing

a further weight loss. The residues after pyrolysis of the nanocomposites showed that the silica rests kept the original shape of the sample, but shrunk (the higher the silica content the lower the shrinkage). All of them exhibited a smooth surface with occasional cracks, as can be seen in Figure 3.17.

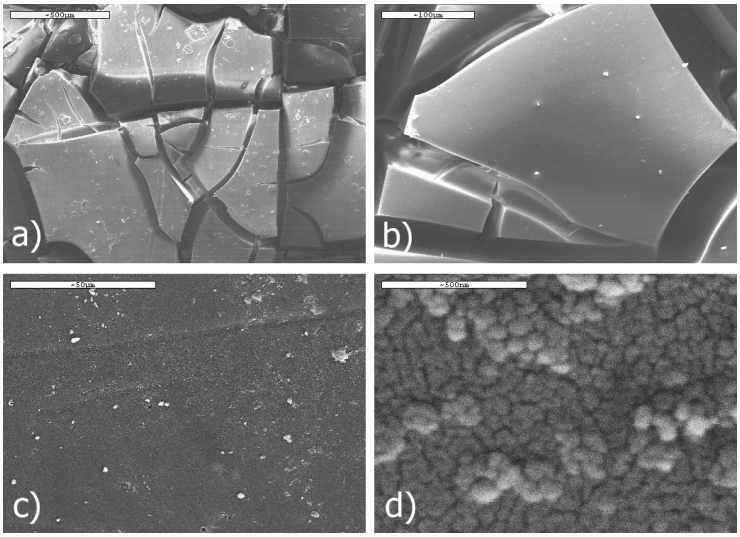

Figure 3.17. SEM images of silica residues after pyrolysis of a nanocomposite with 30wt% silica at different magnifications: a) 75x; b) 350x; c) 1000x; d) 100000x.

The sensible loss of thermal stability of the hybrid materials (defined as the temperature where a 10wt% of the initial mass is lost, Table 3.1) may be a consequence of the just mentioned additional reactions taking place at temperatures above T_g in the nanocomposite samples: active silanols of the silica network or water produced in those condensations may have an accelerating effect on the organic polymer chain scission [119]. One cannot exclude other factors (alternative or conjoint) in the explanation of this shift in the onset of thermodegradation, such as the different morphology of the polymer phase (a bulky phase in the case of the homopolymer, a finely dispersed one in the nanocomposites), leading to the same effect.

3.3.3. Continuity of silica phase

The water and acetone sorption capacity of the samples, referred to the mass of the organic polymer (PHEA) in the sample, is shown on Figure 3.18 [107]. The equilibrium water uptake of the nanocomposites as a function of silica content is first increasing and then decreasing: for silica contents lower than 15wt% the nanocomposites absorb more water than does pure PHEA, their specific sorption capacity falling afterwards under that of the pure matrix polymer. On the contrary, acetone uptake shows a sharp initial decrease at the lowest silica content (5%wt), and then smoothly decreases at higher silica contents.

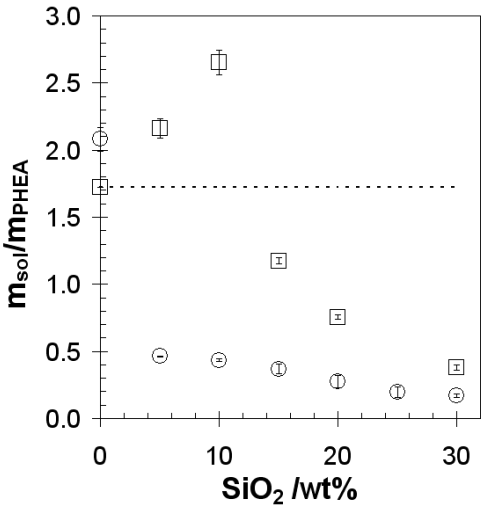

Figure 3.18. Dependence of the equilibrium water content (□) and the equilibrium acetone uptake (○) of the hybrid materials on the silica content. Uptake values are referred to the polymer mass. The horizontal line marks the equilibrium water content in immersion for pure PHEA. Error bars represent standard deviations.

There are further indications that the silica phase is not a continuous network throughout the sample below a threshold silica content: the storage modulus in the rubbery region, both in the dry and swollen states (Figure 3.14), shows a characteristic transition

around a 15wt% content of silica in the sample; furthermore, the maximum of water sorption of the samples occurs around a 10wt% content of silica (Figure 3.18). This suggests that below a value between 10 and 15wt% of silica content the inorganic network is not continuous throughout the sample, and that it constitutes a co-continuous phase only above that value. The increasing trend of water sorption up to 10wt% can be explained on the basis that for non-continuous disconnected silica domains, the number of non-condensed silanol groups on the surface of those domains is significant [117] (large surface to volume ratio), thus increasing the hydrophilicity of the hybrid material on a unit mass basis to a value above that of the PHEA matrix; when the silica network percolates and finally becomes continuous throughout and densely packed for higher silica percentages, these surface OH groups are no longer present or become insignificant (small surface to volume ratio). The water sorption then rapidly falls under the value of PHEA as a consequence of the swelling constraint imposed by the rigid silica skeleton. This is further confirmed by the outlook of the silica residues obtained after complete pyrolysis of the nanocomposite samples in the TGA experiments (Figure 3.17): the residues of samples with lower silica content were very brittle and hardly manageable (even after the contraction and sintering which silica experiences at high temperatures [16,20]), whereas the residues of samples with more than 10wt% silica exhibited good consistency. This last finding is another indication of the finely interpenetrated and co-continuous morphology of both phases in the nanocomposites.

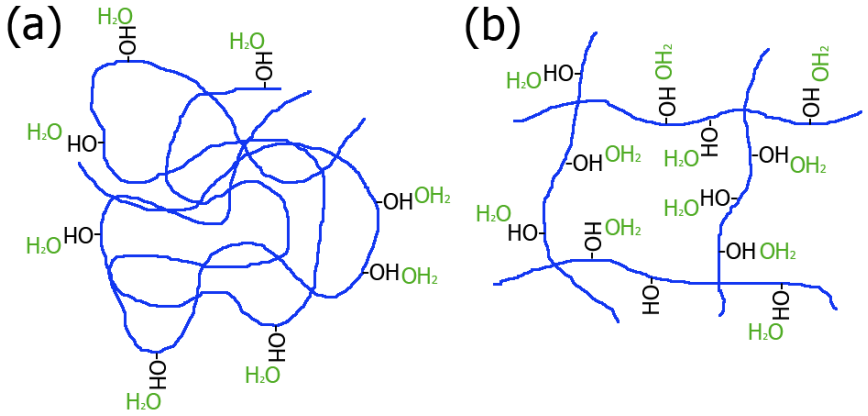

Figure 3.19. Sketch of the swelling behaviour of pure PHEA: (a) the network is equilibrated in water vapour; (b) equilibration after being immersed in water.

The equilibrium water content data can be explained taking into account the continuity of silica in nanocomposites. But first, in order to do so, it is worth explaining how pure PHEA behaves when it is either exposed to controlled humidities or immersed in water, and then try to extrapolate this behaviour to the more complex experimental data of nanocomposites, where water uptake does not only depend on the PHEA phase, but also on silica.

When pure PHEA is exposed to water vapour, only around one third of the whole hydroxyls are ready to form hydrogen bonds with water, since the others are screened because they face each other forming micelles [114], similar to the hydrophobic interaction which takes place at hydrophilic/hydrophobic copolymers when immersed into a solvent [4]. However, when PHEA is immersed in water, the polymer network expands and the hydroxyl micelles disentangle. The consequence is that almost all hydroxyls are available to bind with water molecules and thus the water uptake significantly increases (Figure 3.20b).

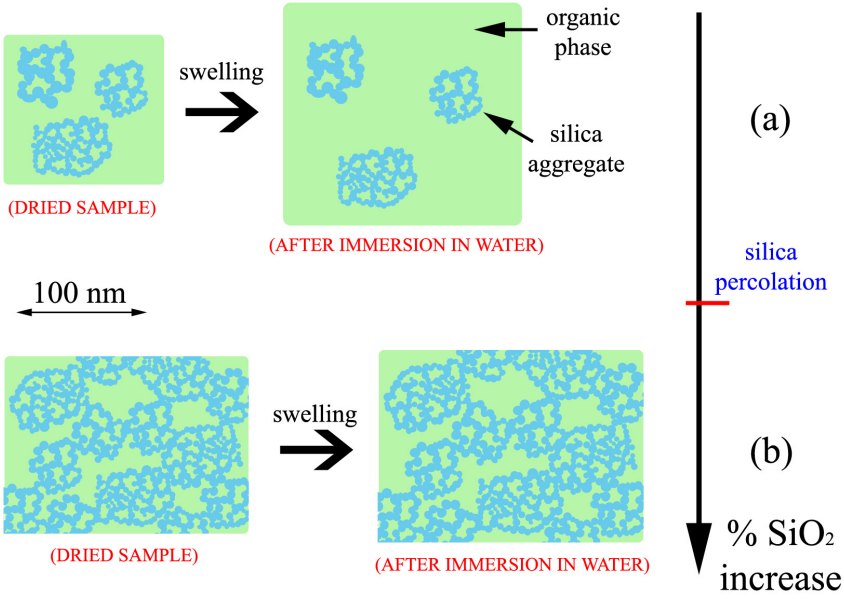

Figure 3.20. Swelling of nanocomposites after water immersion: (a) before and (b) after silica percolation. The difference of the swelling capability depends on the PHEA hindrance (because of silica) to expand.

The water uptake capability of both phases, PHEA and silica, differs from each other: even though both are hydrophilic, the polymeric hydrogel PHEA absorbs larger amounts of water. However, an explanation of the hybrids' behaviour as regards the water sorption must take into account the water binding sites (hydroxyls) of both phases. On one hand, the PHEA hydroxyl density monotonically decreases as the silica phase increases since there are less organic matrix; on the contrary, the evolution of silica hydroxyls is more complex, with a maximum probably around 10wt%, due to a factor involving the silica surface area, where silanols (≡Si-OH) which contribute to the water uptake are located. This function maximum may arise from two opposite trends: at low SiO_2 contents, the specific hydroxyl amount introduced by silica is larger than that corresponding to PHEA and as a consequence the equilibrium water content first increases (Figure 3.18); however, assuming an spherical silica shape,

the specific area decreases as its radius increases and thus the silanol density finally decreases. Furthermore, through silica percolation, two phenomena take place: first, the PHEA hindrance to expand and thus the disentanglement of its micelles does not occur; and second, the aforementioned less specific silica area per unit mass.

The striking water sorption results for the smallest silica percentages (5 and 10wt%, referred to the polymer mass) which are even higher than that corresponding to pure PHEA (Figure 3.18), accounts for the higher specific *–OH* density for such small silica contents. For these nanocomposites, the inorganic structure is not continuous, forming small unconnected aggregates with additional hydroxyl groups (silanols) on their surfaces. The PHEA expansion during the water immersion in them is thus not hindered so much by the dispersed silica, and therefore hydroxyl micelles can be disentangled as do in pure PHEA (Figure 3.20a). On the contrary, for hybrid materials with high inorganic percentages (from 15 to 30wt%), silica percolates and the expansion of the organic phase is mostly hindered (Figure 3.20b). Therefore PHEA hydroxyls forming clusters cannot be disentangled and, additionally to the silanol decrease because of a smaller surface to volume ratio, the equilibrium water content finally drops. The absorbed water then approaches to the value corresponding to the water uptake at high relative humidities for pure PHEA [114], pointing out that the polymer state in nanocomposites concerning water uptake is similar to the one exhibited by neat PHEA in the presence of water vapour.

Additional information about the structure of the silica phase can be obtained from nanoindentation experiments. The result of one of these experiments is shown in Figure 1.3, where the force is represented against the difference between the displacement of the sample in the vertical axis, z, and the cantilever deflection, d. The variable z-d is the relative displacement between the tip and the polymer surface (h). In an elastic body the stiffness (S) can be related to the elastic modulus (Eq. 1.14) and the hardness [76,81,120,122, 123,136], but for assessing the co-continuity of both phases an analysis of the stiffness itself throughout the nanocomposite surface suffices (to compute the sample Young modulus through a reduced

modulus (E_r) is necessary to know the Poisson ratio of the sample). Therefore, we will be only able to map relative material property differences for our set of nanocomposites.

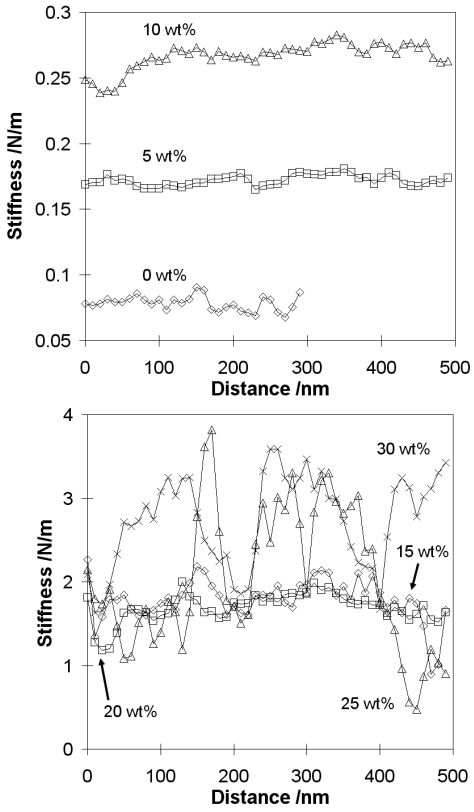

Figure 3.21. Stiffness measured by AFM indentation experiments in a series of aligned points separated 10 nm for different silica contents a): (◊) PHEA, (□) 5wt%, (Δ) 10wt% b) (◊) 15wt%, (□) 20wt%, (Δ) 25wt%, (x) 30wt%.

Appendix 2 collets the stiffness measurements for all the samples (one point means an individual nanoindentation assay, Figure 1.3) as a function of the position along a straight line, on the PHEA homopolymer and the hybrid materials with different silica contents. Though for time-independent materials the load-depth curve in the

initial unloading stage is used to determine the stiffness of the material, this approach is not recommended for viscoelastic materials, in which the loading stage has been shown to be more accurate [81].

There is a great difference in the elastic modulus between PHEA, which is a rubber at room temperature [6], and the inorganic silica phase. The results of the nanoindentation experiments (Figure 3.21) are in good agreement with the mechanical properties of these nanocomposites as obtained by standard macroscopic methods along this work (Figure 3.14) and in previous studies [73,124]. The average stiffness as calculated from Eq. 1.11 increases as the amount of silica in the sample does, as expected.

Nanoindentation experiments explore the viscoelastic behaviour up to ~30 nm depth from the surface. The stiffness value obtained in a nanoindentation experiment not only depends on the characteristics of the surface point where the tip is penetrating but also on the structural characteristics of the surrounding material. For low silica content, up to 15wt%, tapping mode phase images show dispersed silica domains with sizes up to 100nm or even larger in the sample containing 5wt% silica (Figure 3.8a to c), that must be due to regions in which the silica nano-particles concentration at the surface is higher than average. Nevertheless, in spite of the great difference between the stiffness of silica and PHEA, the nano-indentation experiments show a quite uniform behaviour (Figure 3.21), similar to that found in unreinforced PHEA. This can attributed to the fact that silica particles are not connected to each other and the stiffness, that measures a global response in a region some tens of nanometres around the AFM tip, is similar in the regions that appear dark or bright in the tapping mode picture. The increase of the stiffness as the silica content increases is moderate for silica contents lower than 10wt% (from approximately 0.08 N/m for PHEA homopolymer to 0.27 N/m for the sample containing 10wt% of silica). However, there is a qualitative change in stiffness when the silica fraction is 15wt% or higher, what results in stiffness of approximately 2 N/m, and at the same time the value of the stiffness in different points of the surface present a higher heterogeneity as can be seen in Figure 3.21. For samples of higher silica content the stiffness profile show sharp peaks with minima

around the same values than those in sample with 15wt% silica and maxima rising more than 3.5 N/m. This behaviour suggests a transition in the structure of the silica phase: for silica contents up to 15wt% silica nano-aggregates are isolated in the organic PHEA matrix. From this content on, the silica phase percolates and becomes interconnected, and plays the role of an inorganic scaffold that improves the mechanical properties of the system. When the tip touches a cluster of the co-continuous silica network, nanoindentation experiments show a much stiffer material than when the contact point between material and tip has a larger concentration of polymeric material (see Figure 3.22). For those samples with the highest silica contents (25 and 30wt%) the probability that the initial contact point between tip and sample takes place on a silica particle is higher and this is the reason why there are much more points with stiffness in the interval between 2.5-3.5 N/m. The picture provided by nanoindentation experiments in this case correlates better with that shown by phase angle lag in tapping mode AFM (see Figure 3.8).

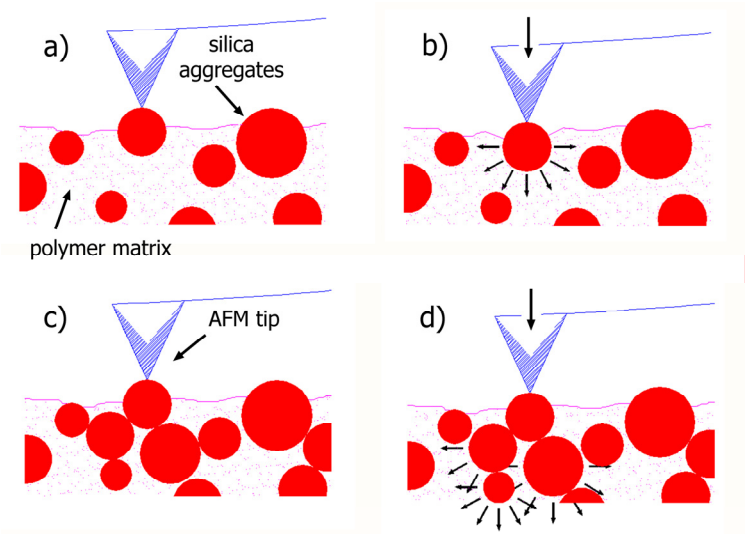

Figure 3.22. Sketch of the interaction between AFM tip and a nanocomposite surface: a-b) low silica contents (dispersed aggregates); c-d) high silica contents. For sake of clarity silica is merely represented as spheres.

Similar results were obtained by Geng et al when evaluating the nanoindentation behaviour of nanometre-thick polymeric films deposited onto silicon wafers [78]. Compared with the elastic properties of polymers, silicon can be considered as rigid. Their results pointed out that depending on the ratio between the penetration and polymer thickness, the substrate influences (or not) the computed reduced moduli: when the indentation depth is higher than 10% of the ultrathin film thickness, the reduced moduli increases because of the substrate. The underlying cause for this behaviour is similar to that hypothesized above for the nanoindentation assessments on PHEA-silica nanocomposites: the role which the surrounding material plays in the elastic properties one evaluates with indentation.

3.3.4. Confinement of PHEA owing to the coexistence with silica

Several works deal with the confinement effects on molecular relaxation dynamics of polymers, either deposited onto substrates [125,126] with nanometer thicknesses, or immobilized on porous materials [50,127]. Poly(methyl methacrylate) (PMMA) is a polymer widely used for lots of applications which belongs to the acrylic polymer family (for instance bone cements are basically made up by PMMA). Several studies dealing with the confinement of PMMA macromolecules on porous substrates yield to either a slowdown of the cooperative main (α) relaxation joint with a speed-up of the sub-glassy secondary (β) relaxation [50], or *vice versa* [127]. Kaloregas et al claimed that it is established hydrogen bonds between the slightly acidic silica surface with the relative basic carbonyl group belonging to the ester group of the pendant chain [50] on silica-filled PMMA. Hydrogen bonding introduces extra free volume which gives rise to fluctuations on the local density with an increase (or decrease) of side chain molecular mobility. This accounts for the shift of the sub-glassy secondary relaxation phenomenon in immobilized PMMA molecules, probably similar to what is happening in PHEA-derived sol-gel nanocomposites between phases. On the other side, the issue whether it exists an immobilized polymer fraction which do not contribute to the glass transition relaxation on PHEA-based nanocomposites (the existence of

the so-called interphase) which was previously introduced, will be extensively discussed later on. Whatever the conclusion regarding this concern, it is claimed that the side chain relaxation occurs regardless the polymer chains are hindered or not [82], since sub-glassy relaxation modes should be understood as a sum of contributions of the individual relaxing side-chain groups. However, it is advanced the slowdown of cooperative rearrangements taking place at the glass transition owing to hydrogen bonds, electrostatic and dipole-dipole interactions established between phases, as well as the role of the silica aggregates as spatial barriers.

Given the biphasic nanocomposite structure which is presented in preceding sections (mainly in *3.1.3. Porous distribution of silica*) and generally sketched by Figure 3.11, there must be always an entrapped (interpenetrated) organic phase in the nanocomposites, regardless the silica content, due to the filling of the smallest silica pores (few nanometres) present on single particles by the organic polymer. However, this constrained phase is not quantitatively significant for the smallest silica contents (5 and 10wt%): most of the organic phase fills the rest of the available free spaces (i.e. both inside and between single particle aggregates) and behaves as neat PHEA does. On the contrary, from this content on, the constraint on PHEA begins to be significant owing to the increase of silica particles and aggregates (higher silica contents). Likewise, after silica percolation, single particle aggregates are closer and perhaps the size of the spaces left inside them diminishes. Therefore, PHEA molecules which fill those latter holes may contribute to the constraint organic phase in nanocomposites. Finally, at the highest silica percentages (25 and 30wt%), there are lots of hindered PHEA chains sections, pointing to a high degree of interpenetration between phases; however, there is still others unperturbed.

Figure 3.23 shows the dynamic-mechanical loss tangent thermograms of pure PHEA and nanocomposites [107]. The pure PHEA plot shows two maxima: one corresponding to the main, or α, mechanical relaxation at around 26ºC, and another one at lower temperatures, associated to a complex side-chain relaxation with small amounts of water [3,11]. Both of them show up again in the

nanocomposites. However, as the silica content increases, the intensity of the α relaxation of the polymer matrix significantly decreases and its shape broadens and shifts towards higher temperatures, becoming more asymmetric, in agreement with the behaviour exhibited by other nanocomposite systems [50,116,128]. On the contrary, the temperature at which the relaxation related to the lateral groups (β, β_{sw}) takes place seems to decrease with increased silica contents (Figure 3.24).

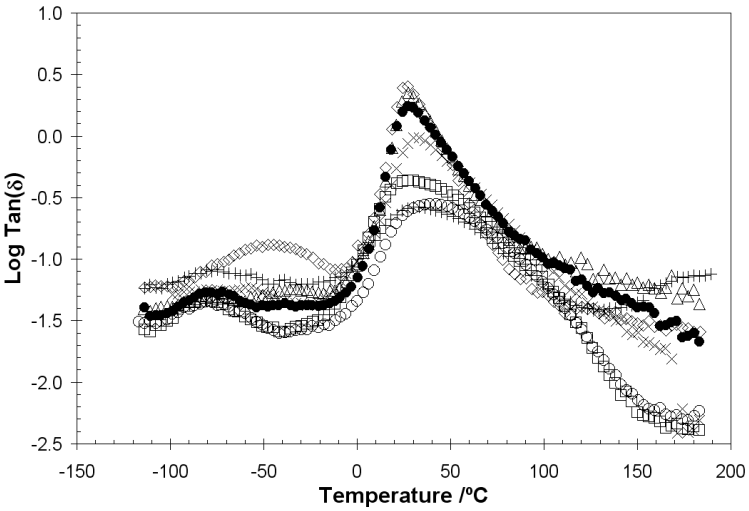

Figure 3.23. Temperature dependence of the loss tangent of dry nanocomposites with different silica contents: (◇) pure PHEA; (△) PHEA-5% SiO_2; (●) PHEA-10% SiO_2; (×) PHEA-15% SiO_2; (□) PHEA-20% SiO_2; (○) PHEA-25% SiO_2; (+) PHEA-30% SiO_2.

The interpenetration and co-continuity of both phases (with silica contents higher than 15wt%) lead to a very constrained mobility of the polymer chains in the spaces left by the inorganic phase. (It is worth remembering at this point that silica polymerises faster than PHEA; otherwise, a macro-phase separation takes place and transparency is lost [59]). This is in fact reflected in the dynamic-mechanical loss tangent (Figure 3.23), whose dissipation maximum significantly decreases in intensity as the silica content of the sample increases. Other results on the same hybrid system also hinted to the

existence of a more constrained PHEA phase within the nanocomposites whose dissipation maximum corresponding to the main mechanical relaxation takes place at lower frequencies in comparison with the less constrained PHEA rich-domains, which behaves as the pure homopolymer [73].

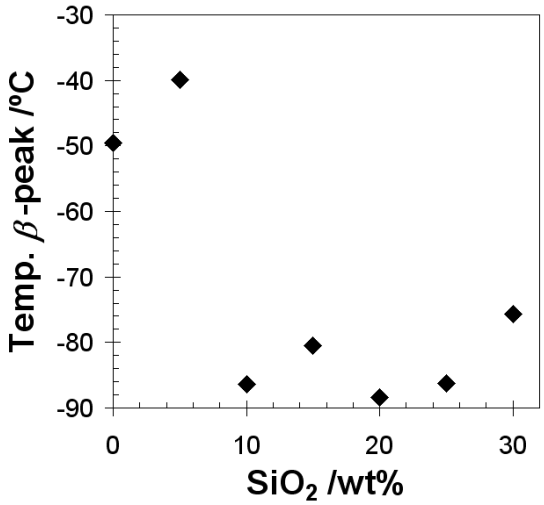

Figure 3.24. Silica dependence of the temperature of the loss tangent maximum appearing at the β relaxation zone.

The presence of the silica phase has also an influence on the secondary dynamic-mechanical relaxation of the polymer. The side chain relaxation of PHEA takes place at different temperatures depending on the amount of residual water remaining in the polymeric network [11,129]. Water-free PHEA has a simple secondary β-dispersion around -90ºC due to the motion of the side chain including the COO groups. When there is water in the polymer this relaxation transforms into a more complex secondary relaxation (called "diluent" relaxation, β_{sw}) taking place at higher energies (around -60ºC), due to the association of water molecules and neighbouring hydroxyls of the PHEA chains [11]. In the nanocomposites with the highest silica contents PHEA molecules are more constrained than in the homopolymer; the formation of those associations of neighbouring

lateral groups through the water hydrogen bonding becomes more hindered, and thus the secondary relaxation has a more pure β-character (not involving water molecules) and it correspondingly takes place at lower temperatures (Figure 3.24) [107].

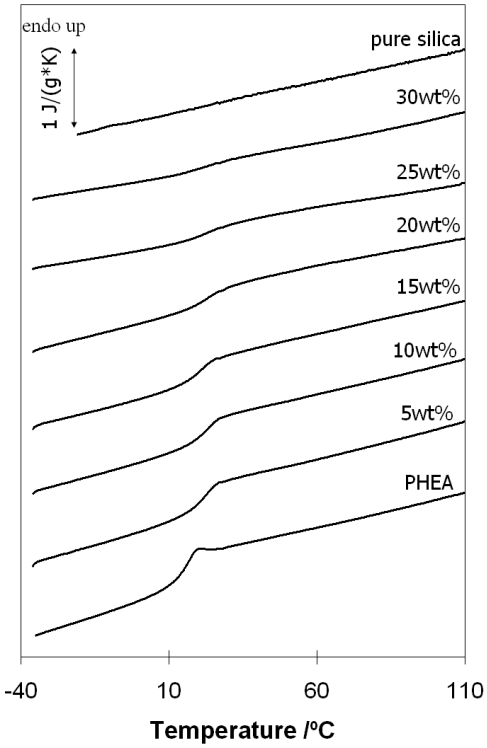

Figure 3.25. Normalized heat flow on heating referred to the sample mass of the PHEA-silica hybrids with different silica contents. The silica percentage is indicated on each curve.

Besides, there are other studies which explain the fall of the sub-glassy relaxation temperature (T_β) based on the physical interactions (mainly hydrogen bonds, but also electrostatic and dipole-dipole interactions) established between the relative acidic silica surface (silanols) and the carbonyl of the side-chain groups [50,115,116]: these interactions yield an extra free volume on the bulky phase of silica-filled PMMA nanocomposites, which finally

increases the glass transition temperature but decreases T_β as a result of an enhancement of local mobility.

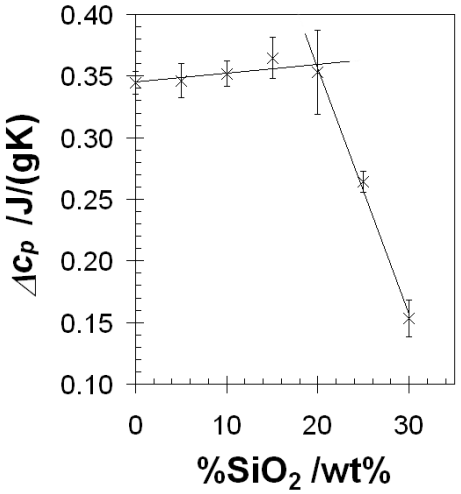

Figure 3.26. Specific heat capacity increment at T_g, Δc_p, per mass (×). Solid lines are linear regressions marking the tendency change. Vertical bars are error estimates obtained by propagation error laws.

Figure 3.25 shows the DSC curves of pure silica and PHEA-silica hybrids with different SiO_2 amounts ranging from 0 to 30wt%. A single glass transition process is observed on either homopolymer or hybrid scans, whereas pure silica exhibits a flat DSC profile, at least at this range of temperatures. The glass transition temperature T_g (Table 3.2) is almost independent of the silica content within the uncertainty of the measurement, but it is about six degrees higher than that of bulk PHEA. The presence of very small amounts of silica in the nanocomposite increases significantly the glass transition temperature of the polymer phase with respect to pure PHEA, what could be explained by the different conditions in the polymerization reaction of HEA: either bulk PHEA or forming the nanocomposite. In the later case the presence of TEOS and water and the low pH conditions could affect the topology of the PHEA network (mainly the average chain distance between crosslinks). It must be noted that even in absence of any cross-linking agent, the polymerization of HEA results in a polymer

network due to transesterification reactions of the side chain groups of the monomer [13]. Some influence of the reacting conditions on this side reaction cannot be excluded. Additionally, there is a broadening of the glass transition region as characterised by ΔT_g (Table 3.2). The specific heat capacity increment at T_g, $\Delta c_p\big|_{Tg}$ (measured per polymer gram), remains constant (if one takes into account the error estimates) or slightly increases around the value corresponding to neat PHEA for small silica percentages (5wt%) up to 20wt% SiO_2, from where it sharply decreases (Figure 3.26) [124].

Silica /wt%	$T_g\big\|_h$ **/ºC**	$\Delta c_p\big\|_{Tg}$ **/J/g ºC**	ΔT_g **/ºC**
0	18.9 ± 0.4	0.34 ± 0.01	6.4 ± 0.4
5	24.1 ± 0.5	0.35 ± 0.01	9.0 ± 0.3
10	23.2 ± 0.5	0.36 ± 0.01	10.4 ± 0.9
15	25.5 ± 0.5	0.36 ± 0.02	11.2 ± 0.4
20	26.0 ± 0.6	0.35 ± 0.02	11.4 ± 0.5
25	23.9 ± 0.4	0.27 ± 0.01	18.9 ± 10.2
30	23.7 ± 0.6	0.16 ± 0.01	17.6 ± 8.8

Table 3.2. Enthalpic glass transition temperatures (T_g), specific heat capacity increment at T_g (Δc_p) per polymer mass, and the width of the glass transition (ΔT_g) for each one of the PHEA-silica hybrids with different silica contents. The estimates of Δc_p errors are computed as the standard deviations corresponding to the reference heating scans of ageing assays (see *3.3.5. Physical ageing in nanocomposites*).

Literature is plenty of published works dealing with the glass transition temperature evolution in nanocomposites with either an increasing, decreasing or constant tend [48,52,82,130]. Furthermore, Bansal et al correlated the nanocomposite dynamic behaviour with that exhibited by supported thin polymer films [51]. The glass transition temperature evolution with silica (Table 3.2) must be the result of the balance of two different phenomena: polymer confinement and physical adsorption (i.e. physical interactions between phases). Polymer confinement yields less entanglement concentration and local density fluctuations which eventually result in increasing local free

volume and mobility (T_g falls) [39,50]. Nevertheless, as polymer confinement takes place, it is also established higher hydrogen bonds between the hydroxyls of PHEA and silica at the interface [39,52,115,131] and therefore the glass transition temperature does not decay at all: it first increases with small silica contents and afterwards, with larger SiO_2 amounts, it fluctuates around that temperature (~25ºC).

In order to assess whether small quantities of water and hydrochloric acid affect the polymer network, PHEA was synthesized at the presence of such amounts of HCl and H_2O to obtain nanocomposites with 30 and 60wt% silica, but without the addition of the silicon alkoxide TEOS. Results of DSC, water uptake and FTIR (data not shown) assert there are not significant differences between both homopolymers not regarding experimental errors.

The change of the behaviour shown by the specific heat capacity in DSC experiments for the highest silica concentrations may account for an increase of the interactions established between phases as a consequence of the increasing spatial molecular confinement of PHEA molecules which in turn, due to hydrogen bonding between hydroxyls of PHEA and silanols at the silica surfaces [39,52,115,131], disturbs the local and polymer chain dynamics. Besides, the broadening of the relaxation times distribution is supported, hitherto, by the widening of the glass transition assessed by DSC and DMA (it will be further discussed when physical aging assays are presented). After the percolation of the silica to form the inorganic network, the amount of polymer segments trapped between the inorganic phase and thus not participating in the cooperative conformational motions responsible for the glass transition, increases rapidly, since interpenetration yields enhanced electrostatic and dipole-dipole interactions between organic and inorganic phases [50]. It is worth noting that an extrapolation of the $\Delta c_p\big|_{Tg}$ results for samples with silica content above 20wt% would determine that in a sample containing less than 40wt% silica the polymer glass transition would be absent, i.e. all the polymer chains would be immobilized by the silica surfaces and no cooperative motions of the polymer segments would be allowed.

Wunderlich et al developed a formalism to quantify the amount of immobilized molecules surrounding crystallites in semicrystalline polymers based on heat capacity measurements (a current review can be found in ref [83]). The issue whether crystallites must melt first to allow the devitrification of the rigid amorphous fraction (*RAF*) around them or *vice versa* is still a hot topic [82]. Because of the melting of crystallites and the relaxation of *RAF* take place at almost the same range of temperatures, nanocomposites were chosen as ideal systems to study polymer confinement since inorganic reinforcements (for instance silica) do not undergo any transition at temperatures where polymers are thermally stable, and thus the organic-inorganic interactions remain the same [82]. Early works of Lipatov and Privalko [132,133] finally yielded a relationship to determine *RAF* in nanocomposites based on the formalism established for semicrystalline polymers:

$$RAF = 1 - X_{SiO2} - \left. \frac{\Delta c_p{}^{nc}}{\Delta c_p{}^{PHEA}} \right|_{Tg} \qquad \text{(Eq 3.1)}$$

where X_{SiO2} is the silica fraction and Δc_p^{nc} and Δc_p^{PHEA} the specific heat capacity increments at T_g for the nanocomposites and pure PHEA, respectively. Rigid amorphous fraction only regarding the organic phase (RAF_{pol}) can be computed by [132,133]:

$$RAF_{pol} = 1 - \left. \frac{\Delta c_p{}^{nc}}{\Delta c_p{}^{PHEA}} \right|_{Tg} \qquad \text{(Eq. 3.2)}$$

Figure 3.27 presents the RAF_{pol} evolution. Assuming that the regression line which defines RAF_{pol} up to 30wt% also rules the behaviour of hybrids with higher silica contents (>30wt%), it is expected for 38wt% that the mobile amorphous fraction (*MAF*, the unperturbed polymer fraction) vanishes. It means that glass transition

will be absent (or sharply displaced towards higher temperatures) from this SiO_2 content on. Similar results of the glass transition disappearance were previously reported [46,134].

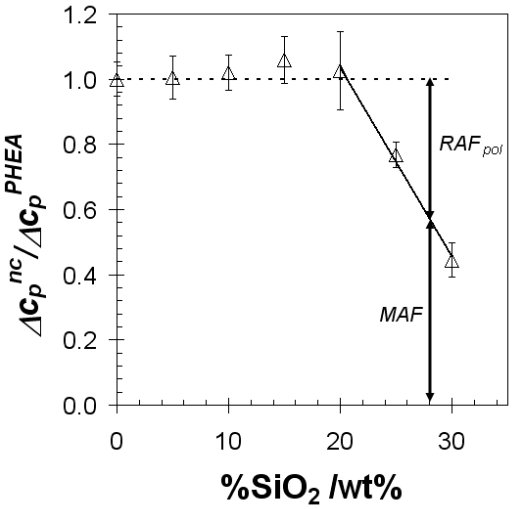

Figure 3.27. Silica dependency of RAF_{pol}. The dashed line represents hybrid systems without PHEA confinement; solid line is a linear regression which accounts for *RAF* in hybrids with high silica contents. Vertical double arrows show the mobile amorphous fraction (*MAF*) and the rigid amorphous fraction of the polymer phase (RAF_{pol}, see text).

Silica percolation takes place at lower silica content (~15wt%) than those needed for significant confined PHEA fractions (>20wt%). It does not mean that interpenetration between organic and inorganic networks only takes place at those contents; on the contrary, it occurs regardless the silica percentage, but its fraction referred to the whole phase is only meaningful at the highest SiO_2 contents. Obviously, it seems that co-continuity and polymer constraint are related: following the nanocomposite structure depicted until now (Figure 3.11), through silica percolation the average size of the spaces between SiO_2 aggregates starts to diminish and, as a consequence, more PHEA segments are in an intimate contact with the silica surface, enhancing their physical interactions. However, the occurrence of one of these

related phenomena (for instance silica percolation) does not directly imply the occurrence of the other (i.e. meaningful fractions of confined organic polymer): it takes place with hybrids at silica contents around 15wt%.

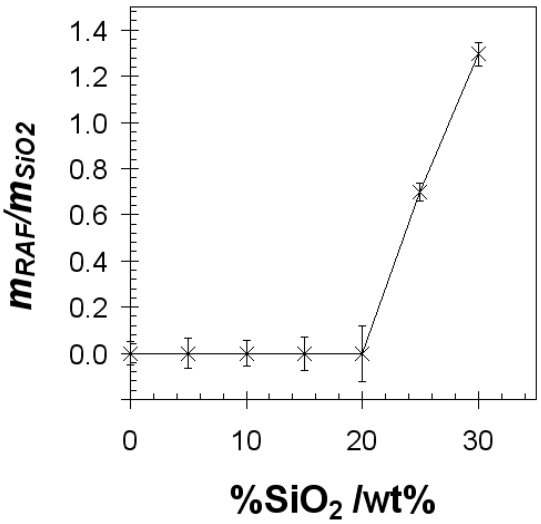

Figure 3.28. Evolution of the percentage of rigid amorphous fraction (*RAF*) with silica. Lines between points are guides to the eye. Vertical bars are errors estimates obtained by error propagation laws.

Figure 3.28 shows how the rigid amorphous fraction relative to the silica percentage evolves with SiO_2: for small inorganic amounts, PHEA confinement probably only takes place as a consequence of the filling of the holes within single silica particles (Figure 3.11) [50,116] and therefore this hindered PHEA fraction is not meaningful in comparison with the huge unperturbed organic one; nevertheless, for higher inorganic percentages, the spaces left between the aggregates of single particles which are filled by the polymer phase begin to diminish their size and, as a consequence, the physical interactions between both phases are enhanced. Additionally, the spaces between SiO_2 aggregates are decreasing (i.e. the unperturbed polymer fraction). Further SiO_2 increases yield a significant fraction of PHEA chains segments in close contact with silica which finally become constrained. This hypothesis is supported by the widening of the glass transition

(Figure 3.23 and Figure 3.25) as a result of the different mobility environments which surround PHEA molecules as the silica percentage increases and percolates.

Another issue which points to a significant increment of the confined PHEA fraction is the fact that DSC profiles of the samples (referred to the polymer mass, not to the sample mass) do not coincide after a proper rotation and shift on the ordinate axis [82]. If PHEA phase were not disturbed at all by the coexistence with silica, it would behave as the pure homopolymer does regardless the inorganic phase amount, and thus thermograms must coincide when referred to the polymer mass. Nevertheless, it does not happen: first, because of the T_g increase (Table 3.2), even for small silica inclusions, which accounts for hindrances of the polymer phase; and second, because $\Delta c_p\big|_{Tg}$ is higher for PHEA than for those samples with the highest silica percentages (referred to the polymer mass, Table 3.2). This is consistent with the results presented on Figure 3.28. Besides, taking together the T_g and $\Delta c_p\big|_{Tg}$ results once the silica dependence of the constrained polymer fractions are defined, it is noteworthy that there is an increase of the glass transition temperature for silica contents up to 20wt% without a specific heat capacity decrease. However, from this content on, $\Delta c_p\big|_{Tg}$ significantly diminishes without an additional T_g increase; on the contrary, it remains constant. Therefore, it seems that T_g variations arise essentially from the physical interactions established between composite phases rather than polymer confinement effects. Likewise, silica percolation is not reflected in any T_g change.

When some segments of the PHEA chain are perturbed due to physical interactions with silica, the loss of mobility affects the rest of the segments belonging to the same cooperative rearrangement region (CRR); [82]. This phenomenon may account for the fact that an increase of the silica amount above the silica continuity threshold (>15wt%) does not imply a significant T_g increase (Table 3.2): although the interaction between phases is enhanced by confinement (probed by the increase of the RAF_{pol}), the glass transition temperature does not

significantly change, perhaps because of the corresponding cooperative rearrangement regions were already not able to relax at lower inorganic concentrations.

Polymer molecules become more mobile when departing from the interface, and thus it is established a mobility molecular gradation from the completely immobilized PHEA at the organic-inorganic interface to the liquid-like polymer [130]. The broadening of the glass transition measured by ΔT_g (Table 3.2) is the magnitude which accounts for that gradation of molecular mobility when the thickness of the disturbed PHEA molecules surpasses the range of the physical (electrostatic and dipole-dipole) interactions between phases.

Finally, another magnitude related with the segmental mobility of the polymer chains is the density of cohesive energy [135]. Cohesive energy density is defined as the molar energy of evaporation per unit molar volume which holds the molecules together, being thus a measure of the intermolecular interactions between polymer chains. An approximate estimate of the change of cohesive energy density at the glass transition, $\Delta H_{coh,g}$, can be obtained from the relationship

$$\Delta H_{coh,g} = C_2 \Delta c_p \Big|_{Tg} T_g \qquad \text{(Eq. 3.3)}$$

with C_2=2.80±10% [135]. Using the experimental values of T_g and $\Delta c_p \Big|_{Tg}$ given in Table 3.2, the results represented in Figure 3.29 are obtained. Once again, there is a similar trend in comparison with other macroscopic magnitudes: firstly, the cohesive energy evolution slightly increases with small silica inclusions (up to 20wt% SiO_2) with a subsequent sharp decay from this content on. Considering the error estimates, the cohesive energy probably does not change at all with low inorganic percentages: the polymer state of nanocomposites organic phase regarding this matter up to 20wt% is the same than that corresponding to neat PHEA. However, for higher SiO_2 contents (<20wt%), the states of the polymer above and below the glass

transition as regards the mobility of its chains are more similar, consistent with the tendency of the fragility parameter obtained by isothermal DMA measures to approximate the linear Arrhenius behavior with increasing silica contents of the PHEA-based nanocomposites [73].

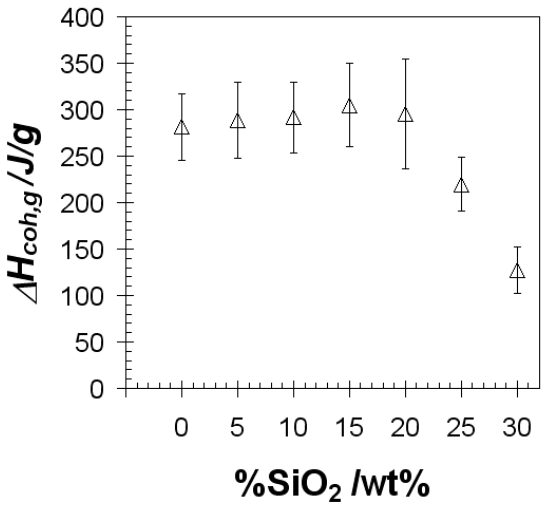

Figure 3.29. Silica content dependence of the increment of cohesive energy density ($\Delta H_{coh,g}$) at T_g. Error bars are the result of an error propagation law.

3.3.5. Physical ageing in nanocomposites

A probe of molecular mobility is the structural relaxation of molecules revealed by enthalpy recovery in so-called ageing experiments. It thus seems of interest to check the mobility of the rigid amorphous fraction making use of this technique. Silicate-layered nanocomposites show two opposite tendencies which rule the occurrence and broadening of the cooperative main relaxation phenomenon: the existence of a less constrained phase than that of the bulk which includes molecules within galleries (spaces left between neighbour silicate layers); and hindered molecules at the interface between the organic and inorganic phases. This balance establishes the widening of the glass transition as well as the shift of T_g [39,136].

Results of Lu and Nutt regarding physical ageing on montmorillonite-epoxy nanocomposites yielded to a slowdown of the main relaxation when compared with the neat polymer [136]. Besides, Priestley et al lately related the fall of the secondary relaxation on silica-filled PMMA nanocomposites with the hindered PMMA molecules at the filler surface making use of the enthalpy recovery decay on physical ageing assays [115]. Closer to PHEA-silica hybrids, reference [137] deals with the enthalpy recovery of PHEMA-derived sol-gel nanocomposites with also a delay of backbone relaxation and a shift to higher temperatures of the enthalpy maxima with the silica growth.

Molecular dynamics simulations show that T_g increases in systems with attractive interaction between the organic and inorganic phases and clearly decreases in systems with only an excluded volume interaction [130]. Furthermore, the interface interactions in polymer nanocomposites might lead to the suppression of physical ageing in the system [52]. T_g increase (or decay) observed in some nanocomposites has been interpreted using an analogy with thin-film polymer films, what allows to identify some 'liquid-like' regions surrounding different particles [51]. The existence of a double glass transition on nanocomposites implies the occurrence of two clearly different polymer phases: one regarding the not disturbed bulk polymer, and the other accounting for confined molecules, both with a narrow molecular mobility distribution around them; on the contrary, only a broadening will be shown if there is a gradation of mobility from the liquid-like bulk polymer to the completely constrained molecules at the silica surfaces. Whatever the situation, neither T_g nor ΔT_g are able to show if there is any change on the kinetics of the cooperative conformational rearrangements of the polymer chains owing to the presence of a silica phase, i.e. an influence on the structural relaxation process. A deeper insight into the kinetics of this process can be obtained by carrying out DSC experiments which include isothermal annealing at different temperatures close to T_g so as to study the influence of the silica content on the enthalpy recovery process.

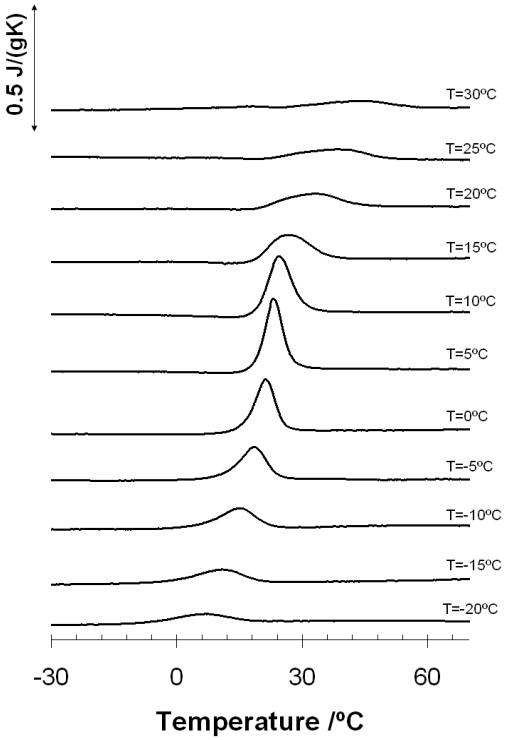

Figure 3.30. Temperature dependence of $(c_p\text{-}c_{pref})$ for PHEA+20wt% SiO_2 after annealing at different temperatures (indicated at the right hand side of the figure) during 200 min. The profiles were shifted in the ordinate axis for the sake of clarity.

Experimental DSC curves were measured after relaxation experiments of 200 min at different temperatures (from -20 to 30ºC with a temperature increment of 5ºC). After each thermal history, a heating thermogram was recorded and then a reference scan followed with no manipulation of the sample and pans in the DSC holder. The difference between these two thermograms equals the difference between the heat capacity in the annealed and in the reference scans ($c_p\text{-}c_{pref}$) [91]. The curves obtained for PHEA with 20wt% silica are shown in Figure 3.30; similar results were obtained for the other samples (see Appendix 3). The endothermic peak observed, whose intensity and position are dependent of the annealing temperature (T_a)

for a fixed ageing time, tends to vanish both at temperatures sufficiently higher and sufficiently lower than T_g. The presence of this ageing peak after annealing at a given T_a reveals that some conformational motions are still possible, relaxing the enthalpy during the isothermal period towards its equilibrium value. The height of the peak increases as T_a does, because the approach to equilibrium is faster the higher the temperature is. On the other hand, for a sufficiently high T_a, close to the T_g value, the rate of the structural relaxation process is high, but the enthalpy recovery is small because the material is close to equilibrium during the annealing (the enthalpy loss evolution with T_a shows a maximum at a certain ageing temperature due to these two opposite physical tends [138]).

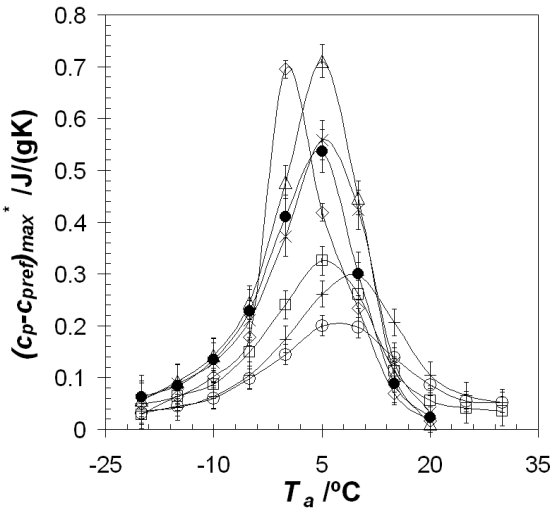

Figure 3.31. Annealing temperature dependence of the maximum of $(c_p\text{-}c_{pref})_{max}^*$ (referred to polymer mass) during isothermal ageing for 200 min: (◇) pure PHEA; (△) 5wt%; (●) 10wt%; (×) 15wt%; (□) 20wt%; (°) 25wt%; (+) 30wt%. Vertical error bars were computed as the standard deviation of Δc_p at T_g for different thermal histories. Curves between points are a guide to the eye.

The enthalpy loss during the relaxation process can be determined by calculating the area under the $c_p\text{-}c_{pref}$ curves. Computing areas yields large measurement errors, mainly due to the definition of

the liquid line. Since similar information can be also obtained by plotting the maximum of the c_p-c_{pref} curves, $(c_p\text{-}c_{pref})_{max}$, as a function of the annealing temperature T_a [137,139,140], it is used so as to minimize uncertainties. This plot defines a temperature interval where conformational rearrangements can take place in the glassy state at moderate experimental times. Figure 3.31 shows the position of the maximum in the $(c_p\text{-}c_{pref})_{max}^*$ curves (referred to the polymer mass) which moves towards higher temperatures (5ºC) with small silica inclusions, whereas a higher shift is observed for the largest silica percentages (around 10ºC for 25 and 30wt%). This shift to higher temperatures is likely induced by the T_g increase, and thus the maximum of $(c_p\text{-}c_{pref})_{max}^*$ was plotted versus $(T_g\text{-}T_a)$ (Figure 3.32). Conformational motions are somehow extended in the high temperature side, i.e. there is a broadening of the temperature interval in which conformational motions take place induced by the presence of a silica phase. The value of $(c_p\text{-}c_{pref})_{max}^*$ measured after annealing at a given temperature T_a is proportional to the number of configurational rearrangements that contribute to the relaxation process at T_a. If the temperature interval in which the glass transition takes place is narrow, most of the mass of the material relaxes at the same rate at each annealing temperature, and consequently the peak in the $(c_p\text{-}c_{pref})_{max}^*$ vs T_a plot is higher. On the contrary, a broad glass transition interval reflects the presence of different microenvironments surrounding the organic phase inside the material and, as a consequence, at every annealing temperature, only a part of the polymer segments participate in the structural relaxation process. Heterogeneous systems show narrower and broader peaks in the $(c_p\text{-}c_{pref})_{max}$ curve [137,140]. It is suggested that the temperature interval where conformational motions take place in these systems significantly widens for silica percentages above the threshold of percolation, but the contribution at each temperature is smaller. When $(c_p\text{-}c_{pref})_{max}^*$ curves are plotted versus $(T_g\text{-}T_a)$ (Figure 3.32), the maximum is found at approximately 20°C below T_g for pure PHEA and hybrids up to 20wt% and 15ºC for composites with the highest silica contents (<20wt%). Furthermore, the curve broadens towards the annealing temperatures above T_g. A broad glass transition interval reflects the presence of T_g distribution in the material and only a part of the polymer segments participating in the structural relaxation process at each temperature. The meaningful

presence of cooperative rearranging regions relaxing at higher temperatures than T_g suggests PHEA hindrances (sometimes removals) due to the enhancement of attractive physical interactions (mainly hydrogen bonding) through spatial polymer confinement [52,115,128].

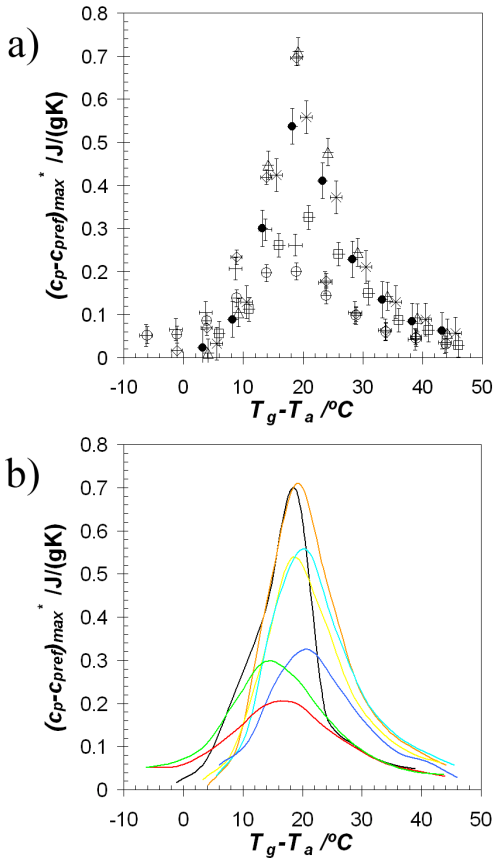

Figure 3.32. Maximum of $(c_p-c_{pref})_{max}^*$ (referred to the polymer mass) vs (T_g-T_a) during isothermal ageing: (◇) pure PHEA (black line); (Δ) 5wt% (orange line); (●) 10wt% (yellow line); (×) 15wt% (cyan line); (□) 20wt% (blue line); (°) 25wt% (green line); (+) 30wt% (red line). Vertical error bars on a) are the standard deviation of Δc_p at T_g for different thermal histories, whereas the horizontal error bars are the outcome of error propagation laws; in b) both symbols and error bars are erased for the sake of clarity.

3.4. Does a hydrophilic environment influence the morphology of the in situ sol-gel generated silica?

The HEA/EA ratio was systematically varied to obtain materials with different organic matrices (see *2.1.2. Copolymer nanocomposites*). -OH_x will account for the HEA amount relative to the organic phase (for instance -OH_{30} identifies the nanocomposite whose HEA/EA percentages equal 30/70). The synthesized hybrids as regards the organic phase are OH_{10}, OH_{30}, OH_{50}, OH_{70}, OH_{90}, where the former composition concerns to the highest hydrophobic system.

Firstly, it must be highlighted that all the synthesized materials are transparent though a phase separation occurs when both phases polymerize: they are not thermodynamically compatible, but the average silica phase size does not surpass tens of nanometres because otherwise it would disperse the light (translucent instead of transparent samples). This hypothesis concerning the silica size is further confirmed by TEM micrographs of nanocomposites with different organic matrices and the lowest silica content (5wt%) in Figure 3.33. It is possible to distinguish on them isolated darker areas with such low inorganic percentages which are ascribed to silica. Higher silica percentages (<10wt%), on the contrary, loses this clear distinction between phases. Silica aggregates do not appear in TEM images as completely dark motifs, and thus they must be porous probably because of the polymerization conditions. Likewise, one can find some differences when compared with each other; however, they are sometimes either subtle (like the silica size) or impossible to confirm (like the density of the aggregates which appear in each TEM image due to a possible variable slice thickness). Perhaps other techniques more sensitive to the silica morphology or which yield quantitative parameters regarding its topology (for instance, fractal dimension) should be used so as to ascertain whether there is a real influence of the organic phase.

Silica was also gelified at the presence of HEA-EA mixtures but without the thermal initiator addition (Figure 3.34). The AFM images of those silicas surfaces show that sometimes there are some small differences of the aggregates size which in turn depend on the scanned areas (for instance compare Figure 3.34a with c); however, if they

definitively exist, they are too small in order to conclude by direct observations (TEM and AFM) that the organic phase in where silica is synthesized has an influence on the silica morphology.

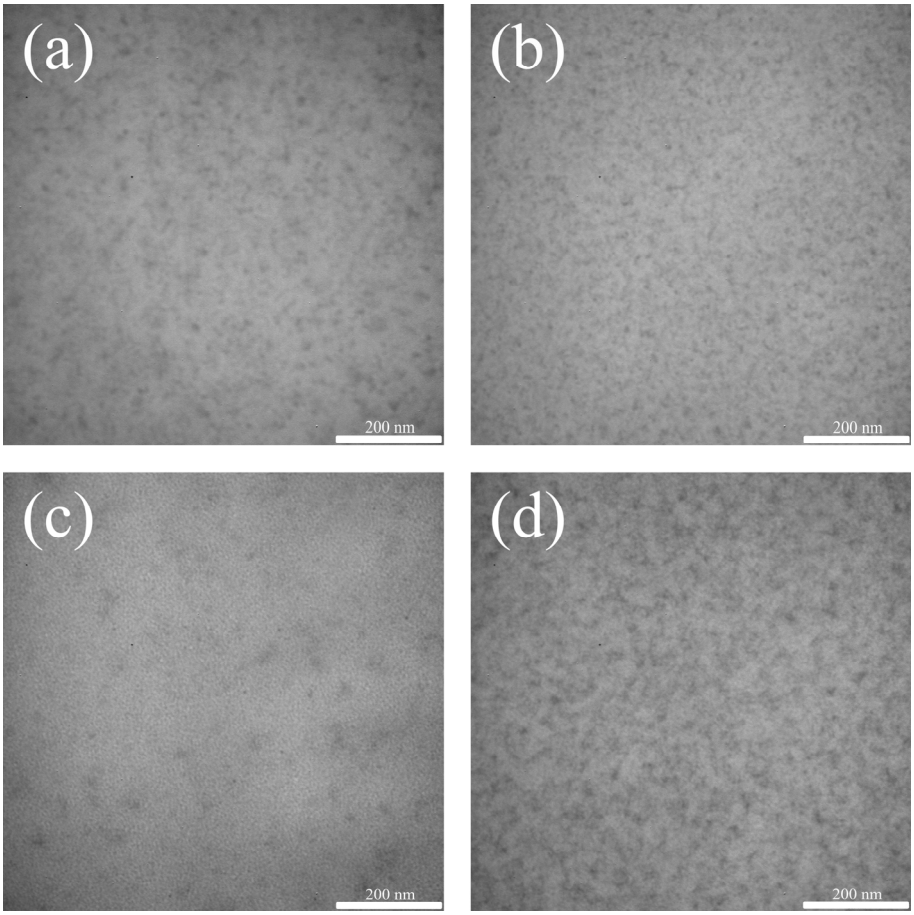

Figure 3.33. TEM images for nanocomposites at 120000x with a fixed silica content (5wt%) and different organic matrices: (a) $-OH_{90}$; (b) $-OH_{70}$; (c) $-OH_{50}$; (d) $-OH_{10}$.

Silicon EDS was also performed on cryo-fractured surfaces of these systems (data not included). Results (as well as the conclusions yielded by them) are similar to those exposed to PHEA-SiO_2 hybrids (see *3.1.2. Silica dispersion on PHEA-based sol-gel hybrid systems*,

Figure 3.9); briefly that silica is widely spread at a micro-scale level, no matter the silica percentage.

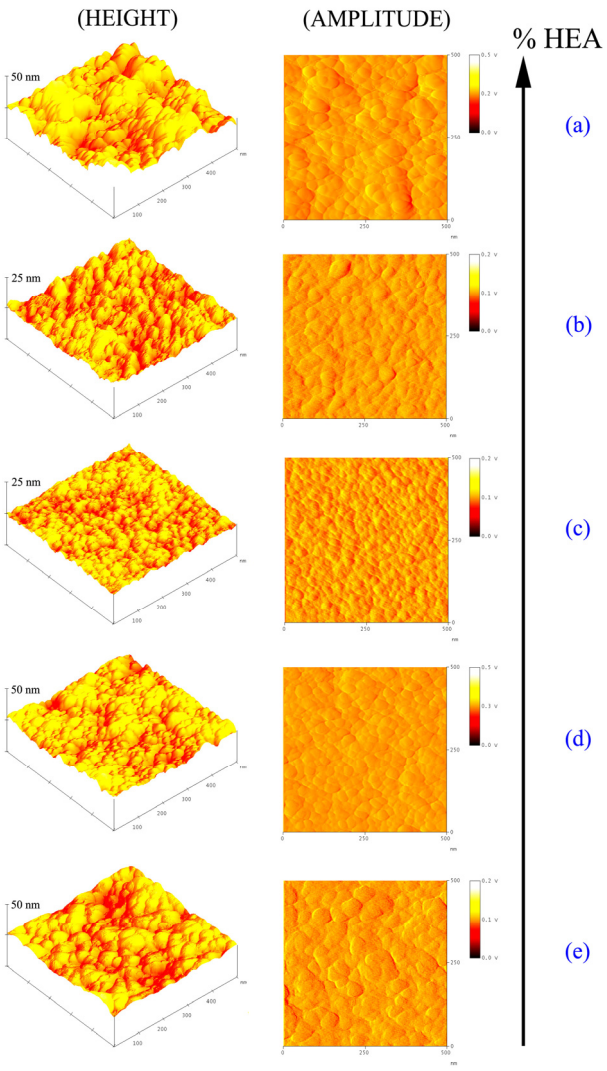

Figure 3.34. 500x500 nm AFM images (height and amplitude) of silicas surfaces gelified in the presence of different HEA-EA solutions: (a) *–OH$_{90}$*; (b) *–OH$_{70}$*; (c) *–OH$_{50}$*; (d) *–OH$_{30}$*; (e) *–OH$_{10}$*.

3.5. Nanocomposite scaffolds with ordered cylindrical orthogonal pores

In this section it is explained a procedure to synthesize porous materials made of hybrid biphasic materials of silica and PHEA. The scaffold porous morphology consists of a mesh of cylinders (pores) which are interconnected by circular transversal holes [141]. The silica inclusion within a PHEA phase increases the elastic modulus of the materials, as is probed in previous sections for bulk materials (see *3.3.1. Mechanical properties*), and does in scaffolds.

3.5.1. Pore structure

With the methodology described at the materials and methods section (see *2.1.3. Nanocomposite scaffolds*), we were able to obtain scaffolds made out of a nanocomposite material with a well-ordered three-dimensional cylindrical pore mesh. Figure 3.35 shows different views at the same magnification of the sintered fabrics acting as porogenic templates. There are interconnected spaces within the template which allow a liquid solution to fill them and be finally polymerized inside them. Also remarkable is the circular cross section of the fabric threads. Figure 3.36a shows a general view of the front face of a scaffolds sheet, while Figure 3.36b gives a detail showing the interconnections. The thickness of the final scaffold depends on the amount of sheets employed in the templates. Figure 3.37 shows micrographs of scaffolds with different thicknesses. It is also possible to assess the pore size and shape in Figure 3.37c. The diameter of the cylinder holes is approximately 80 μm, in agreement with the employed fabric's thread diameter. This fact points out that the filling process of the available spaces inside templates was effective enough. Furthermore, the shape of the pores appears circular, not being affected by compression. Nonetheless, for the highest compressions the circular shape of the fabric threads becomes deformed.

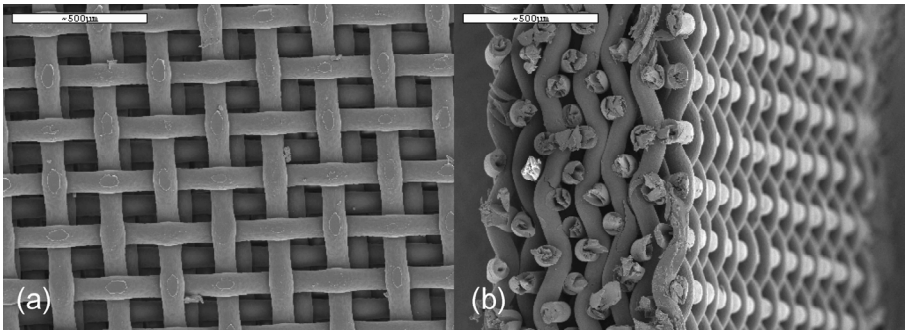

Figure 3.35. SEM images showing compressed and sintered templates of 8 sheets: (a) frontal view; (b) cross-sectional view.

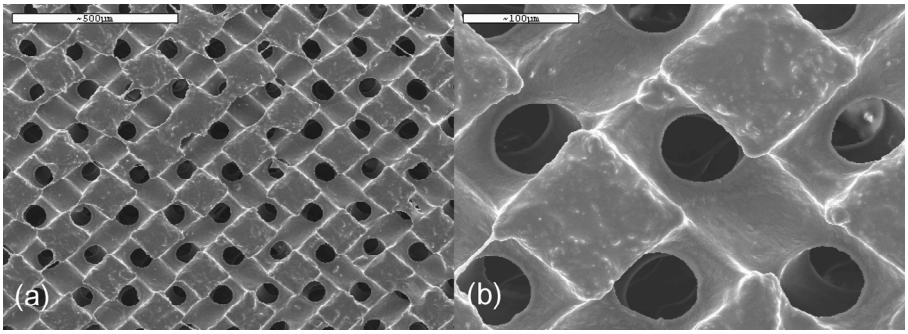

Figure 3.36. SEM images of a scaffold frontal view: (a) general cylindrical pore distribution; (b) detail of the interconnections normal to the frontal plane.

In comparison with other scaffold morphologies, this cylindrical structure is more stable against the pore collapse phenomenon which takes place with other fabrication procedures [7,142]. Furthermore, it is expected that the mechanical properties of the scaffolds we are dealing with should be larger than those corresponding to other pore geometries [143,144], mainly due to less porosity values (~60% *versus* ~80% for interconnected spherical pores).

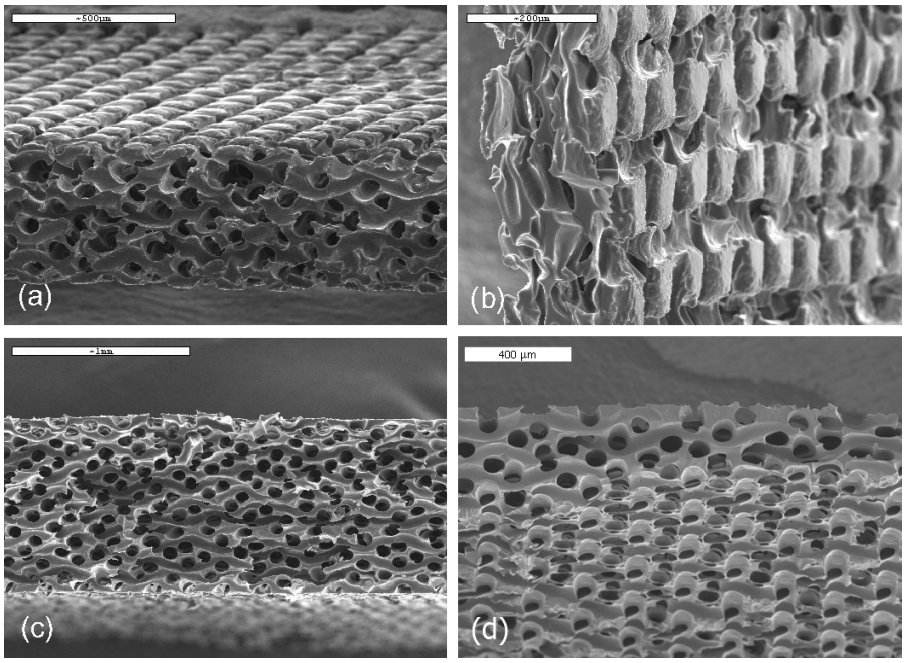

Figure 3.37. SEM images of cross sections of nanocomposite scaffolds with different thicknesses obtained with a compression weight of 4 tons: (a), (b) and (d) scaffolds prepared with 8 textile fabrics; (c) scaffold prepared with 16 fabrics. Pore cylinder diameter coincides with fabric thread diameter.

The manufacturing method used gives rise to well-ordered porous structures which can be made of several materials, including composites. The silanols existence within the silica network of the nanocomposite (see *3.2. Chemical and/or physical bonds between organic and inorganic phases?*) accounts for a possible bioactivity of these scaffolds [72]. The geometry of the resulting porous structure depends directly on the geometry of the employed fabric template. Therefore scaffold properties (pore diameter, distance between neighbouring cylindrical holes and pore distribution) can be easily varied by changing the fabric type and the compression force applied. As a result of sintering and compression process to which the fabrics are subjected, localized melts occur in the areas where neighbouring stacked fabrics are in contact. These melted areas give rise to the

interconnecting holes transversal to the cylinder pores. This formation process of the pores normal to the frontal face of the scaffold can be followed in a computer simulation of the structures created. Figure 3.38 shows the simulated pore structure of a scaffold with such an inter-fabric distance implying no compression (fabrics only touch themselves but do not interpenetrate). The simulation does not show up transversal pores which give rise to tridimensional interconnectivity (Figure 3.38c). Figure 3.39 simulates a pore structure where the distance between neighbouring sheets was smaller, simulating the result of a compression. The resulting pore structure shows spaces transversal to the cylinder pores (Figure 3.39d) very similar to those appearing in Figure 3.36. The number of those normal holes is larger in the model than in the real scaffold since there are differences of position and sheet distance between the simulation and the actual scaffold. However, the modelling clearly demonstrates the need of a proper compression for the normal interconnecting holes that appear in Figure 3.36 to arise.

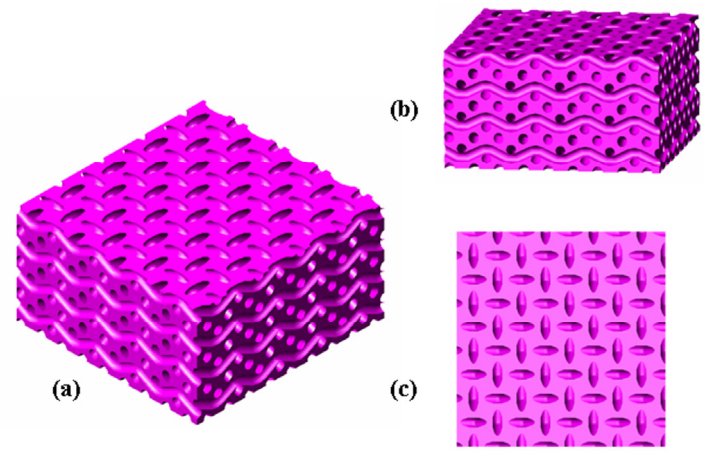

Figure 3.38. Simulated pore structure of scaffolds with a compression not leading to transverse pores: (a) and (b) show three dimensional views; (c) two dimensional view revealing that no interconnection is produced between neighbour stacked sheets.

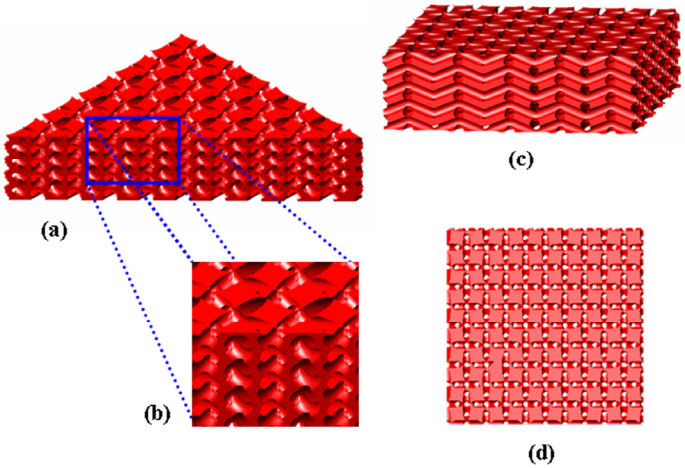

Figure 3.39. Simulated pore structure of scaffolds with proper parameters of the sintering process: (a) three dimensional section; (b) detail of the connected structure; (c) three dimensional view corresponding to the actual case of Figure 3.37a; (d) two dimensional view revealing the interconnections shown in the actual case in Figure 3.36b.

The porosities computed by the apparent density method are listed in Table 3.5. Similar results for dried scaffolds were obtained by mercury porosimetry. The two pore sources in this manufacturing procedure (i.e. the fabric's thread and the localized melting between neighbouring sheets) are reflected on the pore distribution when they are studied by mercury porosimetry. The pore number distribution (Figure 3.40) is centred on a diameter value equal to 80 μm (high increase in the volume of mercury intruded), which coincides with the thread radius of the employed fabric. It means that the main pore diameter will be defined by the fabric and not by the sintering process (as expected), whereas the small pores raising below 40 μm are the outcome of the sintering between neighbour fabric sheets, with contributions to porosity not so large (a slight increase in the mercury volume intruded). Nonetheless, the potential application of these scaffolds requires interconnectivity, what make these smaller pores crucial to its success.

Sample ID	Nº fabrics	π_{dry} /%	π_{sw} /%
8-PHEA	8	59 ± 3	40 ± 5
8-15wt%	8	52 ± 4	42 ± 7
8-30wt%	8	61 ± 7	46 ± 5
16-15wt%	16	60 ± 5	-----
16-30wt%	16	58 ± 4	-----

Table 3.5. Porosities of dried (π_{dry}) and swollen (π_{sw}) scaffolds with different thicknesses obtained by the apparent density method.

Porosity calculations of the computer simulations shown in Figure 3.38 and Figure 3.39 yield 42.1 and 64.4%, respectively. Dried scaffolds porosity (Table 3.5) lies on between these two limit values: the closer to one of them the larger the similarity with its pore topology.

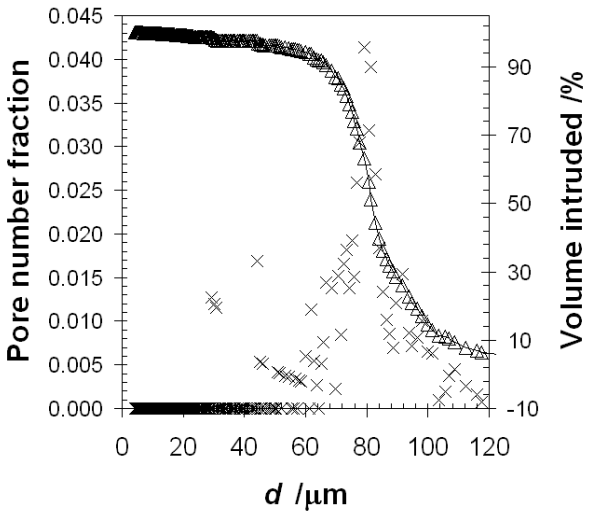

Figure 3.40. Pore number distribution (×) and mercury volume intruded (Δ) when increasing the applied pressure on a porous sample.

3.5.2. The silica phase within scaffolds

Figure 3.41 shows micrographs of silica scaffolds after pyrolysis (originally with 30wt% silica). The final pore distribution is similar to the original one, but with shrunk pore diameter (this phenomenon also appeared when explaining the behavior of the residues of bulky nanocomposites). Briefly, the AFM images of the surface of pyrolysed materials (Appendix 1) exhibit a fine grained topography corresponding to the silica which had constituted the inorganic phase in the nanocomposites before removal of the PHEA phase by pyrolysis [73]. The continuity of the silica phase throughout the scaffold matrix is demonstrated in Figure 3.41: after pyrolysis of the scaffolds, the silica network residue of the nanocomposites was able to withstand the removal of the organic matrix without breaking, retaining the shape of the macroscopic pore structure though somewhat shrunk. Pyrolysis changes the silica network structure by sintering it to a glass [18], producing such a shrinkage. Nonetheless, the AFM topography of the residues clearly shows a structure of silica aggregates with average sizes around tens of nanometres, which give an estimate of the dimension of the typical domain of the silica-rich phase in the nanocomposites.

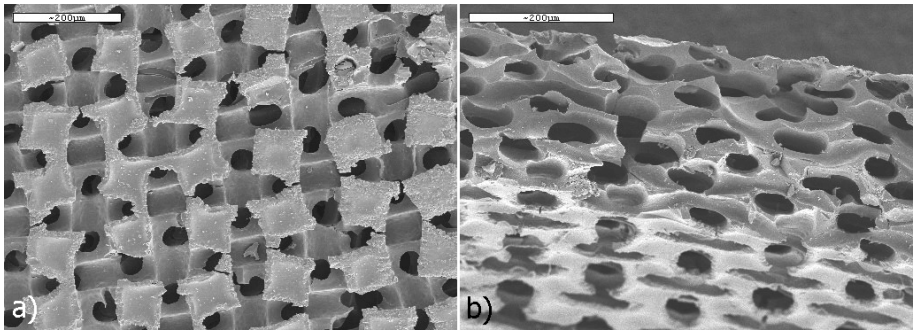

Figure 3.41. Silica residue obtained after pyrolysis of a scaffold with originally 30wt% silica content.

3.5.3. Mechanical properties of scaffolds

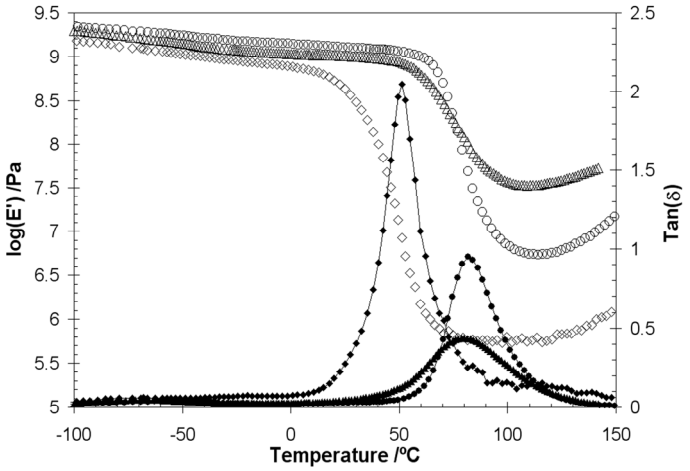

Figure 3.42. Temperature dependence of the storage modulus and the loss tangent of scaffolds with different silica contents and compression weights: (◇) pure PHEA; (○) PHEA-SiO2 15wt%; (Δ) PHEA-SiO2 30wt%. Solid symbols represent loss tangent data.

Figure 3.42 shows the dependence of the storage modulus (*E'*) and the loss tangent (*tan* δ) on temperature of scaffolds for different silica contents and for pure PHEA. Due to its porous structure, their mechanical performance depends on the direction in which they are tested (they are anisotropic). The stretching during DMA was performed on one of the two possible axis directions of the cylindrical pores. The temperature dependence of the porous PHEA elastic modulus shows an unique fall at temperatures significantly higher than that reported for pure PHEA dynamic relaxation [5] (a temperature difference of *circa* 25ºC). Hybrid porous nanocomposites also exhibit single modulus decay, higher than that of porous PHEA (~30ºC). The pronounced fall of the modulus is only due to the glass transition of the matrix polymer: pure silica does not exhibit any transition at these experimental temperatures and thus it does not contribute to the relaxation phenomenon; however, it does to the material stiffness (*E'*). Both the glassy and the rubbery moduli are larger the more silica the

matrix contains, albeit this increase is more apparent in the rubbery region.

Besides, the *tan* δ thermogram shows the main relaxation process of the PHEA polymer, due to the onset of the motion of the main backbone chains above the glass transition. The effect of silica is to lessen significantly the intensity of this relaxation, and to shift to higher values its temperature (as slightly happens with bulk materials, Figure 3.13).

The mechanical properties of scaffolds depend on their structure. The storage modulus of the scaffold relies on the porosity (rather than on pore radius [145]) and on its silica content [146]. Porosity was not significantly affected by the different applied compression loads, and this is why the DMA thermograms of the scaffolds obtained with different compressions were essentially coincident. If compared at a fixed temperature above the glass transition the storage moduli increase significantly with silica content. Notice that even though they are porous, the nanocomposite scaffolds possess a higher modulus than does the pure PHEA polymer. This is a clear proof of the advantage of this reinforcement method for scaffold matrices.

	Pure PHEA	**15wt% SiO_2**	**30wt% SiO_2**
Bulk (MPa)	1.3	3.7	575.5
Porous (MPa)	0.7	6.1	48.9

Table 3.6. Elastic moduli (MPa) at 125ºC for bulk and porous materials.

Table 3.6 compares the rubbery elastic modulus of bulk and porous materials at a temperature above its glass transition (125ºC). Scaffold stiffness should be smaller than that corresponding to the bulk material, in agreement with the experimental results for pure PHEA and the hybrid with 30wt% SiO_2; however, it does not apply for the nanocomposite with 15wt% SiO_2 (Figure 3.42). The differences which exist between the mechanical properties of bulk and porous materials may rely on some kind of material modification during the scaffold fabrication, since even porous pure PHEA relaxes at higher

temperatures (i.e. it does not only concern the silica phase, but also likely both of them). The following section will completely deal with this issue.

3.5.4. Changes in materials due to the scaffold fabrication process

The removal of the template material by a strong inorganic acid may be an inconvenient if the scaffold material is altered. In order to evaluate whether the present process to obtain this porous structure influences the scaffold material, bulk PHEA was immersed in nitric acid for 4 days with periodic renewals. After this exposure time, PHEA was rinsed in boiling water and dried *in vacuum* until constant weight.

Equilibrium water content measures show that PHEA treated with nitric acid (hereafter treated PHEA) looses its hydrogel character since the water uptake falls from 172% for untreated PHEA (Figure 3.18) to 7%. It means that some change, perhaps physical or more likely chemical, involving the *OH* of the pendant side groups is taking place. This change in PHEA may include the catalysis of the etherification and transesterification reactions that this polymeric hydrogel spontaneously undergoes when it is synthesized [13]. This catalysis would mean the loose of hydroxyls and an increase of the crosslink density (i.e. increase of the mechanical properties, glass transition temperature and so on).

Besides, FTIR gives further insights into the problem. Figure 3.43 compares treated and untreated PHEA infrared spectra. First, it is noteworthy the disappearance of the *OH* stretching peak around 3300 cm^{-1}, in agreement with the water uptake drop. Furthermore, two new sharp and intense peaks arise at 1280 and 1625 cm^{-1} in treated PHEA. In order to explain them, it is hypothesized that the exposure of PHEA to nitric acid could give rise to the reaction of some *OH* with the acid to release water molecules and to include a nitro group (NO_3^-) to the lateral chain of the polymer (the symmetric and asymmetric stretching of the nitro group appears at those wavenumber ranges). These

reactions between alcohols and inorganic strong acids are well-known and are used to produce inorganic esters. For instance, sulfuric acid reacts with alcohols following the general equation Eq. 3.5 to form an inorganic ester which acts as a crosslinker between two alkyl chains *R*. However, one can not claim that the catalysis of the aforementioned crosslinking reactions do not take place and in turn both reactions may do.

$$2ROH + HOSO_3H \rightarrow RO - SO_2 - OR + 2H_2O \qquad \text{(Eq. 3.5)}$$

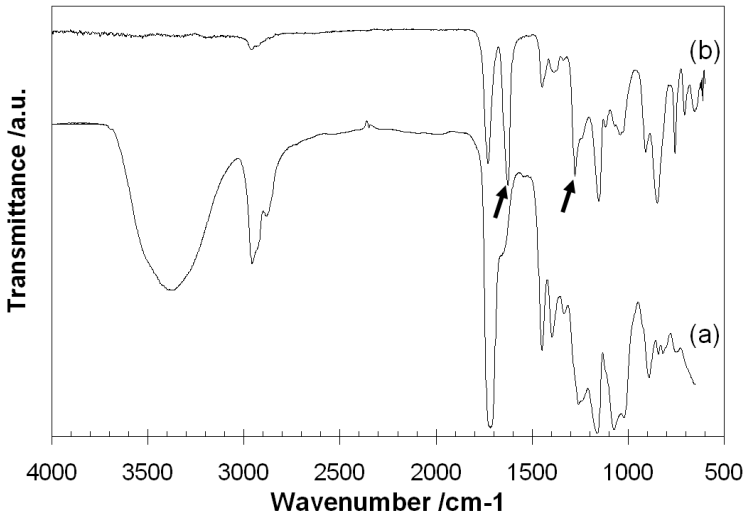

Figure 3.43. FTIR spectra for (a) PHEA and (b) PHEA treated with nitric acid. The arrows point to the new peaks arising in treated PHEA. The spectra were shifted in the ordinate axis for sake of clarity.

DSC of treated PHEA shows an enthalpic glass transition temperature around 104ºC, much higher than that exhibited by pure PHEA (~19ºC, Table 3.2). Nonetheless, the temperature increase on porous PHEA samples (~25ºC) is not as higher as that taking place on

treated PHEA samples (~80ºC): the immersion on nitric acid alters less the PHEA scaffolds, likely due to its saturation owing to the dissolution of the template material (polyamide 6). It is obvious that due to this large change in the glass transition, whatever the reactions which are taking place when PHEA is immersed in nitric acid, they affect to the whole polymeric network and not only at the sample surface.

Again, this T_g increase can be accounted for by both a massive increase of the crosslink density of the network and the existence of big pendant groups at the lateral chain which hinder the mobility of the main macromolecular backbone.

Finally, it is analysed how silica may be altered by the immersion in nitric acid. Studies of Brinker and coworkers in early 1980's suggested that it is possible to depolymerize silica in an environment of *OH*⁻ [16,18] since Eq. 1.2 and Eq. 1.3 are reversed to produce again silanol groups. More current works [147] evaluate the dissolution of crystalline and vitreous silicas immersed at different pH conditions. The conclusion one can extract is the possibility to dissolve the acid catalyzed sol-gel silica which this work deals with. Indeed our results regarding this matter suggest that the inorganic phase of sol-gel silica-polymer hybrid systems can be completely removed at high pH conditions (see *2.2.13. Silica dissolution*).

Silica residues after pyrolysis of nanocomposite scaffolds (Figure 3.41) show it is not dramatically altered by the immersion on nitric acid. The acid pH at which silica is exposed when removing polyamide 6 does not dissolve it. Perhaps there may be small changes on its structure, but it can be concluded that they are not significant at all, in agreement with the reported amorphous silica dissolution rates at different pH conditions [147].

The removal of polyamide 6 with nitric acid affects PHEA. It is thus worth to continue looking for other selective solvents which allow the dissolution of the template but without altering PHEA or other materials, as well as the use of other templates made of easier removable materials (such as polylactide acid, polycaprolactone, etc). However, other physical characterization (e.g. permeability, diffusion,

etc) as well as biological assessments (static and dynamic cell culture, angiogenesis, *etc*) must be done before the use of this porous structure as an implantable scaffold, but they are out of the scope of this work.

Chapter 4

Conclusions

PHEA-silica sol-gel nanocomposites

1. A biphasic material results when HEA monomer and the silica precursor TEOS are simultaneously polymerized. This hybrid material has an organic (PHEA) and an inorganic (silica) phase finely interpenetrated thanks to the porous structure acquired by the silica phase when polymerized within such a kind of liquid template as constituted by the organic monomer. Furthermore, silica is uniformly distributed throughout the hybrid samples, even for small silica contents.

2. The hybrid material obtained by an acid catalyzed sol-gel reaction of the silica precursor TEOS and a free radical polymerization of the monomer HEA shows phase separation at the nano-scale, no matter its inorganic content (up to 30wt% SiO_2). Likewise, silica is completely distributed along the composite and therefore PHEA-SiO_2 hybrids retain the characteristic transparency corresponding to the individual materials by which they are made of.

3. The continuity of the inorganic phase throughout the material depends on its amount: dynamic mechanical results suggest that both phases are co-continuous above a silica percolation threshold around 15wt%. This is one of the most important phenomena taking place as the silica phase enlarges which rules some of the experimental tendencies regarding macroscopic properties.

4. The amorphous silica topology presents a bimodal distribution of pores as a consequence of its built-up: isolated germinal nuclei of SiO_2 begin to polymerize and grow in a fuzzy fashion due to the acid catalyst conditions in which the sol-gel reaction is carried out, finally forming single particles. The linear rather than branched polymer species which form these single particles gives rise to an extremely fine porous structure of these particles, with sizes around few nanometres. Additionally, growing silica nuclei are surrounded by HEA molecules which finally act as a non-surfactant templating liquid and contribute to the nanoparticle porosity production as well. As the single particles coalesce, they group together into bigger nano-aggregates, leaving spaces between them because of their inefficacious stack; this yields another sort of pores. Additionaly, depending on there exist a biphasic continuity or not (that is silica percolation), there will be another pore source which arises from the spaces left between contiguous silica nano-aggregates at lower contents than the percolation threshold (<15wt%).

5. Polymerization rate of the silica is faster than that of PHEA, what avoids a macro-phase separation. Density data point out that all pores left by the silica phase have been occupied by the organic polymer matrix' chains: the apparent specific volumes of both mixed phases coincide with the specific volumes of both pure phases, thus indicating a most efficient packing of the phases, with no interstitial vacancies.

6. The silica inclusion within a PHEA network enhances the mechanical properties of the composite, mainly in the rubbery state, not only in dried but also in swollen samples: there is a 57-fold increase of the elastic modulus in the swollen state of the material with a 30wt% SiO_2 at room temperature. However, this hybrid material is still a hydrogel, with an equilibrium water content equal to 38%.

7. PHEA dynamics is altered by the coexistence with an inorganic phase: there is a shift towards higher temperatures of the main (α) relaxation and a broadening of the glass transition measured by DSC and DMA. The specific heat capacity measured by DSC

(referred to the polymer mass) significantly decreases at silica contents equal to or higher than 20wt%. That decrease suggests that as the amount of silica in the sample increases, the number of polymer chains able to participate in the glass transition process decreases. Furthermore, the temperature range at which conformational motions takes place for pure PHEA is somehow changed by the interactions between the composite's phases (mainly hydrogen bonding) which are enhanced by polymer confinement, with significant enthalpy relaxations above the enthalpic glass transition temperature of nanocomposites with the highest silica contents (<20wt%).

8. Part of the PHEA phase is constrained due to the coexistence with silica. Interpenetration between phases always takes place regardless the silica content; however, it is not significant for small silica contents when it is referred to the unperturbed organic fraction. PHEA confinement takes place because of the filling of the holes within porous silica. Above the silica percolation threshold, increasing the silica contents result in a meaningful abatement of the hole size between silica nano-aggregates and thus an enhancement of interaction between phases (i.e. significant increase of the rigid amorphous fraction).

9. No clear evidence of chemical bonds between both phases can be ascertained, although it cannot be completely excluded that these bonds form to some extent. In this case, they should affect a negligible amount of material, since the hydroxyl groups of the PHEA phase seem to persist with almost intact water sorption capacity.

Nanocomposite scaffolds

10. A highly structured scaffold with cylindrical pores made of a biphasic hybrid material was obtained with the presented procedure. Their geometric characteristics as well as thicknesses

can be easily tailored changing the type of fabric employed and the number of sheets stacked. A further understanding of the final pore structure was gained by modelling the fabric geometry and the compression process, which allowed investigating the effect of compression on the production of interconnecting transversal pores.

11. The use of a hybrid hydrogel nanocomposite as scaffold material matrix greatly improves the mechanical properties; the silica phase of the scaffold was effectively interconnected and continuous, able to withstand pyrolysis without loosing the pore architecture of the scaffold. The existence of silanols in the inorganic silica network gives rise to a potential bioactivity.

12. The main (α) relaxation of nanocomposite scaffolds shown by DMA is shifted towards higher temperatures when compared to bulk hybrids. Additionally, FTIR spectra also yield differences, specially the disappearance of the hydroxyl band at 3400 cm^{-1}. As a consequence of the hydroxyl removal, the water uptake sharply falls. Materials are somehow altered by the followed procedure, mainly because of the immersion in nitric acid during the template removal stage. The resulting biocompatibility of these porous materials is not currently assessed, although cell culture of human chondrocytes was performed using bulk materials. Besides, *in vivo* assays of similar scaffolds but made of by other polyacrylates yielded good results as intervertebral disc replacements, topic that is currently being developed.

13. It is worth trying to find other ways to overcome this inconvenient, either the use of fabrics made of other types of materials (polycaprolactone, polylactic acid, etc) with well-known non aggressive solvents (for instance water or ethanol) or, on the other hand, the use of other less aggressive solvents for polyamide 6.

Appendices

Appendix 1: AFM images of nanocomposites' silica after pyrolysis

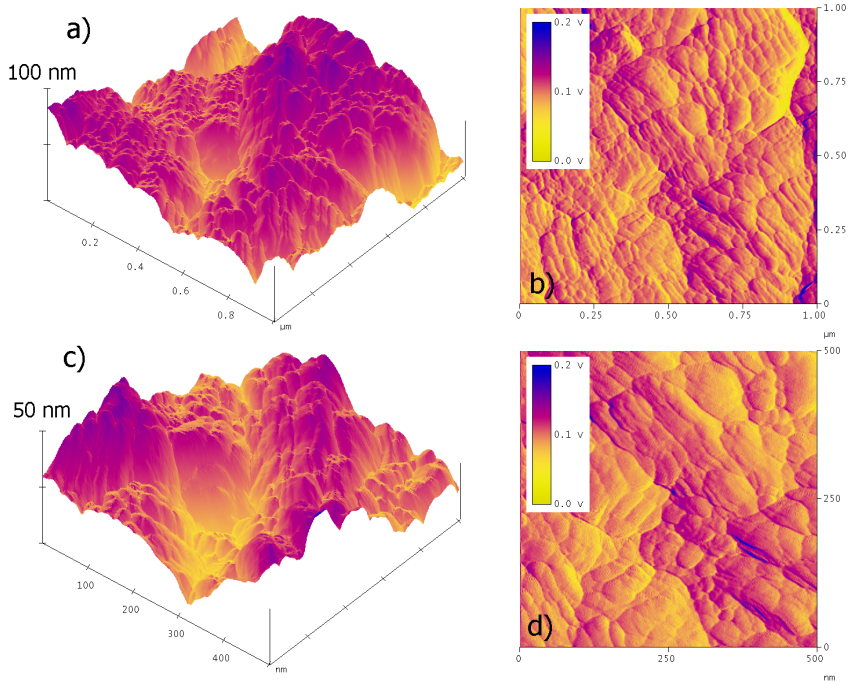

Figure A1.1. AFM height (a-c) and amplitude (b-d) of the TGA residues of PHEA-5wt% nanocomposite at 1x1 µm and 500x500 nm.

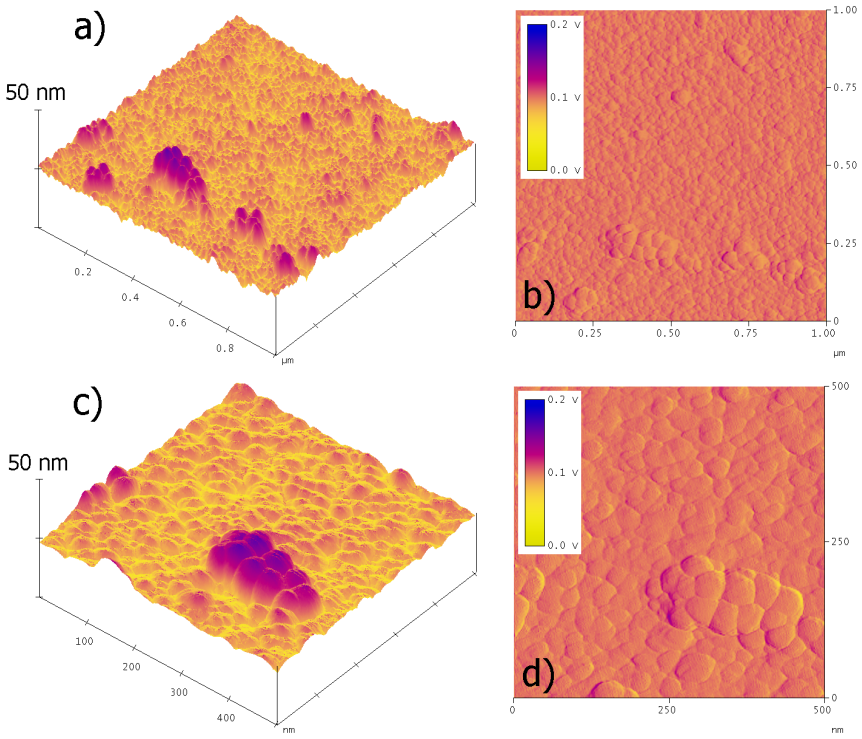

Figure A1.2. AFM height (a-c) and amplitude (b-d) of the TGA residues of PHEA-15wt% nanocomposite at 1x1 µm and 500x500 nm.

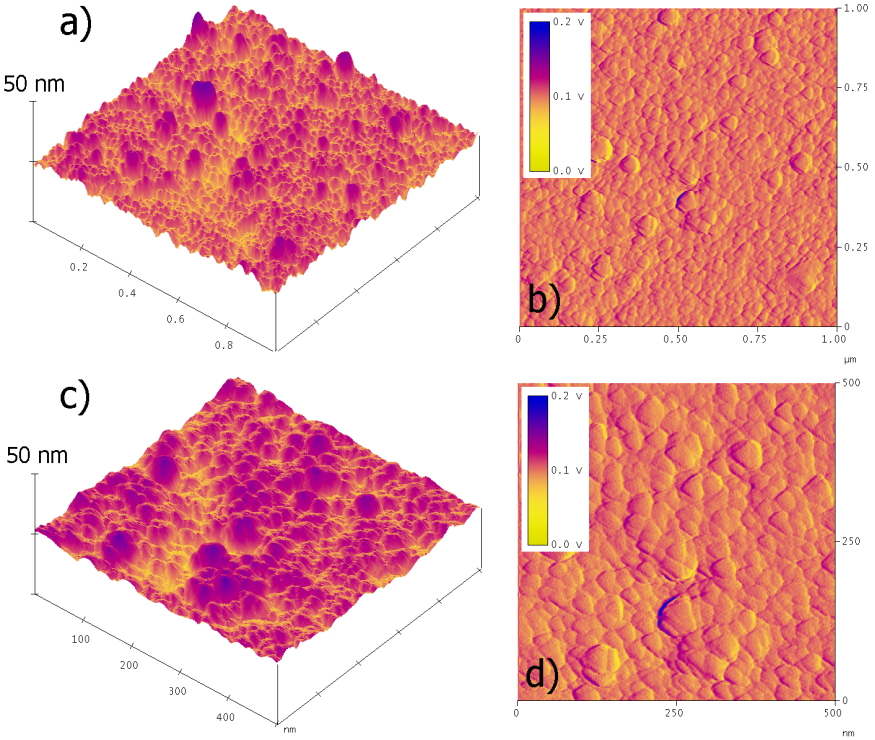

Figure A1.3. AFM height (a-c) and amplitude (b-d) of the TGA residues of PHEA-20wt% nanocomposite at 1x1 µm and 500x500 nm.

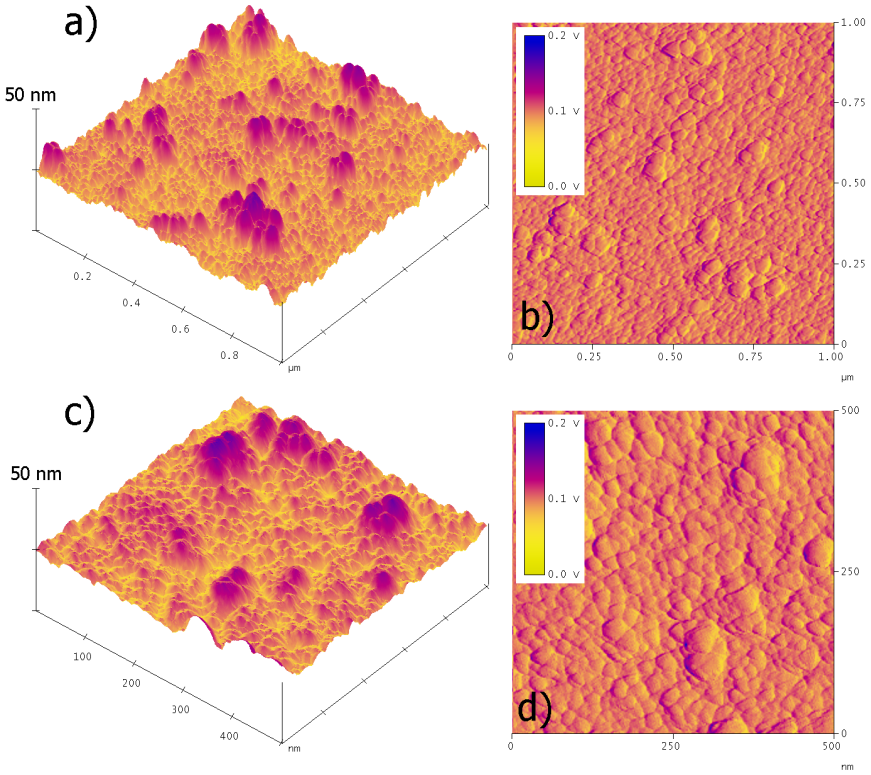

Figure A1.4. AFM height (a-c) and amplitude (b-d) of the TGA residues of PHEA-25wt% nanocomposite at 1x1 µm and 500x500 nm.

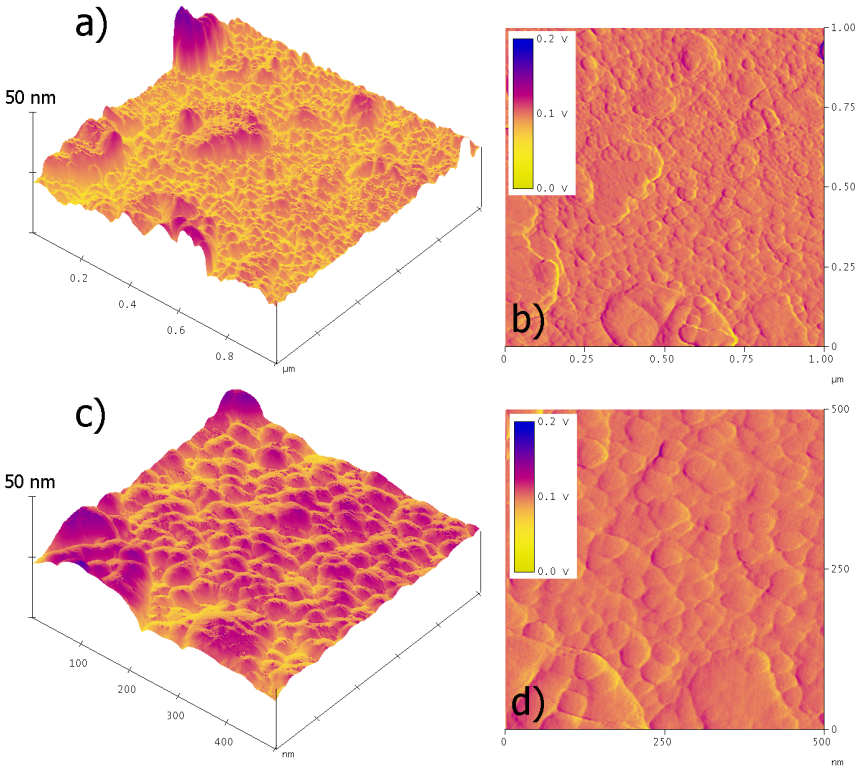

Figure A1.5. AFM height (a-c) and amplitude (b-d) of the TGA residues of PHEA-30wt% nanocomposite at 1x1 µm and 500x500 nm.

Appendix 2: Stiffness of PHEA-silica hybrids measured by nanoindentation

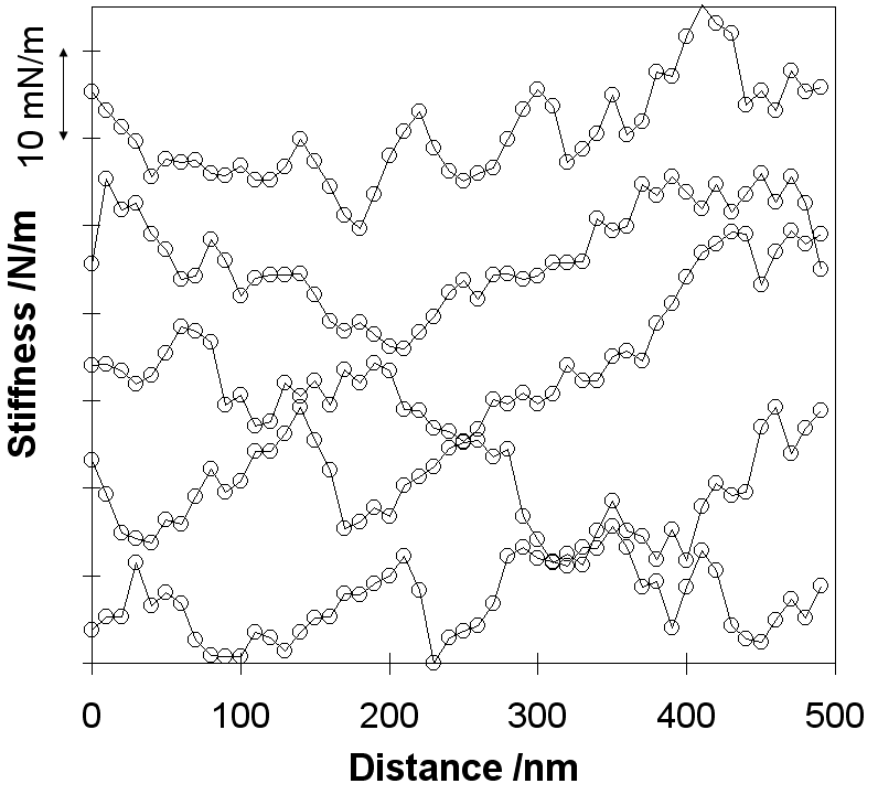

Figure A2.1. Stiffness measured by AFM indentation experiments in the sample with 5wt% silica along 5 parallel lines separated 20 nm from each other. The lines have been shifted in the vertical axis two stiffness units from the precedent one for the sake of clarity.

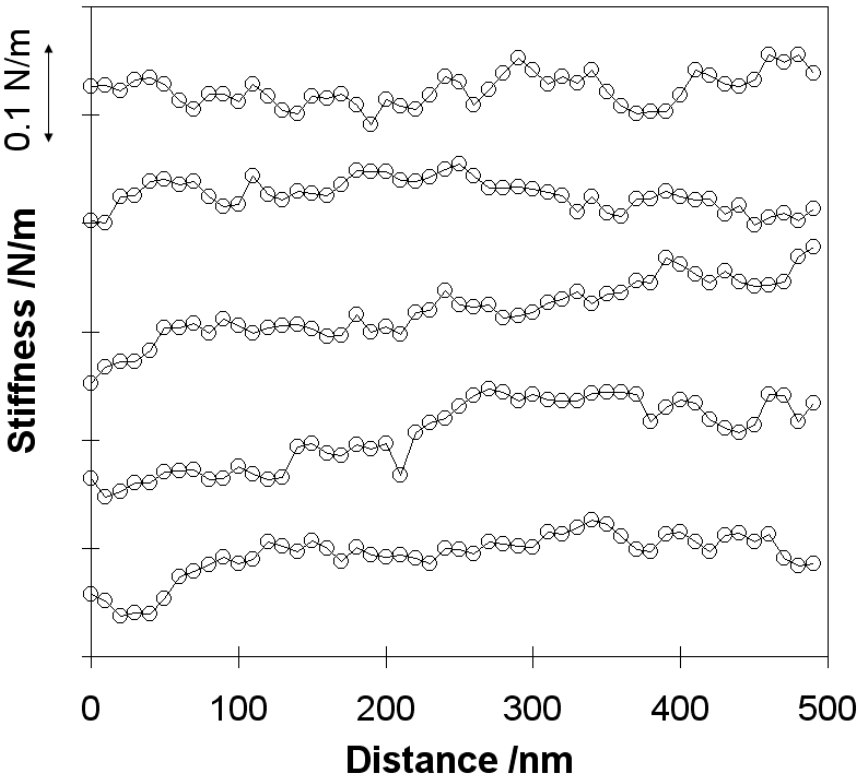

Figure A2.2. Stiffness measured by AFM indentation experiments in the sample with 10wt% silica along 5 parallel lines separated 20 nm from each other. The lines have been shifted in the vertical axis two stiffness units from the precedent one for the sake of clarity.

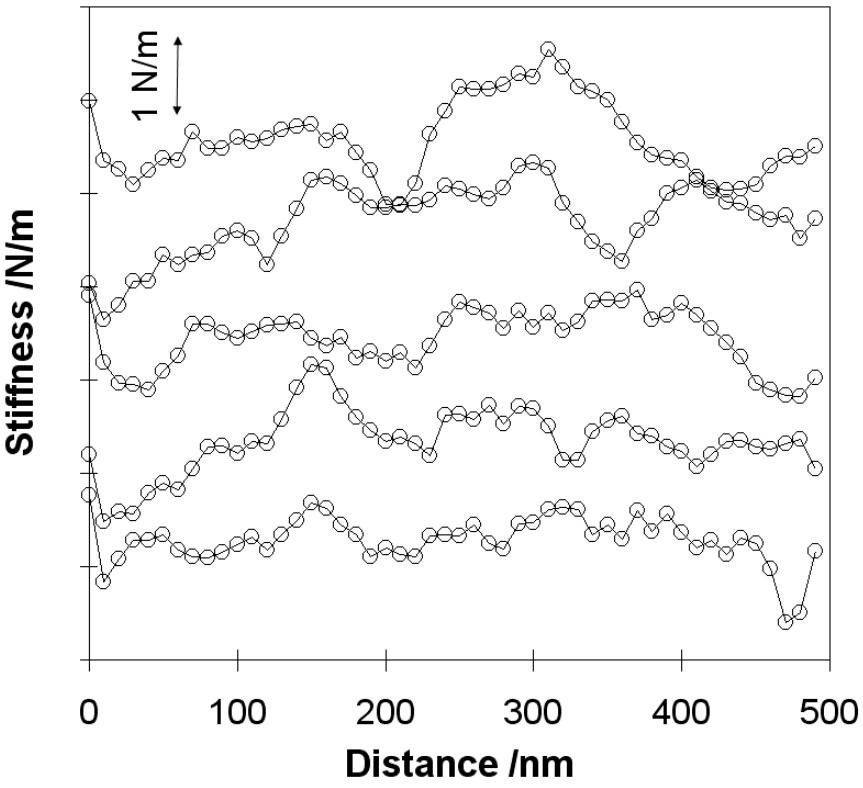

Figure A2.3. Stiffness measured by AFM indentation experiments in the sample with 15wt% silica along 5 parallel lines separated 20 nm from each other. The lines have been shifted in the vertical axis two stiffness units from the precedent one for the sake of clarity.

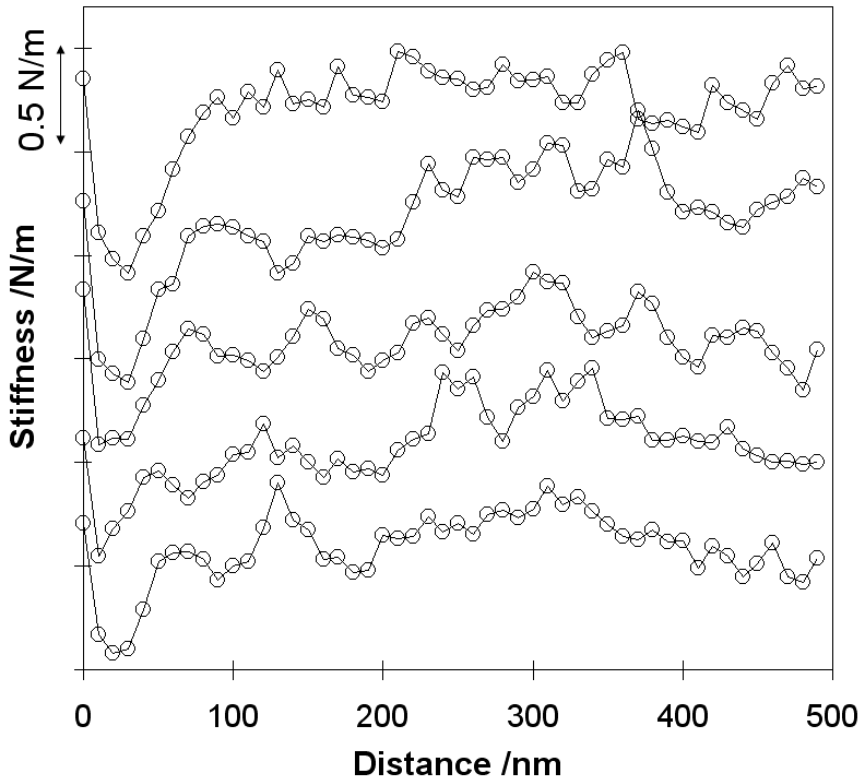

Figure A2.4. Stiffness measured by AFM indentation experiments in the sample with 20wt% silica along 5 parallel lines separated 20 nm from each other. The lines have been shifted in the vertical axis two stiffness units from the precedent one for the sake of clarity.

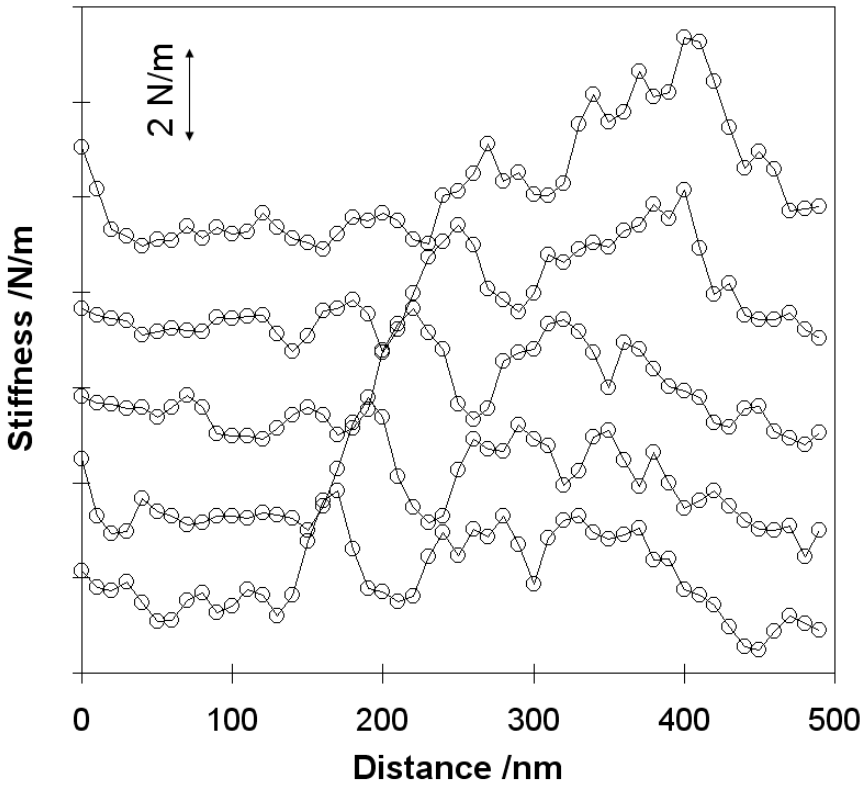

Figure A2.5. Stiffness measured by AFM indentation experiments in the sample with 25wt% silica along 5 parallel lines separated 20 nm from each other. The lines have been shifted in the vertical axis two stiffness units from the precedent one for the sake of clarity.

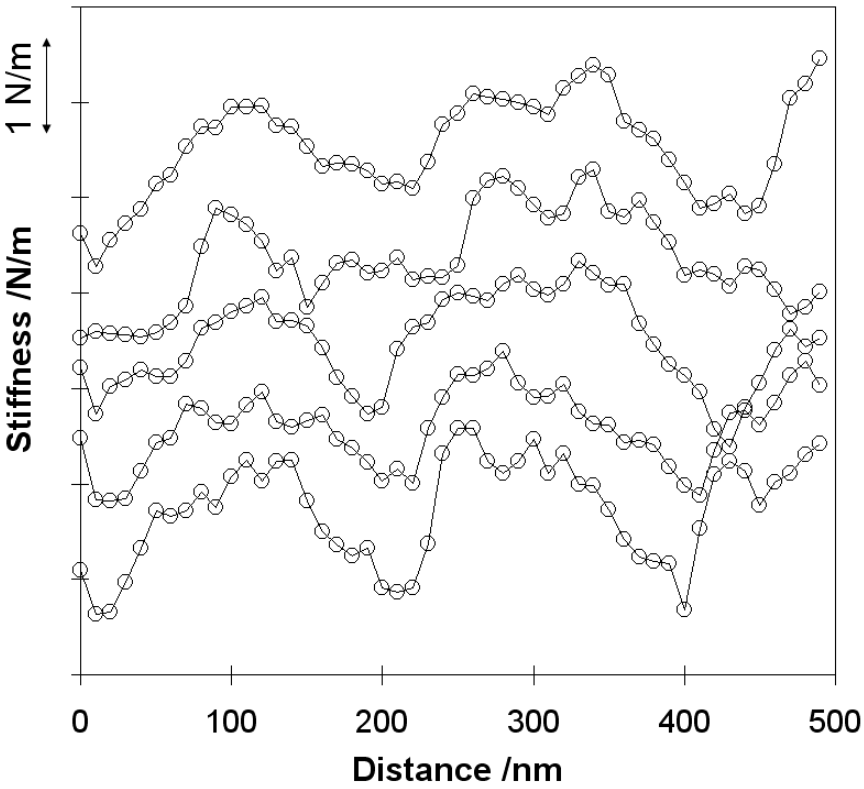

Figure A2.6. Stiffness measured by AFM indentation experiments in the sample with 30wt% silica along 5 parallel lines separated 20 nm from each other. The lines have been shifted in the vertical axis two stiffness units from the precedent one for the sake of clarity.

Appendix 3: c_p-c_{pref} for PHEA-based nanocomposites at different annealing temperatures

(c_p-c_{pref}) curves are referred to the sample mass. However, since silica does not exhibit any transition at this experimental range of temperatures, values can be easily corrected in order to take into account only the organic phase just dividing DSC thermograms by the theoretical polymer fraction on the sample.

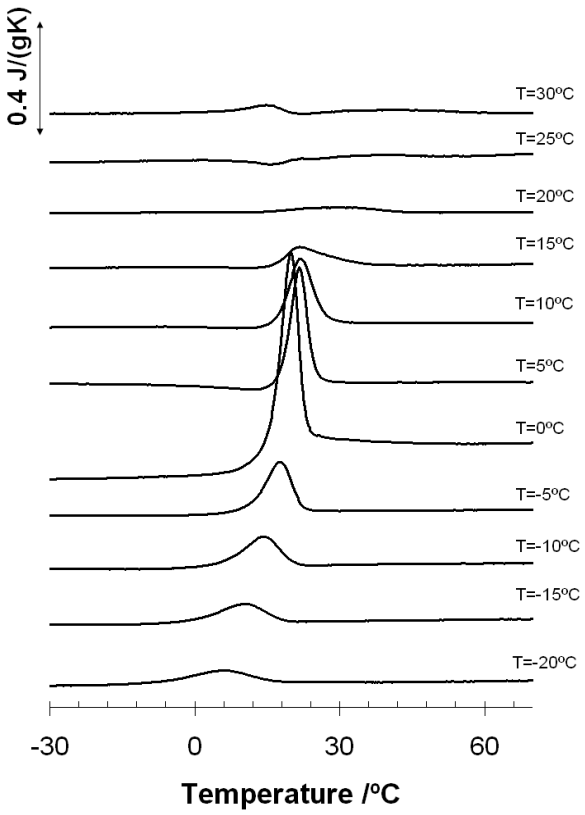

Figure A3.1. Temperature dependence of c_p-c_{pref} for PHEA after annealing at different temperatures (indicated at the right hand side of the figure) during 200 min. The profiles were shifted in the ordinate axis for the sake of clarity.

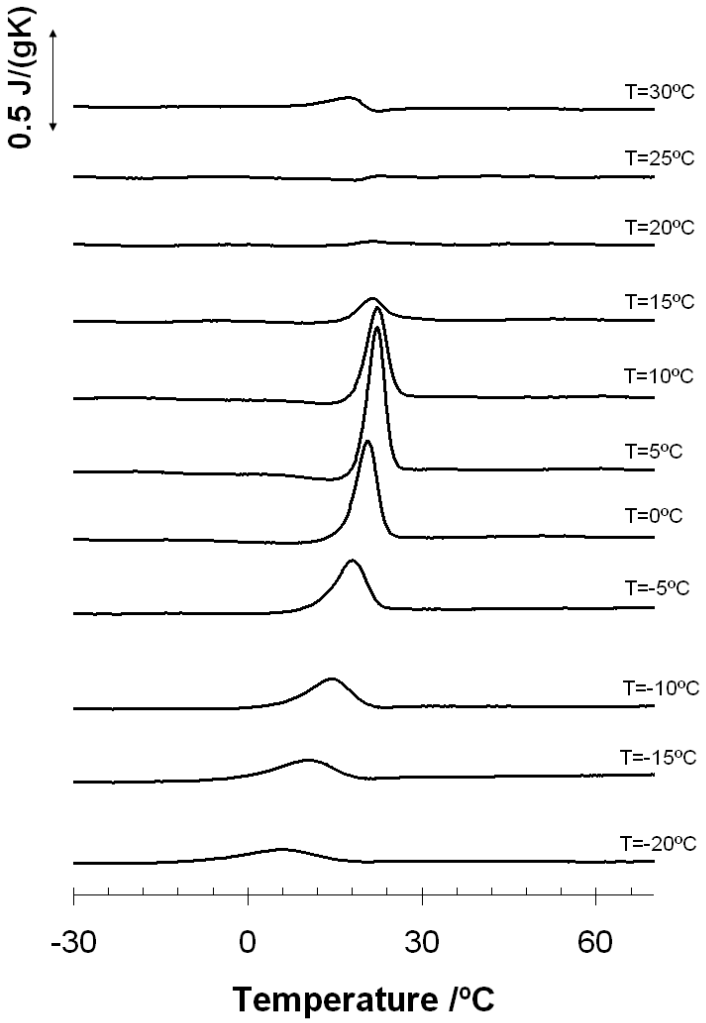

Figure A3.2. Temperature dependence of c_p-c_{pref} for PHEA+5wt% SiO_2 after annealing at different temperatures (indicated at the right hand side of the figure) during 200 min. The profiles were shifted in the ordinate axis for the sake of clarity.

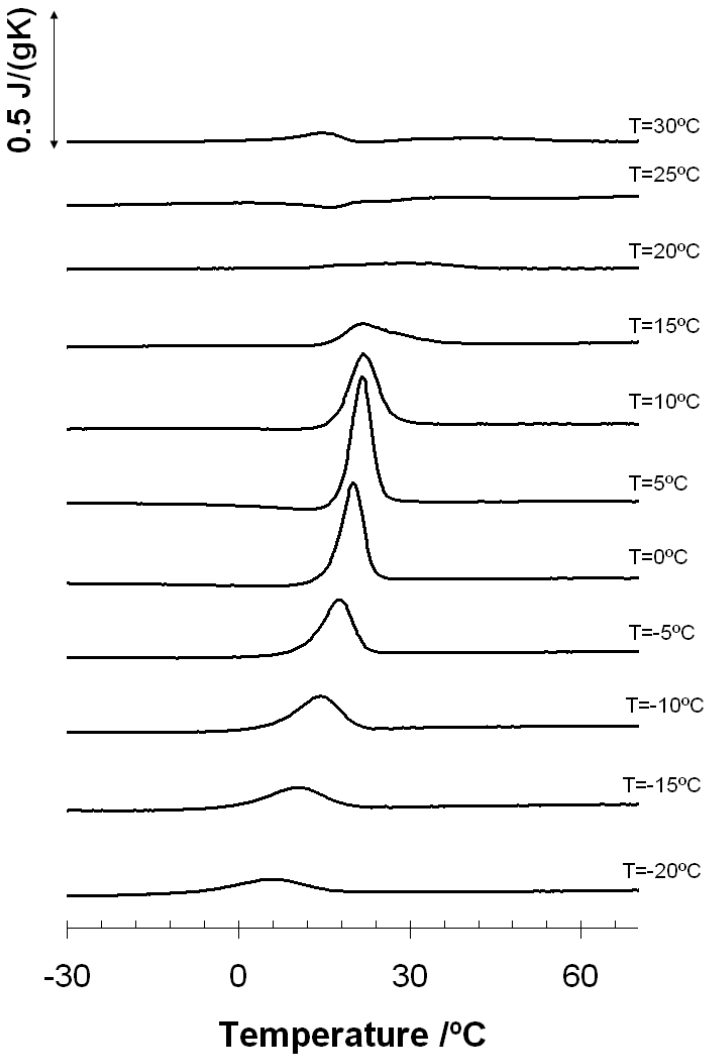

Figure A3.3. Temperature dependence of c_p-c_{pref} for PHEA+10wt% SiO_2 after annealing at different temperatures (indicated at the right hand side of the figure) during 200 min. The profiles were shifted in the ordinate axis for the sake of clarity.

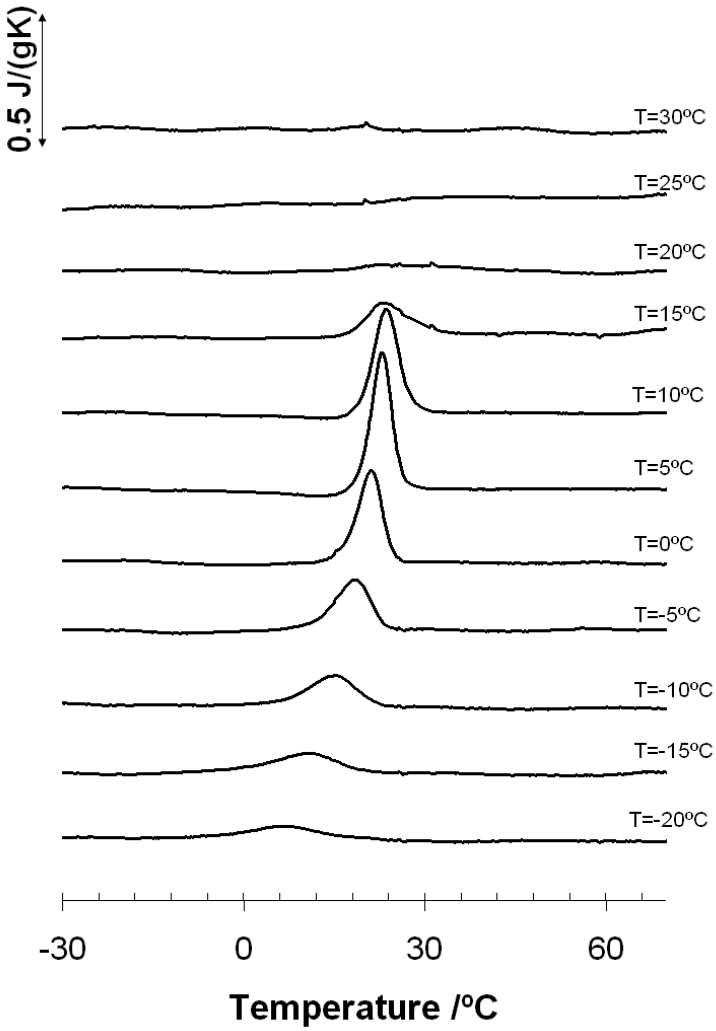

Figure A3.4. Temperature dependence of c_p-c_{pref} for PHEA+15wt% SiO_2 after annealing at different temperatures (indicated at the right hand side of the figure) during 200 min. The profiles were shifted in the ordinate axis for the sake of clarity.

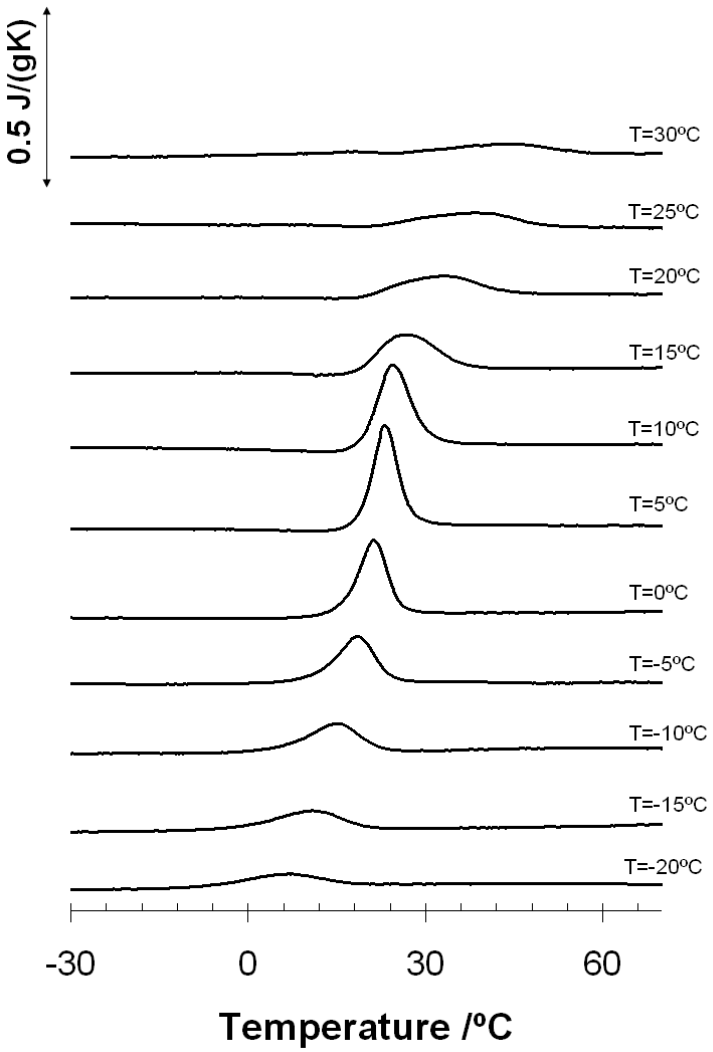

Figure A3.5. Temperature dependence of c_p-c_{pref} for PHEA+20wt% SiO_2 after annealing at different temperatures (indicated at the right hand side of the figure) during 200 min. The profiles were shifted in the ordinate axis for the sake of clarity.

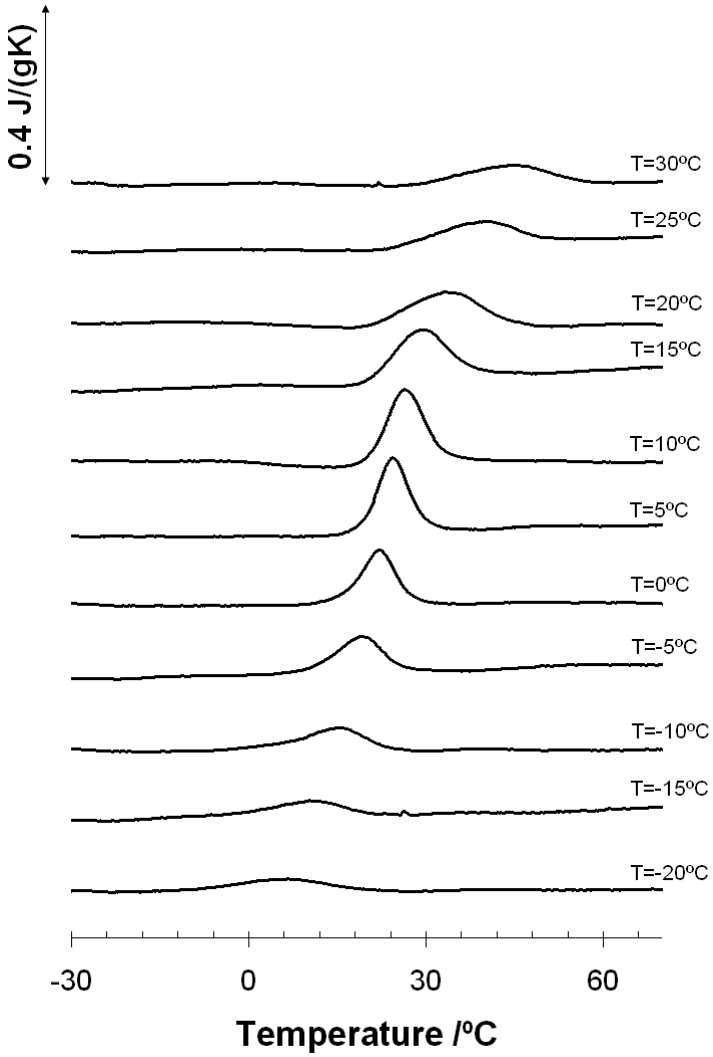

Figure A3.6. Temperature dependence of c_p-c_{pref} for PHEA+25wt% SiO_2 after annealing at different temperatures (indicated at the right hand side of the figure) during 200 min. The profiles were shifted in the ordinate axis for the sake of clarity.

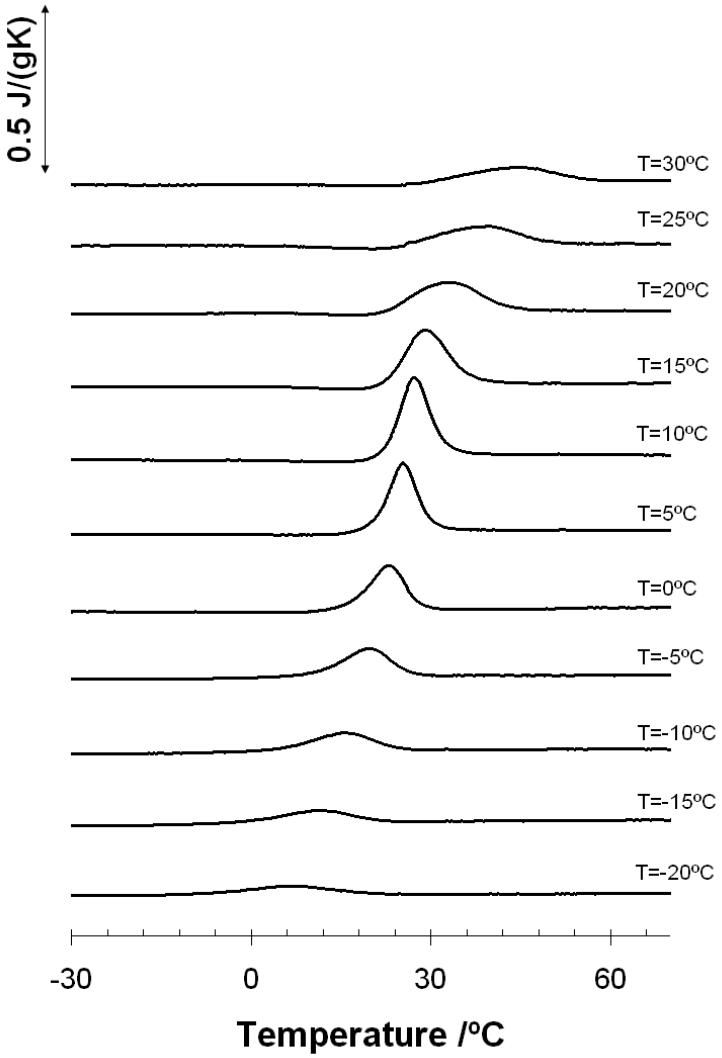

Figure A3.7. Temperature dependence of c_p-c_{pref} for PHEA+30wt% SiO_2 after annealing at different temperatures (indicated at the right hand side of the figure) during 200 min. The profiles were shifted in the ordinate axis for the sake of clarity.

Glossary

A_0	Free oscillation amplitude of the AFM cantilever
A_c	Projected elastic contact area between sample and tip
A_{sp}	Set point amplitude of the AFM cantilever
c_p	Specific heat capacity
c_{pref}	Specific heat capacity of the reference scan
$c_p\big\vert_g$	Specific heat capacity of the glass state
$c_p\big\vert_l$	Specific heat capacity of the liquid state
d	Deflection of the AFM tip
$D_v(r)$	Pore size distribution per volume
$D_s(r)$	Pore size distribution per surface
$D_l(r)$	Pore size distribution per length
E	Elastic modulus of the indented material
E_i	Elastic modulus of the indenter's material
E_r	Reduced elastic modulus
E'	Dynamic-mechanical storage modulus
F	Force applied by the AFM tip in nanoindentation assays
F_{max}	Maximum load applied in nanoindentation
h	Penetration of the AFM tip on the material
h_r	Residual depth remaining after unloading in indentation
h_{max}	Penetration at the maximum load
h_c	Contact penetration
k	Proportional constant relating the applied force with penetration
l/d	Aspect ratio of fillers
l/d_{cr}	Critical aspect ratio
m	Power law exponent related to the indenter's geometry
m_1	Mass of tetraethoxysilane
m_2	Mass of 2-hydroxyethyl acrylate
m_{SiO2}	Silica mass
m_{sol}	Solvent mass
m_{dry}	Material mass after drying
m_{sw}	Material mass when swollen

SiO_2	Molecular weight of silica
M_{TEOS}	Molecular weight of tetraethoxysilane
n_{dry}	Refractive index of dried samples
n_{sw}	Refractive index of samples equilibrated in water
p	Pressure needed to introduce Hg into pores
P	Dried sample weight
P′	Sample weight when immersed in n-octane
r	Pore radius
$\Re$	Gas constant
r_{sp}	Ratio between A_0 and A_{sp}
S	Stiffness
tan δ	Loss tangent
t_a	Annealing time
t_p	Time required for the maximum of the exothermic hydrolysis peak to arise
T_0	Temperature above T_g
T_1	Temperature below T_g
T_{10}	Temperature corresponding to 10 wt% loss
T_{50}	Temperature corresponding to 50 wt% loss
T_a	Annealing temperature
T_g	Enthalpic glass transition temperature
T_{hf}	Temperature corresponding to the maximum of the endothermic peak for the main degradation mechanism
T_{onset}	Onset temperature of melting peak
T_m	Temperature of maximum rate of weight loss
T_β	Temperature of the secondary mechanical relaxation
$v_{polymer}$	Specific volume of the polymer
v_T	Specific total volume
V_{Hg}	Mercury volume intruded at the maximum applied pressure
V_{pores}	Pores volume
V_T	Total volume
z	Z coordinate of the AFM scanner
α	Main mechanical relaxation
β	Secondary mechanical relaxation
β_{sw}	Complex secondary mechanical relaxation
Δh	Activation energy of the hydrolysis reaction
$\Delta c_p\big\vert_{Tg}$	Specific heat capacity increment at T_g
$\Delta H_{coh,g}$	Cohesive energy density at T_g
ΔT_g	Width of the glass transition

ε	Function which correlates the contact and maximum penetrations
γ	Surface tension of Hg
ϑ	Contact angle between Hg and the material surface
λ	Correcting factor for stiffness
ν	Poisson ratio of the indented material
ν_i	Poisson ratio of the indenter's material
π	Porosity
ρ_{mat}	Material density
ρ_{oct}	N-octane density
σ	Silica percentage
τ_{pore}	Pore tortuosity
AFM	Atomic Force Microscopy
ATR	Attenuated Total Reflectance
BPO	Benzoyl peroxide
CRR	Cooperative rearrangement region
EA	Ethyl acrylate
EDS	Energy dispersive x-ray spectrometer
ESC	Equilibrium solvent content
DMA	Dynamic mechanical analysis
DSC	Differential scanning calorimetry
FTIR	Fourier transform infrared spectroscopy
HCl	Hydrochloric acid
HEA	2-hydroxyethyl acrylate
MAF	Mobile amorphous fraction
NMR	Nuclear magnetic resonance
PHEA	Poly(2-hydroxyethyl acrylate)
PHEMA	Poly(2-hydroxyethyl methacrylate)
PMMA	Poly(methyl methacrylate)
RAF	Rigid amorphous fraction
RAF_{pol}	Rigid amorphous fraction regarding the organic phase
SAXS	Small angle x-ray scattering
SEM	Scanning electron microscopy
TEM	Transmission electron microscopy
TEOS	Tetraethoxysilane (also called tetraethyl orthosilicate)
TGA	Thermogravimetric analysis
TMOS	Tetramethoxysilane (also called tetramethyl orthosilicate)

References

[1] Tunc S, Maitz MF, Steiner G, Vázquez L, Pham MT, Salzer R. Colloid Surf B-Biointerfaces 42 (2005) 219

[2] Thierry B, Winnik FM, Merhi Y, Silver J, Tabrizian M. Biomacromolecules 4 (2003) 1564

[3] Monleón Pradas M, Gómez Ribelles JL, Serrano Aroca A, Gallego Ferrer G, Suay Antón J, Pissis P. Colloid Polym Sci 279 (2001) 323

[4] Salmerón Sánchez M, Monleón Pradas M, Gómez Ribelles JL. J Polym Sci Part B: Polym Phys 41 (2003) 1713

[5] Kyritsis A, Pissis P, Gómez Ribelles JL, Monleón Pradas M. J Non-Cryst Solids 172-174 (1994) 1041

[6] Salmerón Sánchez M, Gallego Ferrer G, Monleón Pradas M, Gómez Ribelles JL. Macromolecules 36 (2003) 860

[7] Castilla Cortázar I, Vidaurre A, Gallego Ferrer G, Monleón Pradas M, Gómez Ribelles JL, Meseguer Dueñas JM. J Non Cryst Solids 287 (2001) 130

[8] Monleón Pradas M, Gómez Ribelles JL, Serrano Aroca A, Gallego Ferrer G, Suay Antón J, Pissis P. Polymer 42 (2001) 4667

[9] Serrano Aroca A, Campillo Fernández AJ, Gómez Ribelles JL, Monleón Pradas M, Gallego Ferrer G, Pissis P. Polymer 45 (2004) 8949

[10] Serrano Aroca A, Gómez Ribelles JL, Monleón Pradas M, Vidaurre Garayo A, Suay Antón J. Eur Polym J 43 (2007) 4552

[11] Kolarik J, Vacik J, Kopecek J, Int J Polym Mater 3 (1975) 259

[12] Salmerón Sánchez M, Monleón Pradas M, Gómez Ribelles JL. Eur Polym J 40 (2004) 329-334

[13] Vasilopoulou M, Boyatzis S, Raptis I, Dimotikalli D, Argitis P. J Mater Chem 14 (2004) 3312

[14] Tielens F, Gervais C, Lambert JF, Mauri F, Costa D. Chem Mater 20 (2008) 3336

[15] Zerda TW, Artaki I, Jonas J. J Non-Cryst Solids 81 (1986) 365

[16] Brinker CJ, Keefer KD, Schaefer DW, Ashley CS. J Non-Cryst Solids 48 (1982) 47

[17] Brinker CJ, Keefer KD, Schaefer DW, Assink RA, Kay BD, Ashley CS. J Non-Cryst Solids 63 (1984) 45

[18] Brinker CJ, Scherer GW. J Non-Cryst Solids 70 (1985) 301

[19] Yoldas BE. J Non-Cryst Solids 51 (1982) 105

[20] Strawbridge I, Craievich AF, James PF. J Non-Cryst Solids 72 (1985) 139

[21] Patel S, Bandyopadhyay A, Vijayabaskar V, Bhowmick AK. Polymer 46 (2005) 8079

[22] Unger B, Jancke H, Hähnert M, Stade H. J Sol-Gel Sci Technol 2 (1994) 51

[22] Day VW, Eberspacher TA, Chen Y, Hao J, Klemperer WG. Inorg Chim Acta 229 (1995) 391

[23] Sanchez C, Ribot F. New J Chem 18 (1994) 1007

[24] Pomogailo AD. Colloid J 67 (2005) 658

[25] Mammeri F, Bourhis EL, Rozes L, Sanchez C. J Mater Chem 15 (2005) 3787

[26] Livage J, Henry M, Sanchez C. Prog Solid State Chem 18 (1988) 259

[27] Donatti DA, Vollet DR. J Sol-Gel Sci Techn 17 (2000) 19

[28] Sakka S, Yoko T. J Non-Cryst Solids 147/148 (1992) 394

[29] Hajji P, David L, Gerard JF, Pascault P, Vigier G. J Polym Sci Part B: Polym Phys 37 (1999) 3172

[30] Wei Y, Jin D, Yang C, Wei G. J Sol-Gel Sci Technol 7 (1996) 191

[31] Matejka L, Dusek K, Plestil J, Kríz J, Lednický F. Polymer 40 (1998) 171

[32] Donatti DA, Vollet DR. J Sol-Gel Sci Technol 4 (1995) 99

[33] Vollet DR, Donatti DA, Campanha JR. J Sol-Gel Sci Techn 6 (1996) 57

[34] Donatti DA, Vollet DR. J Non-Cryst Solids 208 (1996) 99

[35] Ramirez-Del-Solar M, De La Rosa-Fox N, Esquivias L, Zarzicky J. J Non-Cryst Solids 121 (1990) 40

[36] Okkerse C. Physical and chemical aspects of adsorbents and catalyst. Academic Press, New York (1970)

[37] Stöber W, Fink A, Bohn E. J Colloid Interface Sci 26 (1968) 62

[38] McCarthy DW, Mark JE, Schaefer DW. J Polym Sci, Part B: Polym Phys 36 (1998) 1167

[39] Giannelis EP, Krishnamoorti R, Manias E. Adv Polym Sci 138 (1999) 107

[40] Termonia Y. Polymer 48 (2007) 6948

[41] Bastiaansen CWM, Leblans PJR, Smith P. Macromolecules 23 (1990) 2365

[42] Godara A, Raabe D. Compos Sci Technol 67 (2007) 2417

[43] Jia X, Li Y, Cheng Q, Zhang S, Zhang B. Eur Polym J 43 (2007) 1123

[44] Huang SL, Chin WK, Yang WP. Polymer 46 (2005) 1865

[45] Zhang F-A, Yu C-L. Eur Polym J 43 (2007) 1105

[46] Motomatsu M, Takahashi T, Nie HY, Mizutani W, Tokumoto H. Polymer 38 (1997) 177

[47] Pukánszky B. Eur Polym J 41 (2005) 645

[48] Bansal A, Yang H, Li C, Benicewicz BC, Kumar SK, Schadler LS. J Polym Sci Part B: Polym Phys 44 (2006) 2944

[49] Pukánszky B, Fekete E. Adv Polym Sci 139 (1999) 109

[50] Kalogeras IM, Neagu ER. Eur Phys J E 14 (2004) 193

[51] Bansal A, Yang H, Li C, Benicewicz BC, Kumar SK, Schadler LS. Nat Mater 4 (2005) 693

[52] Rittigstein P, Torkelson JM. J Polym Sci Part B: Polym Phys 44 (2006) 2935

[53] Khaled SM, Sui R, Charpentier PA, Rizkalla AS. Langmuir 23 (2007) 3988

[54] Tertykh V, Bolbukh Y, Yanishpolskii V. Macromol Symp 221 (2005) 145

[55] Costa ROR, Lameiras FS. J Sol-Gel Sci Techn 27 (2003) 343

[56] Joseph R, Zhang S, Ford WT. Macromolecules 29 (1996) 1305

[57] Guo L, Lee JH, Beaucage G. J Non-Cryst Solids 243 (1999) 61

[58] Breiner JM, Mark JE, Beaucage G. J Polym Sci, Part B: Polym Phys 37 (1999) 1421

[59] Jackson CL, Bauer BJ, Nakatani AI, Barnes JD. Chem Mater 8 (1996) 727

[60] Arora K, Lesser A, McCarthy T. Polymer Eng Sci 38 (1998) 2055

[61] Thomson RC, Wake MC, Yaszemski MJ, Mikos AG. Adv Polym Sci 122 (1995) 245

[62] Andrianova G, Parkhomov S. Polymer Eng Sci 37 (1997) 1367

[63] Landers R, Pfister A, Hübner U, John H, Schmelzeisen R, Mülhaupt R. J Mater Sci 37 (2002) 3107

[64] Moroni L, de Wijn JR, van Blitterswijk CA. Biomaterials 27 (2006) 974

[65] Brígido Diego R, Pérez Olmedilla M, Serrano Aroca A, Gómez Ribelles JL, Monleón Pradas M, Gallego Ferrer G, Salmerón Sánchez M. J Mater Sci: Mater Med 40 (2005) 4881

[66] Kim TK, Yoon JJ, Lee DS, Park TG. Biomaterials 27 (2006) 152

[67] Rücker M, Laschke MW, Junker D, Carvalho C, Schramm A, Mülhaupt R, Gellrich NC, Menger MD. Biomaterials 27 (2006) 5027

[68] Richardson SM, Curran JM, Chen R, Vaughan-Thomas A, Hunt JA, Freemont AJ, Hoyland JA. Biomaterials 27 (2006) 4069

[69] Chirila TV. Biomaterials 22 (2001) 3311

[70] Laurencin CT, Freeman JW. Biomaterials 26 (2005) 7530

[71] Dušek K. Polymer networks: structure and mechanical properties. Plenum Press, New York (1971)

[72] Kokubo T. Mater Sci Eng, C 25 (2005) 97

[73] Gómez Tejedor JA, Rodríguez Hernández JC, Gómez Ribelles JL, Monleón Pradas M, J Macromol Sci Part B: Phys 46 (2007) 43

[74] Larraz E, Elvira C, San Román J. Biomacromolecules 6 (2005) 2058

[75] Bao Q, Higham P. U.S. Patent No. 5,047,055 (1991)

[76] Withers JR, Aston DE. Adv Coll Int Sci 120 (2006) 57

[77] Oliver WC, Pharr GM. J Mater Res 7 (1992) 1564

[78] Geng K, Yang F, Druffel T, Grulke EA. Polymer 46 (2005) 11768

[79] Yang S, Zhang Y-W, Zeng K. J Appl Phys 95 (2004) 3655

[80] Drelich J, Xu Z, Masliyah J. Langmuir 22 (2006) 8850

[81] Pethica JB, Oliver WC. Phys Scr T19 (1987) 61

[82] Sargsyan A, Tonoyan A, Davtyan S, Schick C. Eur Polym J 43 (2007) 3113

[83] Wunderlich B. Progr Polym Sci 28 (2003) 383

[84] Hodge IM. J Non Cryst Solids 169 (1994) 211

[85] Moynihan CT, Macedo PB, Montrose CJ, Gupta PK, DeBolt MA, Dill JF, Dom BE, Drake PW, Easteal AJ, Elterman PB, Moeller RP, Sasabe H. Ann N Y Acad Sci 279 (1976) 15

[86] Narayanaswamy OS. J Am Ceram Soc 54 (1971) 491

[87] Kovacs AJ, Aklonis JJ, Hutchinson JM, Ramos AR. J Polym Sci, Polym Phys Ed 17 (1979) 1097

[88] Scherer GW. J Am Ceram Soc 67 (1984) 504

[89] Gómez Ribelles JL, Monleón Pradas M. Macromolecules 28 (1995) 5867

[90] Gómez Ribelles JL, Monleón Pradas M, Vidaurre Garayo A, Romero Colomer F, Más Estelles J, Meseguer Dueñas JM. Macromolecules 28 (1995) 5878

[91] Petrie SEB. J Polym Sci Pol Chem 10 (1972) 1255

[92] Gómez Ribelles JL, Ribes Graus A, Díaz Calleja R. Polymer 31 (1991) 223

[93] Cowie JMG, Ferguson R. Polymer 34 (1993) 2135

[94] Monleón Pradas M, Gómez Ribelles JL, Santos Esteve L. Spanish Patent Application P200502805, "Nuevos andamiajes poliméricos porosos tridimensionales para aplicaciones médicas" (2005)

[95] Knoll A, Magréele R, Krausch G. Macromolecules 34 (2001) 4159

[96] Godehart R, Lebek W, Adhikari R, Rosenthal M, Martin C, Frangov S, Michler G. Eur Pol J 40 (2004) 917

[97] Markiewicz P, Goh MC. Langmuir 10 (1994) 5

[98] Carniglia SC. J Catal 102 (1986) 401

[99] Pang J-B, Qiu K-Y, Xu J, Wei Y, Chen J. J. Inorg Organomet Polym Mater 10 (2000) 39

[100] Qi D, Bao Y, Weng Z, Huang Z. Polymer 47 (2006) 4622

[101] Sugimoto H, Daimatsu K, Nakanishi E, Ogasawara Y, Yasumura T, Inomata K. Polymer 47 (2006) 3754

[102] Rubio F, Rubio J, Oteo JL. J Sol-Gel Sci Techn 8 (1997) 159

[103] Wei Y, Jin D, Ding T, Shih W-H, Liu X, Cheng SZD, Fu Q. Adv Mater 3 (1998) 313

[104] Wei Y, Xu J, Dong H, Dong JH, Qiu K, Jansen-Varnum AS. Chem Mater 11 (1999) 2023

[105] Guo W, Xu Li, Zhao XS. Micropor Mesopor Mat 93 (2006) 285

[106] Kruk M, Celer EB, Jaroniec M. Chem Mater 16 (2004) 698

[107] Zhang F, Yan Y, Yang H, Meng Y, Yu C, Tu B, Zhao D. J Phys Chem B 109 (2005) 8723

[108] Lin H-P, Chang-Chien C-Y, Tang C-Y, Lin C-Y. Micropor Mesopor Mat 93 (2006) 344

[109] Tamayo J, García R. Appl Phys Lett 71 (1997) 2394

[110] Cleveland JP, Anczykowski B, Schmid AE, Elings VB. Appl Phys Lett 72 (1998) 2613

[111] Tamayo J, García R. Appl Phys Lett 73 (1998) 2926

[112] García R, Tamayo J, Calleja M, García F. Appl Phys A 66 (1998) S309

[113] Martínez NF, García R. Nanotechnology 17 (2006) S167

[104] García R, Gómez CJ, Martínez NF, Patil S, Dietz C, Magerle R. Phys Rev Lett 97 (2006) 016103

[105] Nagao E, Dvorak JA. Biophys J 76 (1999) 3289

[106] Sawyer LC, Grubb DT. Polymer microscopy. Chapman & Hall (1996) p39

[107] Rodríguez Hernández JC, Monleón Pradas M, Gómez Ribelles JL. J Non-Cryst Solids 354 (2008) 1900

[108] Haskouri JE, Zárate DO, Guillem C, Beltrán-Porter A, Caldés M, Marcos MD, Beltrán-Porter D, Latorre J, Amorós P. Chem Mater 14 (2002) 4502

[109] Huerta L, Guillem C, Latorre J, Beltrán A, Martínez-Máñez R, Marcos MD, Beltrán D, Amorós P. Solid State Sci 8 (2006) 940

[110] Bosch P, Del Monte F, Mateo JL, Levy D, J Pol Sci Part A: Polym Chem 34 (1996) 3289

[111] Landry CJT, Coltrain BK, Wesson JA, Zumbulyadis N, Lippert JL. Polymer 33 (1992) 1496

[112] Gallego Ferrer G, Monleón Pradas M, Gómez Ribelles JL, Macromol Symp 200 (2003) 217

[113] Gallego Ferrer G, Monleón Pradas M, Gómez Ribelles JL, Salmerón Sánchez M. Polymer 45 (2004) 6207

[114] Monleón Pradas M, Gómez Ribelles JL, Serrano Aroca A, Gallego Ferrer G, Suay Antón J, Pissis P. Colloid Polym Sci 279 (2001) 323

[115] Priestley RD, Rittigstein P, Broadbelt LJ, Fukao K, Torkelson JM. J Phys Condens Matter 19 (2007) 205120

[116] Kalogeras IM. Acta Mater 53 (2005) 1621

[117] De Farias RF, Airoldi C. J Therm Anal 53 (1998) 751

[118] Bertini F, Audisio G, Zuev VV. Polym Degrad Stabil 89 (2005) 233

[119] Liufu S-C, Xiao H-N, Li Y-P. Polym Degrad Stabil 87 (2005) 103

[120] Jang J, Park J. J Appl Pol Sci 83 (2002) 1817

[121] Lu H, Wang B, Ma J, Huang G, Viswanathan H, Mech Time-Depend Mater 7 (2003) 189

[122] Hues SM, Draper CF. Procedures in Scanning Probes Microscopies. Colton, Engel, Frommer, Gaub, Gewirth, Guckenberger, Heckl, Parkinson eds. John Wiley & Sons (1999) p585

[123] Fischer-Cripps AC. Surf Coat Tech 200 (2006) 4153

[124] Rodríguez Hernández JC, Salmerón Sánchez M, Gómez Ribelles JL, Monleón Pradas M. Eur Polym J 43 (2007) 2775

[125] Keddie JL, Jones RAL, Cory RA. Europhys Lett 27 (1994) 59

[126] Sharp JS, Forrest JA. Phys Rev E 67 (2003) 031805

[127] Pallikari-Viras F, Li X, King TA. J Sol-Gel Sci & Technol 7 (1996) 203

[128] Lu H, Nutt S. Macromolecules 36 (2003) 4010

[129] Gómez Ribelles JL, Meseguer Dueñas JMª, Monleón Pradas M. Polymer 29 (1988) 1124

[130] Starr FW, Schoroder TB, Glotzer SC. Phys Rev E 64 (2001) 021802

[131] Fryer DS, Peters RD, Kim EJ, Tomaszewski JE, de Pablo JJ, Nealey PF, White CC, Wu W-L. Macromolecules 34 (2001) 5627

[132] Lipatov YS, Privalko VP. Polym Sci USSR 14 (1972) 1843

[133] Privalko VP, Lipatov YS, Kercha YY. Polym Sci USSR 12 (1970) 1520

[134] Bershtein VA, Egorova LM, Yakushev PN, Pissis P, Sysel P, Brozova L. J Polym Sci B: Polym Phys 40 (2002) 1056

[135] В. П. Привалко. Молекулярное Строение и Свойства Полимеров. Химия, Ленинград, 1986 (Privalko VP. Molecular Structure and Properties of Polymers (in russian). Khimiya, Leningrad) (1986) p85

[136] Lu H, Nutt S. Macromol Chem Phys 204 (2003) 1832

[137] Théneau C, Salmerón Sánchez M, Rodríguez Hernández JC, Monleón Pradas M, Saiter JM, Gómez Ribelles JL. Eur Phys J E 24 (2007) 69

[138] Hernández Sánchez F, Meseguer Dueñas JM, Gómez Ribelles JL. J Therm Anal Calorim 72 (2003) 631

[139] Gómez Ribelles JL, Meseguer Dueñas JM, Torregrosa Cabanilles C, Monleón Pradas M. J Phys: Condens Matter 14 (2003) 1149

[140] Salmerón Sánchez M, Brígido Diego R, Iannazzo SAM, Gómez Ribelles JL, Monleón Pradas M. Polymer 45 (2004) 2349

[141] Rodríguez Hernández JC, Serrano Aroca A, Gómez Ribelles JL, Monleón Pradas M. J Biomed Mater Res Part B: Appl Biomater 84B (2008) 541

[142] Brígido Diego R, Gómez Ribelles JL, Salmerón Sánchez M. J App Polym Sci 104 (2007) 1475

[143] Más Estellés J, Krakovsky I, Rodríguez Hernández JC, Piotrowska AM, Monleón Pradas M. J Mat Sci 42 (2007) 8629

[144] Brígido Diego R, Más Estellés J, Sanz JA, García-Aznar JM, Salmerón Sánchez M. J Biomed Mater Res Part B: Appl Biomater 81 (2007) 448

[145] Gibson LJ, Ashby M. The mechanics of foam: Basic results. In: Clarke DR, Suresh S, Ward IM, editors. Cellular Solids: Structure and Properties. Cambridge University Press (2001) p175

[146] Zhang K, Wang Y, Hillmyer MA, Francis LF. Biomaterials 25 (2004) 2489

[147] Rimer JD, Trofymluk O, Navrotsky A, Lobo RF, Vlachos DG. Chem Mater 19 (2007) 4189